

Heidelberg University
Department of Physics and Astronomy

Feedback-Driven Wind Simulations on a Moving Mesh

Master Thesis in Physics by
Raphael ThienNam King
born in Fountain Valley, California

January 2026

Abstract

Stellar feedback-driven galactic winds are multiphase structures that can affect the evolution of galaxies by regulating star formation and enriching the interstellar medium (ISM) and intergalactic medium (IGM) with metals. Despite their importance, much about their structure and evolution remains unsettled, particularly in regards to the driving mechanisms of multiphase gas. There is a clear need for high detail galactic-scale wind simulations that can simultaneously analyze their flow at large scales while also being able to resolve their core processes at small scales. To that end, we build a suite of idealized hydrodynamic simulations made with the moving-mesh code AREPO. We study the structure and evolution of winds driven by a central starburst-like energy injection, varying the energy and mass loading, scale, and time variability, as well as assessing the impact of background gravity from an NFW halo. We examine how the physical setup can impact the wind structure, studying both spherically symmetric winds and winds where we include an idealized central disk galaxy embedded within a uniform circumgalactic medium (CGM). Importantly, we include a simple model for radiative cooling and investigate its impact on outflow evolution. We find that winds propagate outward as wind-blown superbubbles which form biconical morphologies when in the presence of a galactic disk. Additionally, efficient radiative cooling allows for cool clouds to be ejected directly from the galactic disk and survive at substantial distances into the CGM, while a cooling phase forms in-situ from the wind. The natural spatial adaptivity of the moving Voronoi mesh provides a resolution advantage over fixed grid techniques, allowing us to study the structure and evolution of winds and cool gas with exceptional detail.

Contents

Abstract	iii
Contents	v
List of Figures	vii
List of Tables	ix
1 Introduction	1
2 Theoretical Foundations	4
2.1 Thermally Driven Outflows	4
2.2 The Problem of Entrainment	6
2.3 Radiative Cooling	7
2.4 Radiative Cooling and Multiphase Gas	9
3 Simulation Setup	11
3.1 Initial Conditions	11
3.1.1 Galactic Disk	11
3.1.2 Circumgalactic Medium	12
3.1.3 Creating the Initial Conditions	13
3.2 Feedback-Driven Injection of Mass and Energy	15
3.3 Radiative Cooling Model	16
3.4 Refinement and Derefinement	17
4 Results and Discussion	19
4.1 Structure and Evolution of Spherically Symmetric Winds	21
4.1.1 Evolution of CC85 Winds	21
4.1.2 Energy Injection Beyond CC85	26
4.2 Winds on a Galactic Disk	28
4.3 Effects of Radiative Cooling on Galactic Winds	32
4.3.1 The Formation of Cold Gas	33
4.3.2 Effects of Energy and Mass Load on Radiatively Cooled Winds	39
4.3.3 Survival and Entrainment of Cold Clouds	48
4.3.4 Cooling Models	52
4.3.5 The Evolution of Shocks and Episodic Bursts	53

5 Conclusions and Outlook	61
5.1 Summary of Key Results	61
5.2 Outlook	62
Bibliography	63

List of Figures

2.1	Cooling functions at redshift $z = 0$, plotted as a function of temperature	7
3.1	Initial conditions pre-relaxation process	13
3.2	Post-static relaxation initial conditions	14
3.3	Initial conditions following the resolution of the two-step relaxation process	14
3.4	Voronoi diagrams of the initial condition at $t = 1$ Gyr and $t = 1.5$ Gyr	16
3.5	Radial profiles of the initial conditions	17
4.1	Density, velocity, and temperature panels of a cc85 outflow	22
4.2	Time evolution of a spherically symmetric outflow	23
4.3	Radial profiles comparing the variations in mass and energy load	24
4.4	Radial profiles comparing the variations in injection radii.	26
4.5	Radial profiles of velocity for varying halo concentration	27
4.6	Radial profiles assessing the impact of an intermittent burst	28
4.7	Edge-on central slices and profiles of density, radial velocity, and temperature at steady state	29
4.8	Bicone region of analysis	30
4.9	Temporal evolution of density for varying disk models	31
4.10	Voronoi diagrams comparing the cell states of static vs moving mesh	33
4.11	Temperature and density slices of non-cooled wind vs a cooled wind	34
4.12	Initial formation of cold gas	35
4.13	Radial profiles of n , v , T , P for metallicities	37
4.14	Temperature profiles of this work vs CGOLS	39
4.15	temperature profiles and histograms for varying energy load and cooling	40
4.16	Cooling time/advection time vs radius	41
4.17	Cold gas mass fraction over load parameters	42
4.18	Density profiles and histograms for varying load configurations	43
4.19	Phase diagrams of temperature and density	44
4.20	Velocity profiles and edge-on slice plots	45
4.21	Mass and energy outflow rates for different loading parameters	47
4.22	Column densities of a cold cloud	49
4.23	temperature profiles and slice of the cloud	49
4.24	Velocity slice of the cold cloud	50
4.25	Pressure slice of cold cloud	51
4.26	Temperature comparison between cooling models.	52
4.27	Volumetric cooling rate comparison between cooling models.	53

4.28 Temperature temporal evolution for varying duty cycle	55
4.29 Velocity, density, and temperature profiles for each episodic starburst configuration	57
4.30 Cold gas mass fraction over duty cycle configurations	58
4.31 Temperature over time weighted by mass	59

List of Tables

3.1	Table of parameters that are used to define the initial conditions	15
4.1	Table of key parameters that we vary across our simulations	19
4.2	Table of parameters varied across each section	20
4.3	Mass and energy load cases for radiative cooled winds	39
4.4	Episodic burst cases for radiatively cooled winds	54

1 Introduction

Just as galaxies provide the raw feed needed to facilitate the formation of stars, so too can stars give back material needed to drive the evolution of galaxies in the form of mass, energy, and momentum. These processes, referred to as feedback, can express themselves in many different ways. The most spectacular expression of feedback, however, comes in the form of galactic winds¹, whereby the injection of mass and energy into a galaxy drives an outflow that is so fast that it escapes the gravitational pull of the host galaxy ([Schneider et al. 2020](#)). Galactic winds can have major ramifications for the long-term evolution of galactic environments. Firstly, winds inherently play an ejective role in galaxy evolution. By removing gas from galaxies, winds can enrich the interstellar medium (ISM) and circumgalactic medium (CGM) with metals, shaping the mass-metallicity relation and explaining the low metallicities found in low-mass galaxies ([Zhang 2018](#)). However, galactic winds are also preventative in nature. By injecting energy and momentum into their surroundings, winds delay or prevent the accretion of cold mass into the galaxy, starving it of the needed gas to facilitate star formation, and potentially quenching the formation of stars in galaxies ([Thompson & Heckman 2024](#); [Veilleux et al. 2020](#)). Together, the preventative and ejective nature of winds form a rich ecosystem that plays a critical role in regulating the flow of galactic mass across large timescales.

Structurally, galactic winds form bipolar morphologies that operate on kiloparsec scales, from the $\sim 5 - 10$ kpc of M82 and NGC 253 ([Veilleux et al. 2020](#)) to the 50 kpc of the Makani galaxy ([Rupke et al. 2019, 2023](#)), and can reach speeds on the order of $v \gtrsim 10^3$ km/s. Winds can form in two ways. The first is through stellar feedback, where mass, energy, and momentum from sources such as core collapse supernovae, stellar winds, or radiation is injected into the interstellar medium, driving mass and energy outward in the form of a wind. The second is through AGN feedback, where gas accretion onto an AGN is converted into an outflow. Some galaxies, such as Mrk 231, contain winds that originate from both stellar sources and AGN ([Zhang 2018](#); [Veilleux et al. 2020](#)). For this work, we focus on stellar feedback-driven winds, which play a more significant role in the evolution of the low-mass star-forming galaxies which make up most of the known galaxies in the universe. Due to their exceptionally high rates of star formation, the nuclei of starburst galaxies provide the most well-observed hosts for the feedback-driven galactic-scale winds across both the local and high redshift universe, making them the ideal case studies for galactic winds ([Strickland & Heckman 2009](#); [Thompson & Heckman 2024](#)).

Feedback-driven winds were first discovered during the 1960s, where along with the discovery of the now archetypal starburst galaxy M82, optical spectroscopy found that cool ionized gas can

¹Note that the terms "winds" and "outflows" are often used interchangeably in the literature. Here, we adopt the same convention as [Schneider et al. \(2020\)](#) and define "winds" to be gas that is moving fast enough to escape the halo potential and "outflows" to mean any gas that is moving away from the galaxy. However, given that we focus entirely on the former, the terms are functionally the same.

be accelerated outward at supersonic velocities ([Zhang 2018](#)). Stellar feedback, particularly in the form of supernovae explosions, was proposed as a wind-driver with the discovery of extended X-ray emissions of the now archetypal M82 ([Watson et al. 1984](#)) as well as NGC 253 ([Fabbiano & Trinchieri 1984](#)). The CC85 model of [Chevalier & Clegg \(1985\)](#) was developed soon after to model supernova feedback processes that could drive a then undiscovered hot phase outward in the form of a supersonic wind. The launch of high-resolution X-Ray observatories such as Chandra would allow for the detection of the diffuse hard X-ray emissions associated with hot plasmas ([Strickland & Heckman 2009](#)). Subsequent observations of galactic winds would use tracer measurements to detect gas parcels that vary in temperature, velocity, and density. These tracers include: CO for cold molecular gas ($T < 10^4$ K) e.g. [Fluetsch et al. \(2019\)](#), H α and [S $_{\text{II}}$] for cool gas ($T \sim 10^4 - 10^5$ K) e.g. [Xu et al. \(2023\)](#), and [S $_{\text{III}}$] for warm gas ($T \sim 10^5 - 10^6$ K) ([Schneider 2015](#)). Recently, optical integral fields have been used to resolve tracers across multiple wavelengths and temperatures ranges e.g. [Rupke et al. \(2019\)](#). Collectively, these observations reveal that galactic winds are fundamentally multiphase structures, containing colder, high density gas phases embedded within hotter, less dense phases.

Developing an explanatory foundation behind multiphase winds is an inherently complex endeavor. Their structure and formation is the product of several non-linear processes, and as such cannot be explained by analytic models. Because of this, hydrodynamic simulations have become essential tools to establishing a physical understanding behind the nature of galactic winds. The results have been quite promising. Adiabatic wind simulations have managed to accurately describe the hot phase observed in X-ray emissions using relatively few parameters e.g. [Strickland & Heckman \(2009\)](#). On cosmological scales, the TNG50 suite e.g. [Nelson et al. \(2019\)](#); [Pillepich et al. \(2019\)](#) have demonstrated that winds possess a natural collimation from which bipolarity can emerge, while the FIRE simulations e.g. [Hopkins et al. \(2014, 2018\)](#) have characterized the inefficiency of star formation resulting from stellar feedback.

Despite these breakthroughs, there is much that remains unsettled. Of particular importance in recent years has been determining the driving mechanisms of the cooler phases. This is because the creation and destruction processes of these phases operate on scales that are unresolvable by cosmological simulations ([Veilleux et al. 2020](#)). Given the high wind velocities relative to the cloud, the traditional view has been that the hot wind serves as the "Prime Mover" ([Thompson & Heckman 2024](#)) that sweeps up cool gas clouds from the ISM and accelerates them outward via ram pressure. This view, however, is complicated by results from simulation studies, which conclude that the timescales needed for the wind to transfer a sufficient amount of momentum to entrain the cloud is far longer than the timescales needed to shred it via hydrodynamic instabilities. Since then, many studies have focused on attempting to find a mechanism that can stabilize cool clouds, allowing them to become entrained. Thus far, the most promising and developed candidate for such a mechanism is radiative cooling. It has been established in cloud crushing studies such as [Scannapieco & Brüggen \(2015\)](#); [Gronke & Oh \(2018\)](#); [Fielding et al. \(2020\)](#) that radiative cooling can dampen instabilities, extending the lifetime of cold clouds. However, these studies often assume a laminar background wind, making it difficult to ascertain the efficacy of radiative cooling as a mechanism of cool clouds in a true galactic wind environment ([Schneider et al. 2020](#); [Dutta et al. 2025](#)). An alternative model for driving cool cloud production has been proposed by [Thompson et al. \(2016\)](#), who argue that cold clouds can form in-situ from an initially hot phase, wherein the initial destruction of cool clouds seeds thermal instabilities and perturbations. At large distances, these winds enter a region where radiative cooling dominates over adiabatic expansion, facilitating

cool cloud production at large distances. It is probable that for a sufficiently cooled wind, both mechanisms would be simultaneously active and linked to each other.

Given the uncertainties in determining the driving mechanisms of multiphase gas, there is a demonstrated need for more galactic-scale wind simulations that are large enough to avoid the domain uncertainties of cloud–wind simulations while simultaneously maintaining sufficient detail to resolve the formation and destruction processes of the cold phases. To that end, this thesis builds a suite of idealized stellar-feedback driven galactic wind simulations, with the overarching goal being to achieve a better understanding of the physical structure and evolution behind feedback-driven winds. Our work is motivated by the following questions:

- What are the physical structures and evolutionary processes behind galactic winds?
- What are the effects of radiative cooling on winds?

For this work, we use AREPO, a massively parallel simulation code that utilizes a moving, unstructured mesh defined by the Voronoi tessellation of discrete points (Springel 2010; Weinberger et al. 2020). The moving mesh approach offers a natural spatial adaptivity, where cells move and adjust their geometry with the wind flow, allowing for automatic adjustment of resolution and higher fidelity visualizations of the highest mass regions. This approach is meant to address the problem of overmixing commonly found in more traditional fixed-grid techniques and allow us to potentially study winds in significantly greater detail.

We proceed as follows. Chapter 2 develops the core physical ideas behind this thesis, comprising an introduction to thermally driven flows in Section 2.1, a discussion on entrainment of clouds and the entrainment problem in Section 2.2, an introduction to radiative cooling in Section 2.3, and how radiative cooling can form multiphase gas in Section 2.4. In Chapter 3, we describe our simulation setup, discussing our initial conditions in Section 3.1, the implementation of our feedback-driven wind model in Section 3.2, our radiative cooling routines in Section 3.3, and our refinement conditions in Section 3.4. In Chapter 4, we show and discuss our results, first focusing on spherically symmetric winds in Section 4.1, before discussing winds on a galactic disk in Section 4.2, and the effects of radiative cooling on winds in Section 4.3. Finally, in the Conclusion, we provide closing remarks and propose avenues for future work.

2 Theoretical Foundations

In this chapter, we develop the core physical concepts behind this thesis. In Section 2.1, we introduce the dynamics behind thermally-driven winds and how we can model their evolution using the CC85 model (Chevalier & Clegg 1985). In Section 2.2, we discuss the physics behind entrainment, as well as introduce the entrainment problem in the formation of cold phases. Section 2.3 then follows up on this by providing a brief synopsis on radiative cooling physics. Lastly, in Section 2.4, we discuss how radiative cooling can produce the multiphase gas found in galactic winds.

2.1 Thermally Driven Outflows

The energy needed to drive stellar-feedback driven winds can originate from a variety of sources, with the most prominent sources being those found in stellar cluster environments (Veilleux et al. 2020). For starburst galaxies in particular, the core feedback mechanism for driving winds is through thermal heating of the interstellar medium (ISM) by overlapping core-collapse supernovae (SNe) explosions within the galactic nucleus (Zhang 2018; Thompson & Heckman 2024). These SNe originate from massive stars that are between 8 and $25 M_{\odot}$ and typically explode between 4-40 Myr post-cluster formation. As they explode, they inject between ~ 1 to $10 M_{\odot}$ of metal enriched material with a kinetic energy of $KE = \sim 10^{51}$ erg into the ISM. SNe heating as a wind driver was first proposed in response to the discovery of extended X-ray emissions in low-mass starburst galaxies (Watson et al. 1984; Fabbiano & Trinchieri 1984). These heating processes have since received support via direct X-ray observations e.g. Strickland et al. (2000a), and are now considered to be a dominant wind driver in many hydrodynamic simulations e.g. Strickland & Heckman (2009); Schneider & Robertson (2018); Hopkins et al. (2012). Conceptually, the mass and energy released from the overlapping SNe collide with the ambient ISM, heating it and forcing a pressure gradient that accelerates gas outward. The outflowing wind forms a "wind-blown" superbubble that comprises the interior wind that is driven out by ISM heating, and is enveloped by a forward shock of CGM gas formed by the initial injection of mass and energy into an ambient medium. This shock is driven by the mass, energy, and momentum of the injected wind.

The exact physical processes regarding how mass, energy, and momentum from SNe can be mixed into the ISM and then launched outward as a wind is complicated and an active topic of research (Thompson & Heckman 2024). Nevertheless, it is possible to approximate the physics of SNe driven winds using simplified analytic models. The first such model was developed by Chevalier & Clegg (1985), henceforth referred to as the CC85 model, to describe the extended X-ray emissions of M82 (Watson et al. 1984). It assumes that wind velocities are high enough that gravitational effects are negligible and that the cooling is solely due to adiabatic expansion.

The CC85 model argues that under a continuous injection of mass and energy into the ISM, the thermalization of energy deposited by SNe creates an over-pressured region of hot gas that

accelerates a spherically symmetric wind outward via ram pressure. The wind dynamics can be characterized in terms of mass and energy injection rates \dot{M} and \dot{E} . The steady state flow of a wind that is driven by the injection of mass and energy into a starburst with injection radius R_{inject} can be described using the hydrodynamic equations ([Chevalier & Clegg 1985](#)):

$$\frac{1}{r^2} \frac{d}{dr} (\rho u r^2) = q \quad (2.1)$$

$$\rho u \frac{du}{dr} = -\frac{dP}{dr} - qu \quad (2.2)$$

$$\frac{1}{r^2} \frac{du}{dr} \left[\rho u r^2 \left(\frac{1}{2} u^2 + \frac{\gamma}{\gamma-1} \frac{P}{\rho} \right) \right] = Q \quad (2.3)$$

where r , u , ρ , P , γ are the respective values for radius, wind velocity, density, pressure, and adiabatic index. q and Q are the respective mass and energy efficiencies per unit volume. For $r < R_{\text{inject}}$, the injection efficiencies are set to $q = \dot{M}/V$ and $Q = \dot{E}/V$, where $V = \frac{4}{3}\pi R_{\text{inject}}^3$ is the volume of the starburst region defined by radius R_{inject} . For $r > R_{\text{inject}}$, no mass or energy is injected, so $q = Q = 0$.

The corresponding analytical solution of Equations 2.1-2.3 can be written in terms of the Mach number $\mathcal{M} = v/c_s$ for a given sound speed c_s . To solve for \mathcal{M} , we impose a boundary at $\mathcal{M}(r = R_{\text{inject}}) = 1$ so that the wind undergoes a smooth transition from subsonic flow for $r < R_{\text{inject}}$ to supersonic flow for $r > R_{\text{inject}}$. We then have a piece-wise solution for \mathcal{M} that depends on radius r :

$$\left(\frac{3\gamma + 1/\mathcal{M}^2}{1 + 3\gamma} \right)^{-\frac{3\gamma+1}{5\gamma+1}} \left(\frac{\gamma - 1 + 2/\mathcal{M}^2}{1 + \gamma} \right)^{\frac{\gamma+1}{2(5\gamma+1)}} = \frac{r}{R} \quad (r < R) \quad (2.4)$$

$$\mathcal{M}^{\frac{2}{\gamma-1}} \left(\frac{\gamma - 1 + \frac{2}{\mathcal{M}^2}}{1 + \gamma} \right)^{\frac{\gamma+1}{2(\gamma-1)}} = \left(\frac{r}{R} \right)^2 \quad (r \geq R) \quad (2.5)$$

The wind velocity v and sound speed c_s can now be written in terms of \mathcal{M} ([Nguyen et al. 2023](#)):

$$v = \mathcal{M} \left(\frac{\dot{E}}{\dot{M}} \right)^{\frac{1}{2}} \left(\frac{(\gamma - 1)\mathcal{M}^2 + 2}{2(\gamma - 1)} \right)^{-\frac{1}{2}} \quad (2.6)$$

$$c_s^2 = \left(\frac{\dot{E}}{\dot{M}} \right) \left(\frac{(\gamma - 1)\mathcal{M}^2 + 2}{2(\gamma - 1)} \right)^{-1} \quad (2.7)$$

Density, pressure, and temperature are obtained from the continuity equation:

$$\rho = \frac{\dot{M}}{4\pi v R^3} \quad (r \leq R), \quad \rho = \frac{\dot{M}}{4\pi v r^2} \quad (r > R) \quad (2.8)$$

$$P = \frac{\rho c_s^2}{\gamma} \quad (2.9)$$

$$T = \frac{P\mu}{k_b \rho} \quad (2.10)$$

It is possible to parameterize the injection rates by introducing two dimensionless parameters. The first is known as the mass loading factor:

$$\beta = \frac{\dot{M}_{\text{wind}}}{\dot{M}_{\text{SFR}}} \quad (2.11)$$

The mass loading characterizes the mass outflow rate as a fraction of the star formation rate. The mass injection rate \dot{M} can then be written as ([Chevalier & Clegg 1985; Schneider & Robertson 2018; Schneider et al. 2020](#)):

$$\dot{M}_{\text{inject}} = \beta \dot{M}_{\text{SFR}} \quad (2.12)$$

Similarly, the energy loading factor is written as:

$$\alpha = \frac{\dot{E}_{\text{wind}}}{\dot{E}_{\text{SN}}} \quad (2.13)$$

This factor characterizes the rate of energy thermalization as a fraction of the energy released by SNe i.e. a thermalization efficiency. The energy loading factor allows us to write the energy injection rate as $\dot{E} = \alpha \dot{E}_{\text{SN}}$. To rewrite this injection rate in terms of the star formation rate, we make the assumptions that every supernova releases 10^{51} erg, that there is 1 supernova per 100 M_\odot , and M_{SFR} is written in units of $\text{M}_\odot \text{ yr}^{-1}$ ([Thompson et al. 2016](#)). This energy injection rate can then be rewritten as:

$$\dot{E}_{\text{inject}} = 3 \cdot 10^{41} \alpha \dot{M}_{\text{SFR}} \text{ erg s}^{-1} \quad (2.14)$$

When parameterized this way, we find that we can write Equations [2.6](#), [2.8](#), and [2.10](#) in terms of scalable predictions:

$$v = v_{\alpha=\beta} \left(\frac{\alpha}{\beta} \right)^{1/2} \quad (2.15)$$

$$n = n_{\alpha=\beta} \frac{\beta^{3/2}}{\alpha^{1/2}} \quad (2.16)$$

$$T = T_{\alpha=\beta} \left(\frac{\alpha}{\beta} \right) \quad (2.17)$$

where $v_{\alpha=\beta}$, $n_{\alpha=\beta}$, $T_{\alpha=\beta}$, are the corresponding values for velocity, number density, and temperature for $\alpha = \beta$.

The CC85 model has been able to reproduce the X-ray observations of the hot gas of M82 with a high degree of precision, with the hydrodynamic simulations of [Strickland & Heckman \(2009\)](#) being able to use it to constrain the hot $3 - 8 \cdot 10^7 \text{ K}$ flows of M82 to $\alpha \sim 0.3 - 1.0$ and $\beta \sim 0.2 - 0.6$. As such, it is widely considered to be a good model for describing adiabatic winds ([Zhang 2018](#)). However, due to its simplifying assumptions, the CC85 model has many clear limitations that prevent it from being able to explain non-adiabatic winds, particularly the cooler phases found in multiphase outflows. As such, galactic winds that take non-adiabatic processes such as radiative cooling into account are expected to have results that differ significantly from the CC85 model.

2.2 The Problem of Entrainment

Multiphase gas has been detected across many observational studies covering a wide variety of wavelengths, such as the JWST observations of M82 by [Fisher et al. \(2025\)](#) (infrared), the Chandra observations of NGC 253 [Strickland et al. \(2000b\)](#) (X-ray), and VLC H I studies of M82 by [Martini et al. \(2018\)](#) (radio). These studies consistent note the presence of accelerated cool clouds embedded within the hotter wind. Because of the high wind velocities relative to the clouds, it is traditionally believed that these cooler cloud phases were originally swept up from the ISM by the hot wind and then entrained, or accelerated outward via the transfer of momentum from the hot to the cold phase ([Veilleux et al. 2005; Thompson et al. 2016](#)).

However, this has proven to be extremely challenging to replicate in simulation studies e.g. [Zhang et al. \(2017\); Schneider & Robertson \(2017\)](#), where it has been consistently established that when winds take up ram pressure-driven cool clouds, they develop shocks that compress and shreds the clouds, leading to their eventual destruction via Kelvin-Helmholtz shearing and

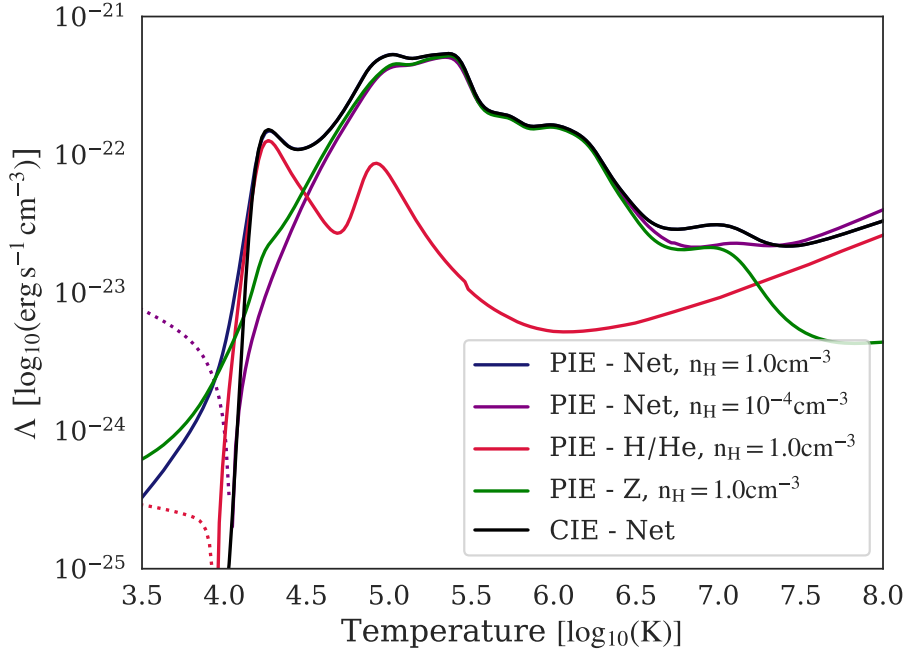


Figure 2.1. Cooling functions taken from the lookup tables of Wiersma et al. (2009), plotted as a function of temperature. We include the net cooling function for PIE cooling at density $n = 1 \text{ cm}^{-3}$ and $n = 10^{-4} \text{ cm}^{-3}$, as well as the total metallic and primordial components for $n = 1 \text{ cm}^{-3}$. The net CIE cooling function is also included. Dotted lines are used to represent negative cooling rates i.e. heating. Hydrogen is excited and ionized at $T \sim 10^4 \text{ K}$, and ionized at higher temperatures. The ionization of Hydrogen unbinds free electrons and enables the excitation of heavier atoms. Recombination and ionization between heavier ions lead to extensive cooling between $10^{4.5} - 10^7 \text{ K}$. For temperatures $T \gtrsim 10^7 \text{ K}$, nearly all gas is ionized, leading to Bremsstrahlung becoming the primary cooling mechanism. Metals enable new cooling avenues and drastically increase cooling efficiency compared to primordial gas. The inclusion of a UV background in the case of PIE results in heating at lower temperatures, as well as reduced cooling rates for lower density gas.

Rayleigh-Taylor fragmentation (Veilleux et al. 2020). To represent this in a scaling argument, the "cloud crushing" timescale on which a cloud with radius r_{cl} and density ρ_{cl} is destroyed is $t_{\text{cc}} \sim (\rho_{\text{cl}}/\rho_{\text{wind}})^{1/2}(r_{\text{cl}}/r_{\text{wind}})$. By comparison, the timescale needed to accelerate a cloud to wind velocities is $t_{\text{acc}} \sim (\rho_{\text{cl}}/\rho_{\text{wind}})(r_{\text{cl}}/r_{\text{wind}})$. The destruction timescale is therefore faster than the acceleration timescale by a factor of $(\rho_{\text{cl}}/\rho_{\text{wind}})^{1/2}$. Per Gronke & Oh (2020), $(\rho_{\text{cl}}/\rho_{\text{wind}})^{1/2} \sim 100 - 1000$. Therefore, clouds should be destroyed and mixed into the hot flow long before they can be accelerated to wind velocities. The "entrainment problem" represents a major unsolved conflict between theory and observation within galactic wind research. Much of the recent literature has been motivated to either develop a potential stabilization mechanism that can extend the lifetime of cool clouds, or explore alternative means of producing them.

2.3 Radiative Cooling

In this section, we provide a brief synopsis on radiative cooling, which plays a critical role in many aspects of galaxy formation. For galactic winds, radiative cooling is thus far the most successful

candidate as a potential stabilization mechanism for the entrainment of clouds, with recent cloud crushing studies e.g., Gronke & Oh (2018, 2020); Fielding et al. (2020) suggesting that it might be possible for a radiatively cooled cloud to not only survive, but also thrive, as they are entrained.

We start by defining a volumetric cooling rate C as the energy radiated away per unit volume and unit time (Schneider 2015). C is dependent on the gas metallicity, temperature, and density. As a standard practice, we quantify the extent of cooling by defining a cooling function (Mo et al. 2010):

$$\Lambda(n_e, n_{\text{H}}, T, Z) = \frac{C}{n_{\text{H}^+} n_e} \approx \Lambda(n_{\text{H}}, T, Z) = \frac{C}{n_{\text{H}}^2} \quad (2.18)$$

for an electron number density n_e , hydrogen number density n_{H} , and ionized hydrogen number density n_{H^+} . We assume that the gas is a quasi-neutral ionized plasma, such that $n_e n_{\text{H}^+} \approx n_{\text{H}}^2$. The cooling function has units $[\Lambda] = \text{erg s}^{-1} \text{cm}^{-3}$.

Generally, the radiative processes most relevant to the study of galaxy evolution are two-body collisions between free electrons and atoms, with the relatively low densities of galactic structures allowing us to ignore three or more body interactions (Mo et al. 2010). The four most important processes are:

- (i) Bremsstrahlung (free-free): A free election is accelerated by an ion and emits photons, resulting in cooling.
- (ii) Recombination (free-bound): A free electron recombines with an ion, radiating away its kinetic and binding energy.
- (iii) Collisional ionization (bound-free): A free electron impacts and unbinds an electron from an atom, radiating away its kinetic and binding energy.
- (iv) Collisional excitation (bound-bound): A free electron collides and knocks a bound electron to an excited state. The bound electron emits a photon as it decays.

We show various cooling functions as a function of the temperature in Fig. 2.1¹. At temperatures below 10^4 K, the gas is almost entirely neutral, such that collisional excitation is the dominant cooling process (Katz et al. 1996). Exciting hydrogen, which makes up the most common form of matter in the universe, requires a temperature of around $\sim 10^4$ K. As such, for a primordial composition i.e. made up entirely of H/He, cooling is highly inefficient below this temperature, and it is often the temperature floor for many astrophysical simulations. However, for enriched gases, cooling can still continue below $T \sim 10^4$ K, as collisions can still excite the fine structure levels of low ions (Mo et al. 2010). At higher temperatures, hydrogen becomes ionized, which unbinds more free electrons and enables the excitation and eventual ionization of heavier atoms. Excited atoms quickly return to a more stable state, and free electrons recombine with ions, resulting in significant cooling. Above $T \simeq 10^7$ K, excitation and ionization ceases, as even the heaviest elements are fully ionized. Thus, cooling is primarily driven via bremsstrahlung.

A very common simplification used in many simulations and theoretical models is to assume that the ionization and recombination rates are equal to each other, leading to a fixed abundance of ions (Wiersma et al. 2009). This assumption is referred to as ionization equilibrium, and is valid when the radiative timescales are much shorter than the hydrodynamical timescales (Mo et al. 2010). In the absence of an external radiation field, the cooling is said to be in collisional ionization equilibrium

¹<https://local.strw.leidenuniv.nl/WSS08/>

(CIE). While in CIE, radiative cooling is no longer dependent on density, as creation and destruction rates via collisions are now equalized with each other. The cooling function can be reduced to:

$$\Lambda(n_{\text{H}}, T, Z) \rightarrow \Lambda(T, Z) = \frac{C}{n_{\text{H}}^2} \quad (2.19)$$

However, while collisional ionization equilibrium is often assumed, it is well established by observations that the physical universe is permeated by a metagalactic UV background. This background field can ionize and heat gas via photoionization. For photoionization equilibrium (PIE), in which a gas maintains ionization equilibrium under photoionization, the cooling function can be written as:

$$\Lambda(n_{\text{H}}, T, Z) = \frac{C - \mathcal{H}}{n_{\text{H}}^2} \quad (2.20)$$

where \mathcal{H} represents the heating from the UV background. At low temperatures, photoionization leads to radiative heating. Additionally, it also suppresses the cooling rates of low density gas. Because of this, the PIE cooling function reintroduces density dependence ([Katz et al. 1996](#); [Wiersma et al. 2009](#)).

2.4 Radiative Cooling and Multiphase Gas

When radiative cooling is introduced, the formation of cold gas in winds can be facilitated in two different ways ([Veilleux et al. 2020](#)): (i) the survival of entrained cool clouds and (ii) A direct i.e. in-situ formation of cold gas from the wind. Note, however, that neither origin is mutually exclusive with the other. In actuality, it is quite likely that several mechanisms for cold gas need to be active in order to produce the multiphase structures found in observations ([Hopkins et al. 2012](#); [Veilleux et al. 2020](#)).

Entrainment of Cool Clouds

Recent breakthroughs in cloud crushing simulations e.g. [Gronke & Oh \(2018, 2020\)](#); [Fielding et al. \(2020\)](#) have demonstrated that radiative cooling can extend the lifetime of cool clouds. The initial crushing of cool clouds by the hot wind increases cloud densities, raising the cooling efficiency and allowing it to survive for longer periods of time ([Veilleux et al. 2020](#)). Furthermore, the relative shearing between the clouds and the wind creates an intermediate mixing layer between the wind and cloud while also ablating it, causing it to elongate and form a cometary tail ([Gronke & Oh 2020](#)).

It has been argued by [Gronke & Oh \(2018, 2020\)](#) that by itself, radiative cooling is often insufficient in preventing the destruction of cool clouds. However, efficient cooling of the warm intermediate mixing layer between the hot high-velocity wind medium and the tail can allow the cloud to survive and grow as it is entrained by the wind. The survival criterion is the ratio between cloud crushing time t_{cc} to the cooling time $t_{\text{cool,mix}}$ of the mixed layer, whose temperature can be written as a geometric mean, such that $T_{\text{mix}} \simeq (T_{\text{wind}} T_{\text{cloud}})^{1/2}$ and density $n_{\text{mix}} \simeq (n_{\text{wind}} n_{\text{cloud}})^{1/2}$ ([Begelman & Fabian 1990](#)). The critical cloud size beyond which clouds can survive is found by equating the two timescales to each other, and can be written as a column density ([Thompson & Heckman 2024](#)):

$$N_{\text{cl,grow}} \simeq n_{\text{cl}} r_{\text{cl}} \gtrsim \frac{k_{\text{B}} T_{\text{mix}}}{m_{\text{p}}} \frac{v_{\text{w}}}{\Lambda(T_{\text{mix}})} \simeq 5 \cdot 10^{18} \text{ cm}^{-2} \left(\frac{\alpha}{\beta} \right)^{1/2} T_{\text{mix},5.5} \Lambda_{-21.3} \quad (2.21)$$

for a given proton mass m_{p} and cooling function at mixing temperature $\Lambda(T_{\text{mix}})$. The entrainment mechanism for the cool clouds then becomes the transfer of mass and momentum to the cloud

via the mixing layer. Notably, this mixing is largely dominated by radiative cooling, which creates pressure gradients that can potentially siphon gas into the cloud and drive mass growth ([Gronke & Oh 2020](#)).

In-situ Formation from the Hot Wind

Another possible origin for cold gas was proposed by [Thompson et al. \(2016\)](#), who argue that cold gas can form in-situ via radiative cooling of a metal enriched hot wind. This process is expected to happen at larger distances, as the outflowing gas is initially too hot for any radiative processes outside of bremsstrahlung to be efficient. Moreover, the short advection time means that cooling is dominated by adiabatic expansion. However, cooling can become radiative once gas temperatures become sufficiently low to the point where metal-lines start to dominate the gas emissivity ([Thompson et al. 2016](#)). The transition point is defined by the cooling radius R_{cool} where $t_{\text{advec}} = t_{\text{cool}}$.

Modeling the in-situ formation of cold gas can be done by modifying the CC85 model to take radiative cooling into account. Using an approximated power-law for the cooling rate Λ and assuming a steady state flow for $r \gg R_{\text{inject}}$, the cooling time for a wind with metallicity ξ that is expanding into a solid angle Ω can be given as ([Thompson et al. 2016](#)):

$$t_{\text{cool}} \simeq 3 \cdot 10^6 \text{ yr} \frac{\alpha^{2.20}}{\beta^{3.20}} \left(\frac{R_{0.3}}{r_{10}} \right)^{0.27} \frac{R_{0.3}^2}{\dot{M}_{*,10}} \frac{\Omega_{4\pi}}{\xi} \quad (2.22)$$

where $R_{0.3} = R_{\text{inject}}/0.3 \text{ kpc}$, $r_{10} = r/10 \text{ kpc}$, $\dot{M}_{*,10} = \dot{M}/10 M_{\odot} \text{ yr}^{-1}$, and $\Omega_{4\pi} = \Omega/4\pi$. The advection timescale of a hot wind at radius r is given as:

$$t_{\text{advec}} \simeq 1 \cdot 10^7 \text{ yr} \left(\frac{\beta}{\alpha} \right)^{1/2} r_{10} \quad (2.23)$$

Setting these two timescales as equivalent to each other, the solution for the cooling radius can be approximated as ([Thompson et al. 2016; Schneider & Robertson 2018; Thompson & Heckman 2024](#)):

$$R_{\text{cool}} \approx 4 \text{ kpc} \frac{\alpha^{2.13}}{\beta^{2.92}} \mu_{0.6}^{2.13} R_{0.3}^{1.79} \left(\frac{\Omega_{4\pi}}{\xi \dot{M}_{\text{SFR},10}} \right)^{0.789} \quad (2.24)$$

Under this model, [Thompson et al. \(2016\)](#) proposed a process defined by two cool clouds transmigrations. The initial injection of mass and energy accelerates cold gas outward via ram pressure stripping. However, they are rapidly destroyed by fragmentation from Rayleigh-Taylor fragmentation and shearing from Kelvin-Helmholtz instabilities and merged into the hot wind. This introduces density perturbations to the wind and increases its mass load. Past R_{cool} , radiative cooling of the perturbed gas drives in-situ formation of multiphase gas beyond the cooling radius.

3 Simulation Setup

In this chapter, we describe the simulation setup used for this suite. In Section 3.1, we discuss the initial conditions, explaining its various components as well as the steps taken to prepare them for wind simulations. For Section 3.2, we describe the implementation of our feedback-driven wind model. In Section 3.3, we discuss the implementation of our radiative cooling routines. Finally, we review our refinement and derefinement conditions in Section 3.4.

Before proceeding, note that AREPO does not include temperature as an output field; it is instead derived from the specific internal energy u and electron abundance $x_e = n_e/n_H$ fields. The calculation for the temperature in Kelvin can be found on the IllustrisTNG website¹ and is included here for reference:

$$T[\text{K}] = (\gamma - 1)u/k_b \frac{\text{UnitEnergy}}{\text{UnitMass}} \mu \quad (3.1)$$

for adiabatic index γ , Boltzmann constant k_b in CGS units, and code units UnitEnergy and UnitMass. The mean molecular weight can be calculated from:

$$\mu = \left(\frac{4}{1 + 3X_H + 4X_H x_e} \right) m_p \quad (3.2)$$

where $X_H = 0.76$ is the hydrogen mass fraction. AREPO calculates and assigns $x_e = n_e/n_H$ to each cell when radiative cooling is enabled. For simulations without radiative cooling, we instead assume a constant $x_e = 1$. This equates to a dimensionless mean molecular weight of $\mu = 0.63$, corresponding to an almost entirely ionized gas at solar composition.

Unless stated otherwise, all simulations are run on a Voronoi moving mesh and periodic boundary conditions. However, the choice of boundary conditions is of secondary importance, as the box can be made sufficiently large such that edge effects do not affect our region of interest.

3.1 Initial Conditions

In this section, we describe the two initial conditions used for this project, which consist of: (i) an empty box consisting entirely of a diffuse circumgalactic medium-like background, and (ii) a box containing a diffuse CGM and a galactic disk embedded within the center. The CGM-only setup is used to study the structure and evolution of spherically symmetric outflows, while the setups containing a disk are used for all other simulations.

3.1.1 Galactic Disk

For simulations that include a galactic disk, we use static gravitational potentials to model the effects of both the disk and the dark matter halo. The disk component is represented by a Miyamoto-Nagai

¹<https://www.tng-project.org/data/docs/faq/>

disk potential, which is a function of the radial coordinate r and cylindrical height z (Miyamoto & Nagai 1975):

$$\Phi_{\text{stellar}}(r, z) = \frac{-GM_{\text{stars}}}{\sqrt{r^2 + \left(R_{\text{stars}} + \sqrt{z^2 + z_{\text{stars}}^2}\right)^2}} \quad (3.3)$$

for a given stellar disk mass M_{stars} , stellar scale radius R_{stars} and a disk scale height z_{stars} .

The dark matter halo interactions are represented using the NFW halo potential (Navarro et al. 1997):

$$\Phi_{\text{NFW}}(R) = \frac{-Gm_{\text{NFW}}(R)}{R} \quad (3.4)$$

where $m_{\text{NFW}}(R)$ is the enclosed mass within radius R . This enclosed mass depends on a critical density $\rho_{\text{crit}} = 3H^2/(8\pi G)$ and a characteristic density $\delta_c = 200c^3/[3\ln(1+c) - c/(1+c)]$ (Navarro et al. 1997). The halo concentration is calculated as (Schneider 2015):

$$c \approx 6.7 \left(\frac{M}{2 \cdot 10^{12} h^{-1} M_\odot} \right)^{-1} (1+z)^{-0.5} \quad (3.5)$$

For this work, we assume a redshift of $z = 0$, while the dimensionless Hubble constant is set to $h = 0.70$. In order to avoid close encounters and non-physical accelerations, we soften the halo potential with a length of $\epsilon = 0.01$ kpc for the small and medium scale disks and $\epsilon = 0.05$ kpc for large disks. The total static potential is then given as the $\Phi = \Phi_{\text{NFW}} + \Phi_{\text{stellar}}$.

Our implementation of the galactic disk closely follows the approach used in (Schneider & Robertson 2018), where a galactic disk with a defined mass of M_{gas} is embedded within the center of the simulation domain. The gas is radially distributed across a radius of $3R_{\text{stars}}$ using an exponential surface density profile:

$$\Sigma(r) = \Sigma_0 e^{-r/R_{\text{gas}}} \quad (3.6)$$

where $R_{\text{gas}} = 2R_{\text{stars}}$ is the scale radius of the disk gas, and $\Sigma_0 = \frac{M_{\text{gas}}}{2\pi r}$ is the central surface density.

The volume density of our disk can then be calculated as (Schneider & Robertson 2018):

$$\rho(r, z) = \rho_{[r,0]} \cdot \exp\left(-\frac{\Phi - \Phi_{[r,0]}}{c_s^2}\right) \quad (3.7)$$

where $\rho_{[r,0]}$ and $\Phi_{[r,0]}$ are the respective mid-plane density and total potential at $z=0$. The mid-plane density is calculated by dividing the surface density by the vertically integrated density profile such that (Schneider & Robertson 2018):

$$\rho_{[r,0]} = \frac{\Sigma(r)}{\int_{\infty}^{\infty} \exp\left(-\frac{\Phi - \Phi_{[r,0]}}{c_s^2}\right) dz} \quad (3.8)$$

for isothermal sound speed $c_s = (k_b T)/(\mu m_p)$, under the assumptions that the disk temperature is constant at $T = 10^4$ K and the mean molecular weight is $\mu = 0.60$, the expected value for an ionized gas with solar composition.

3.1.2 Circumgalactic Medium

For configurations that consist solely of uniform diffuse gas, we assign a number density of 10^{-4} hydrogen atoms per cubic centimeter to every individual cell. For configurations where we include the disk, we instead assign a number density of $6.15 \cdot 10^{-5} \text{ cm}^{-3}$. This value is $\sim 10^5$ smaller than the edge of the disk's mid-plane density, and is assigned to the background cells to better highlight the

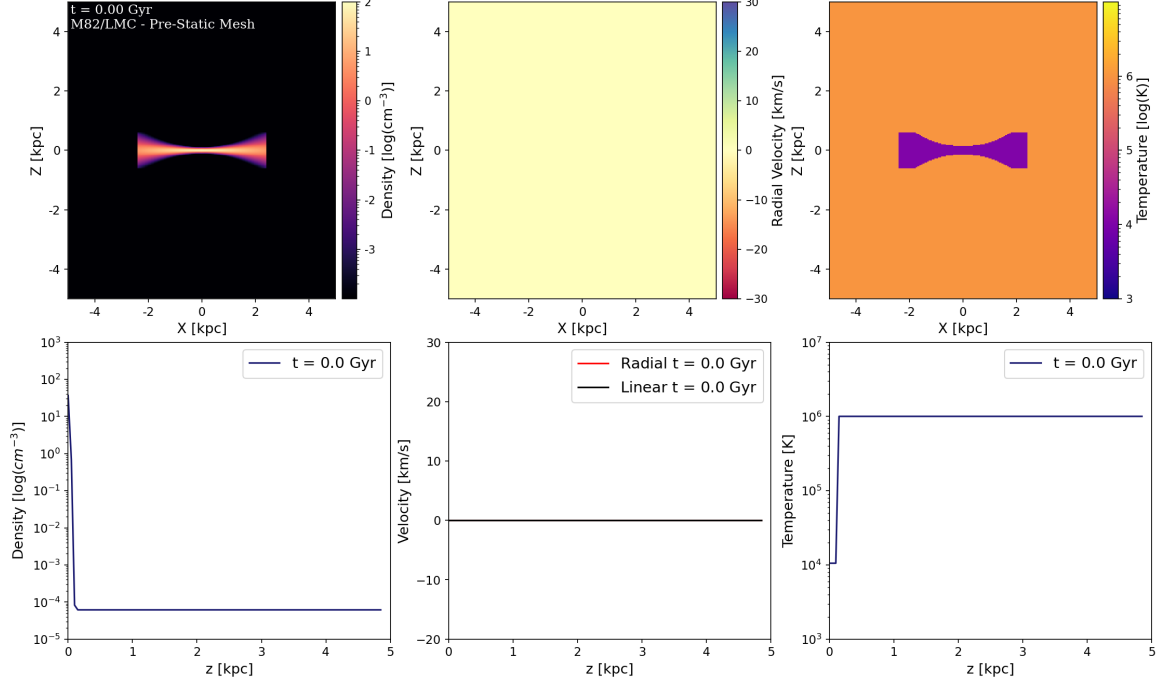


Figure 3.1. Central edge-on slices and vertical profiles of the LMC/M82-scale (see Table 3.1) disk’s number density (**left**), radial velocity (**middle**), and temperature (**right**) at the start of our two-stage relaxation procedure. At this stage, the disk has not settled into a stable equilibrium and is expected to undergo structural changes as we run the relaxation process.

effects of the disk on the outflowing wind. In both cases, we distribute to each cell a specific internal energy such that the temperature $T \approx 10^6$ K. The values chosen for the temperature and number density correspond to that of a warm outer galactic halo (Schneider & Robertson 2018; Fielding et al. 2017).

3.1.3 Creating the Initial Conditions

For CGM-only configurations, we distribute the gas across a 3D box that spans 30 kpc³. This box is divided into N_{dim} evenly sized cells along each dimension, such that the total number of cells is N_{dim}^3 . By default, the spherically symmetric tests are run on a box with $N_{\text{dim}} = 150$, for a box resolution of $\Delta x = 200$ pc.

For initial condition configurations that include a galactic disk, we instead divide the gas into two layers. The inner layer consists of a high-resolution box, which for the fiducial case spans 10 kpc³ with 301³ evenly spaced cells, giving us an initial resolution of $\Delta_{\text{in}}x = 33$ pc. This inner region is encased within a lower resolution padding region containing 50³ cells that extend outwards to form a 100 kpc³ box, for an initial ‘halo’ resolution of $\Delta_{\text{out}}x = 2$ kpc.

Similarly to Schneider & Robertson (2018), we assume that the disk is rotating and in radial equilibrium with the static potentials. The disk velocities are set by solving for the circular velocity v_θ from the radial acceleration due to the potential and pressure gradient:

$$a_r(r) = -\frac{d\Phi}{dr} + \frac{dP}{dr} \quad (3.9)$$

where $P = \rho c_s^2 / \gamma$. Here, the gas is assumed to be monoatomic, such that adiabatic index $\gamma = 5/3$.

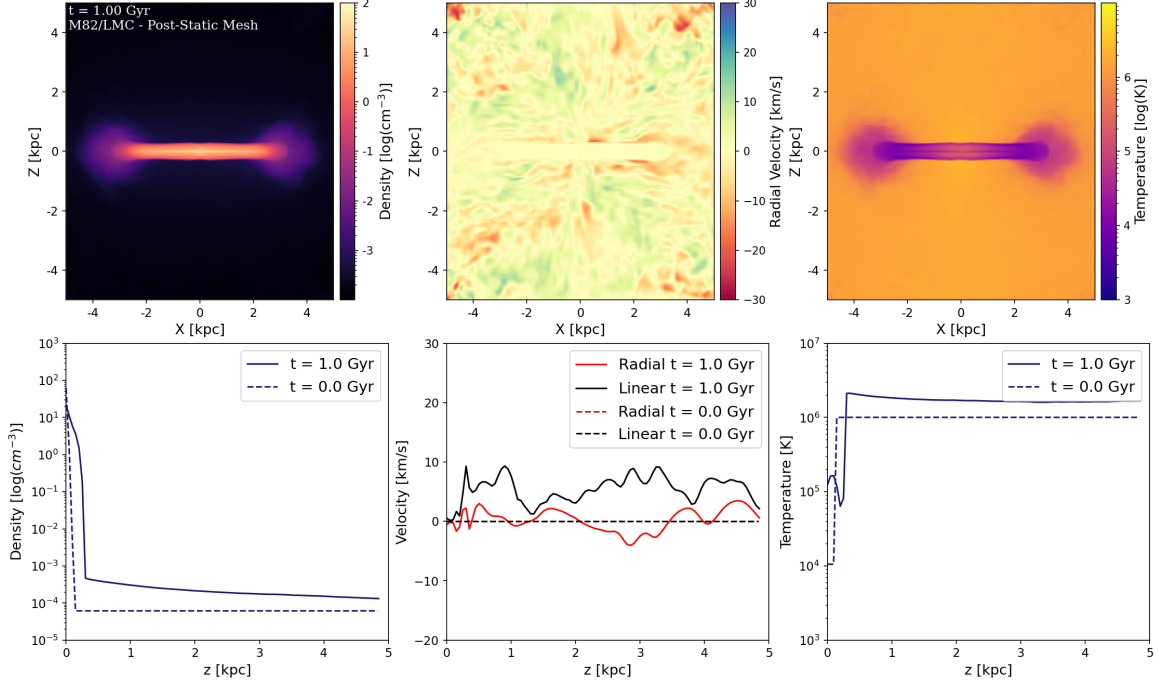


Figure 3.2. Central edge-on slices and vertical profiles of the LMC/M82-scale disk’s number density (**left**), radial velocity (**middle**), and temperature (**right**) after we have evolved the disk in a static mesh for 1 Gyr, i.e. the end of the first stage of our relaxation procedure. The disk has begun to settle into a stable equilibrium, but still contains potential transient features and artifacts.

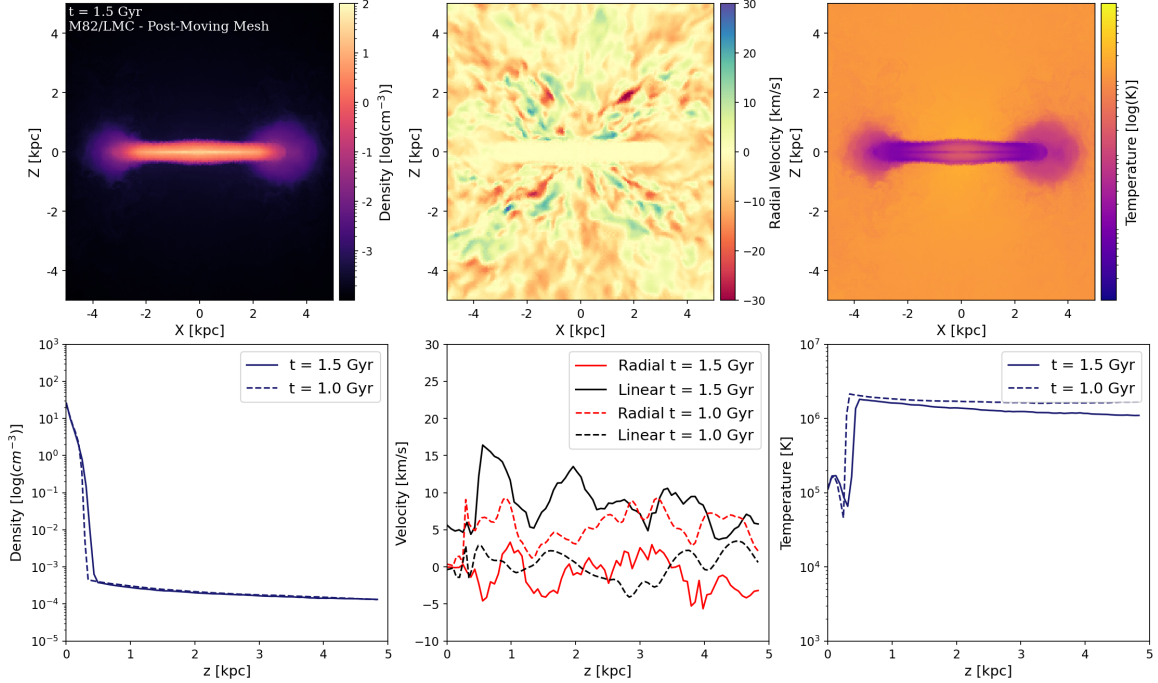


Figure 3.3. Central edge-on slices and vertical profiles of the LMC/M82-scale disk’s number density (**left**), radial velocity (**middle**), and temperature (**right**) after we enable a moving mesh and a mass-based refinement/derefinement operation and evolve the disk for an additional 500 Myrs. By this point, the disk has settled into a stable equilibrium and most transients have been removed from the disk.

Galaxy	T_{bg}	M_{stars}	M_{gas}	R_{stars}	z_{stars}	M_{200}	c_{NFW}
	[K]	M_{\odot}	M_{\odot}	[kpc]	[kpc]	M_{\odot}	
M82/LMC	1e6	1e10	2.5e9	0.8	0.15	5e10	10.0
MW	1.5e6	5e10	7.5e9	2.15	0.3	2e12	6.94
SMC	1e6	1e9	1.5e8	0.5	0.1	6.5e9	12.3

Table 3.1. Table of parameters used to characterize the initial structure of our galactic disk models. These values are: background/"halo" temperature, stellar mass, gaseous mass, stellar scale radius, stellar scale height, virial mass, and halo concentration. The values chosen are based on those found in galaxies on the scale of M82, the Milky Way, and the Small Magellanic Cloud.

The x and y components of the velocity in Cartesian coordinates can then be acquired as:

$$v_x = -v_{\theta} \frac{r_y}{r}, v_y = v_{\theta} \frac{r_x}{r} \quad (3.10)$$

To prepare the galactic disk for wind simulations, we employ a two-step relaxation process. Firstly, we evolve the disk (Fig. 3.1) on a static mesh for 1 Gyr (Fig. 3.2) to ensure that the gas reaches a stable equilibrium on a fixed grid. Afterwards, we turn on the moving mesh along with mesh refinement/derefinement, and evolve the disk for another 500 Myr (Fig. 3.3). This is done to ensure that the disk cells settle into their final positions (Fig. 3.4) and to remove transient features that might have arisen due to boundary and initialization artifacts. The result is our final initial condition. As seen in Fig. 3.4, turning on the moving mesh and relaxing the disk for another 500 Myr results in a cell configuration that consists of a high-resolution disk, and a lower resolution background and disk flare.

We use this two-step 'relaxation' procedure to make three initial conditions based on the galactic disks of: M82, the Milky Way (MW), and the Small Magellanic (SMC) Cloud. The parameters used for each galaxy can be found in Table 3.1 and are chosen based on a review of the literature (Licquia & Newman 2015; Rix & Bovy 2013; Hopkins et al. 2018; Bekki & Stanimirović 2009). The mid-plane radial profiles at each step of the process are shown in Fig. 3.5. Note that due to scale length of the Milky Way, the inner box was extended out to 15 kpc, divided into 451^3 cells.

3.2 Feedback-Driven Injection of Mass and Energy

We implement the feedback processes as injection routines, such that for every timestep Δt within a starburst duration of t_{burst} , a total of $M = \dot{M}\Delta t$ and $E = \dot{E}\Delta t$ is distributed across a central starburst defined by R_{inject} . Over the course of the starburst, a total of $M_{\text{tot}} = \dot{M}t_{\text{burst}}$ and $E_{\text{tot}} = \dot{E}t_{\text{burst}}$ is added into the system.

Our injection rates for mass and energy utilize the parameterization of the CC85 Model described in Section 2.1, with Equation 2.12 being the mass injection rate, and Equation 2.14 being the energy injection rate. For this work, we set the star formation rate to be constant at either $\dot{M}_{\text{SFR}} = 10 M_{\odot} \text{ yr}^{-1}$ for simulations where cooling is purely adiabatic or $\dot{M}_{\text{SFR}} = 20 M_{\odot} \text{ yr}^{-1}$ for simulations where we enable radiative cooling. The injection of mass and energy is then controlled by three core parameters: injection radius R_{inject} , mass loading factor β , and energy loading factor α . To further

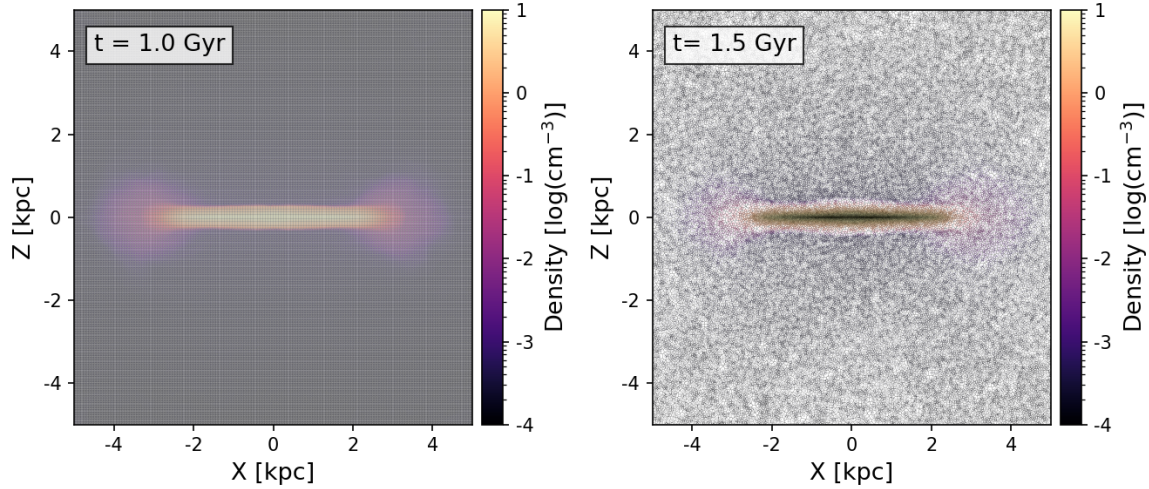


Figure 3.4. Voronoi diagrams of the gas cells of the LMC/M82-scale disk at the start of the moving mesh stage $t = 1.0$ Gyr (**left**), and the end of the moving mesh stage at $t = 1.5$ Gyr (**right**). At the start of the moving mesh stage, we still have a nested Cartesian grid. After evolving the disk for an additional 500 Myr, we end up with the high-resolution disk that is surrounded by a lower resolution background.

control our feedback model and study the effects of intermittent starbursts and duty cycles, we implement two temporal parameters: the starburst duration t_{burst} , and the duration between bursts t_{rest} .

We implement two different methods for distributing mass and energy. The first method evenly distributes a mean mass $M = \dot{M}\Delta t/n$ and mean energy $E = \dot{E}\Delta t/n$ for n cells inside $r \leq R_{\text{inject}}$. This approach assumes that all cells within the starburst region have roughly the same volume and cell size. While this is sufficient for non-radiative cooling simulations, simulations with radiative cooling enabled can potentially lead to the formation of small highly dense gas cells next to ones that are comparatively less dense. This can lead to some cells having a disproportionate amount of mass and energy injected into them. To fix this, we instead apply a volume-based injection scheme, where cells are weighed by their volume and normalized by the combined volumes of all cells where $r \leq R_{\text{inject}}$ such that $M = \dot{M}\Delta t V_{\text{cell}}/V_{\text{total}}$ and mean energy $E = \dot{E}\Delta t V_{\text{cell}}/V_{\text{total}}$.

3.3 Radiative Cooling Model

Our radiative cooling model is represented by the net cooling function:

$$\Lambda_{\text{net}} = \Lambda_{\text{prim}} + \Lambda_Z \quad (3.11)$$

Λ_{prim} is the cooling function for the primordial (H/He) gas; its cooling is already included in AREPO and uses the methodology described in Katz et al. (1996), and includes the effects of: (i) collisional excitation, (ii) collisional ionization, (iii) recombination, and (iv) free-free emission, or Bremsstrahlung such that:

$$\Lambda_{\text{prim}} = \Lambda_{\text{ex}} + \Lambda_{\text{ion}} + \Lambda_{\text{rec}} + \Lambda_{\text{ff}} \quad (3.12)$$

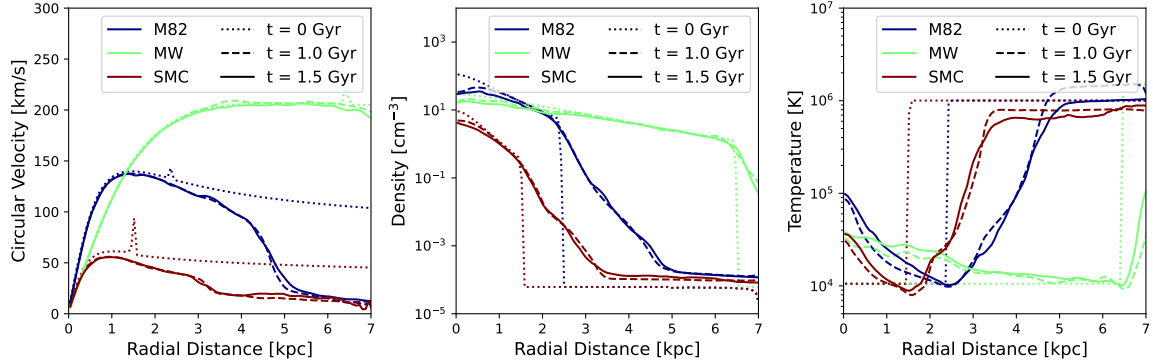


Figure 3.5. Radial profiles of our initial conditions, consisting of the rotational curves (**left**), number density (**middle**), and temperature (**right**). In order for the disk to settle into a state that is in hydrostatic equilibrium, we relax our initial IC with a two-stage procedure. First, we evolve the disk in a static mesh simulation, from $t = 0$ Gyr (dotted) to $t = 1$ Gyr (dashed). We then enable the moving Voronoi mesh, as well as refinement/derefinement operations, and evolve for a further $\Delta t = 500$ Myr (solid).

We implement the metallic cooling function Λ_Z using the approach for high-temperature metal line cooling found in Hopkins et al. (2018), where the metallic cooling function Λ_Z is given as:

$$\Lambda_Z = \frac{x_e}{x_{e,\odot}} \Lambda_{Z,\odot} \frac{Z}{Z_\odot} \quad (3.13)$$

We implement the metallicity Z as a passive scalar field that is transported by the gas. The initial values are distributed at the beginning of the simulation, with Z_{Disk} being assigned to disk cells while the background is assigned a metallicity of $Z_{\text{CGM}} = 0.1 Z_\odot$, corresponding to a mildly enriched CGM. We also assume that the outflowing mass will initially have the same metallicity as the galactic disk, and assign a metallicity of $Z_{\text{wind}} = Z_{\text{Disk}}$ to all mass injected into the starburst.

The solar values of the electron abundance $x_{e,\odot}$ and the cooling function $\Lambda_{Z,\odot}$ are acquired by running a linear interpolation scheme on the Cloudy tables provided by Wiersma et al. (2009)². For this work, we set the solar metallicity to $Z_\odot = 0.02$.

Our suite utilizes two cooling schemes: (i) Collisional Ionization Equilibrium (CIE), and (ii) Photoionization Equilibrium (referred in this work as either PIE or PIE+CIE). CIE cooling neglects the effects of a UV background, such that cooling is purely driven by collisional processes and depends only on metallicity and temperature (Wiersma et al. 2009). PIE cooling, on the other hand, does include the UV background, which heats the gas at low temperatures and severely suppresses the cooling rates of low density gas. As such, the implementation depends on both metallicity, temperature, and density (Mo et al. 2010). Furthermore, to prevent collapse of the galactic disk due to runaway cooling, we impose a temperature floor of $10^{3.5}$ K.

3.4 Refinement and Derefinement

We use AREPO’s default mesh de/refinement scheme, which refines or splits cells that have a mass that is more than twice the value of a given target mass criterion and derefines or deletes them if their mass is less than half of said criterion (Springel 2010). For this work, we opt for a target mass is a value that is less than or equal to the disk mass at $r = R_{\text{stars}}$.

²<https://local.strw.leidenuniv.nl/WSS08/>

To ensure that the starburst maintains a sufficiently high number of cells to sustain mass and energy injections, we implement another refinement scheme that refines all cells within $r \leq R_{\text{inject}}$ that are greater than a target volume. This refinement scheme also allows the winds to maintain a higher resolution even at distances that are far away from the central starburst.

4 Results and Discussion

Parameter	Description	Fiducial Value	Range
α	Energy loading factor	0.25	0.05-1.8
β	Mass loading factor	0.25	0.05-1.0
$\dot{M}_{\text{SFR}} [\text{ M}_\odot \text{ yr}^{-1}]$	Star Formation Rate	10	10-20
$R_{\text{inject}} [\text{kpc}]$	Injection radius	1.0	0.3-2.0
$t_{\text{burst}} [\text{Myr}]$	Starburst duration	100	15-100
$t_{\text{rest}} [\text{Myr}]$	Time between bursts	0	1-10
$M_{200} [\text{M}_\odot]$	Virial mass	5e10	6.5e9-2e12
c_{NFW}	Halo concentration	10.0	6.94-15.0
$Z_{\text{disk}} [\text{Z}_\odot]$	Disk metallicity	0.0	0.0-4.0
$Z_{\text{CGM}} [\text{Z}_\odot]$	CGM metallicity	0.00	0-0.1
$\Delta x [\text{pc}]$	Spatial resolution	33	33-300
N_{cells}	Cells per dimension	301	100-451
\vec{F}_G	Gas self-gravity	Off	Off/On
Λ	Radiative cooling	Off	Off/CIE/PIE

Table 4.1. Table of the key parameters that we vary across our simulations, along with their default fiducial values, and the range over which we vary them. The first set of parameters deal with feedback, the second with the initial conditions, and the third with additional physics. Our fiducial setup is that of a ‘medium-sized’ M82/LMC-scale disk with a 100 Myr starburst.

In this chapter, we present and discuss the results of the simulation suite. In Section 4.1, we study the case of spherically symmetric winds, first focusing on the case of CC85 winds, before including variations and modifications to the traditional CC85 model. In Section 4.2, we examine the effects of galactic disks on the structure and evolution of winds, including a discussion on how different disks and initial conditions can affect the evolution of winds across time. Section 4.3 examines winds under radiative cooling, starting with the formation and origins of cool gas in winds. Afterwards, we transition to discussing how variations in the loading parameters can affect the nature of cooled

Section/Subsection	Parameters	Fiducial Value	Values
4.1	$M_{\text{SFR}} [\text{M}_\odot \text{yr}^{-1}]$	10	
	Disk	None	
	Cooling	Off	
4.1.1	α	0.25	0.05–1.0
	β	0.25	0.05–1.0
	$R_{\text{inject}} [\text{kpc}]$	1.0	0.5–2.0
4.1.2	c_{NFW}	0	0–15.0
	$t_{\text{burst}} [\text{Myr}]$	50	15–50
4.2	$M_{\text{SFR}} [\text{M}_\odot \text{yr}^{-1}]$	10	
	α	0.25	
	β	0.25	
	$R_{\text{inject}} [\text{kpc}]$	1.0	
	$t_{\text{burst}} [\text{Myr}]$	100	
	Cooling	Off	
	Disk	M82	SMC, M82, MW
4.3	$M_{\text{SFR}} [\text{M}_\odot \text{yr}^{-1}]$	20	
	$R_{\text{inject}} [\text{kpc}]$	1	
	Z_{CGM}	0.1	
	Disk	M82	
4.3.1	Z_{disk}	4.0	0.25–4.0
4.3.2	α	0.9	0.9–1.8
	β	0.6	0.6–1.0
4.3.3	-	-	-
4.3.4	Cooling	PIE	PIE, CIE
4.3.5	$t_{\text{burst}} [\text{Myr}]$	50	1–50
	$t_{\text{rest}} [\text{Myr}]$	0	0–10

Table 4.2. Table of major parameters used in each section and subsection. Each set is separated into section and subsection subsets. The section subsets lists parameters that we hold constant across the entire section, and their fiducial values. The subsection subsets list the parameters that we examine in that subsection, the section’s fiducial value, and the range over which we vary them. The first set of parameters is used in Section 4.1, covering spherically symmetric winds. The second set is used in Section 4.2, focusing on winds on a galactic disk. The third set, used in Section 4.3, are for radiative cooled winds.

winds. This is followed by a close study of the nature of cold gas entrainment under CC85-type winds. We then compare the differences between CIE vs PIE based cooling models, before closing out the section by discussing the structure of cold gas and shock patterns in episodic starbursts.

The range of the controlling parameters within the simulation suite, along with the baseline values for each parameter, are listed in Table 4.1. The parameters analyzed in each section can be found in Table 4.2. The scripts and notebooks used to generate the plots, as well as the videos for each simulation, can be found at this [link](#).

4.1 Structure and Evolution of Spherically Symmetric Winds

In this section, we study the evolution of adiabatic spherically symmetric winds modeled using CC85. In subsection 4.1.1, we present and discuss the results of spherically symmetric winds, examining their radial and temporal evolution, as well as their variability across control parameters. In subsection 4.1.2, we transition our focus to beyond CC85, looking at the effect of a background NFW potential on the wind flow as well as on the case of an intermittent starburst.

4.1.1 Evolution of CC85 Winds

This subsection discusses the simple case of a continuous injection of mass and energy into a spherical starburst placed within the center of a CGM-like background of 10^{-4} cm^{-3} . We start by examining the case of a steady state wind and how it compares to the CC85 analytic solution. We then look at the temporal evolution of the wind, focusing on how the wind-blown superbubble forms and evolves at earlier times. Lastly, we examine the variability of the wind across different loading parameter and injection radius configurations. We adopt the fiducial energy and mass loading parameters $\alpha = \beta = 0.25$, along with a starburst radius of $R_{\text{inject}} = 1.0 \text{ kpc}$, and maintain a star formation rate of $\dot{M}_{\text{SFR}} = 10 M_{\odot} \text{ yr}^{-1}$.

We show the steady state of the wind flow at $t = 50 \text{ Myr}$ in Fig. 4.1, consisting of the central edge-on slice histograms for the number density, radial velocity, and temperature on the top row, along with their respective radial profiles on the bottom row. We include a vertical dashed line at $r = R_{\text{inject}}$ to mark the boundaries between the starburst and the wind. We note that for $r \leq R_{\text{inject}}$, the injected mass and energy create a hot, nearly isothermal gas region with a density profile that declines with distance, demonstrating a decreasing pressure gradient per the ideal gas law. This pressure gradient causes the gas inside to accelerate, consistent with that of a thermally driven flow. Beyond $r > R_{\text{inject}}$, the injected energy is transformed into bulk-motion (Veilleux et al. 2020), giving rise to a ram pressure that accelerates the gas to supersonic values towards an asymptotic velocity v_{∞} . As the gas flows outward, its temperature and density decrease as it propagates away from the injection radius. Because there is no radiative cooling, this decrease in temperature is purely due to adiabatic expansion.

We plot the CC85 solution for density, velocity, and temperature onto their respective profiles. Beyond the sonic point at $r = R_{\text{inject}}$, the wind profiles are in near perfect agreement with the CC85 solutions. However, for $r < R_{\text{inject}}$, our results deviate from CC85, with density and velocity being slightly above their analytic result. Based on resolution convergence tests (see [link](#)), we attribute this to be a numerical artifact arising from an insufficient number of cells inside the starburst. To ensure that the starburst retains enough number of cells to sustain injection, we implemented adaptive mesh refinement to replace cells that have been pushed out by the outflow. However, an insufficiently

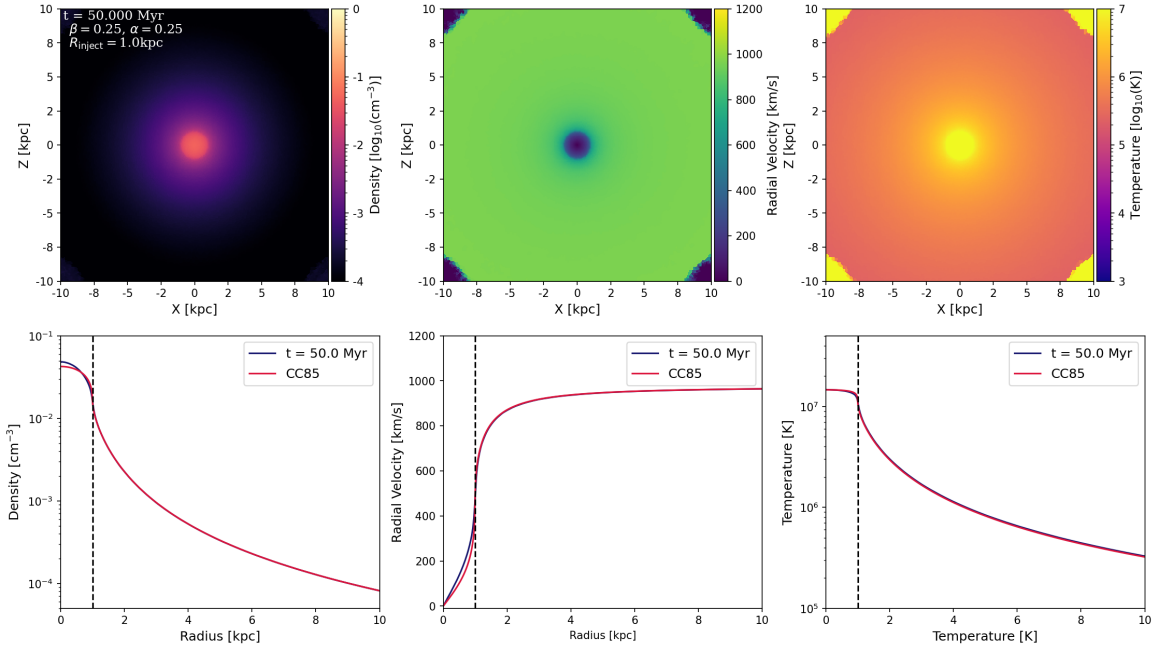


Figure 4.1. Edge-on slice and profiles of density (**left column**), radial velocity (**center column**), and temperature (**right column**) for the case of a spherically symmetric fiducial wind at steady state. The profiles consist of the median radial profile (blue), the corresponding CC85 solution (red), and a dashed black line indicating the injection radius $r = R_{\text{inject}}$. Inside R_{inject} , the gas is hot, dense, with subsonic velocities. For $r > R_{\text{inject}}$, the gas is driven outward as a wind via ram pressure and accelerated to an asymptotic velocity. The gas cools and becomes less dense as it propagates away from the injection radius, indicating adiabatic expansion. Our results correspond with the CC85 solution for $r > R_{\text{inject}}$, with minor inconsistencies in $r \leq R_{\text{inject}}$ due to numerical artifacts. The corner values in the slice plots are due to bounce-back effects from periodic boundary conditions.

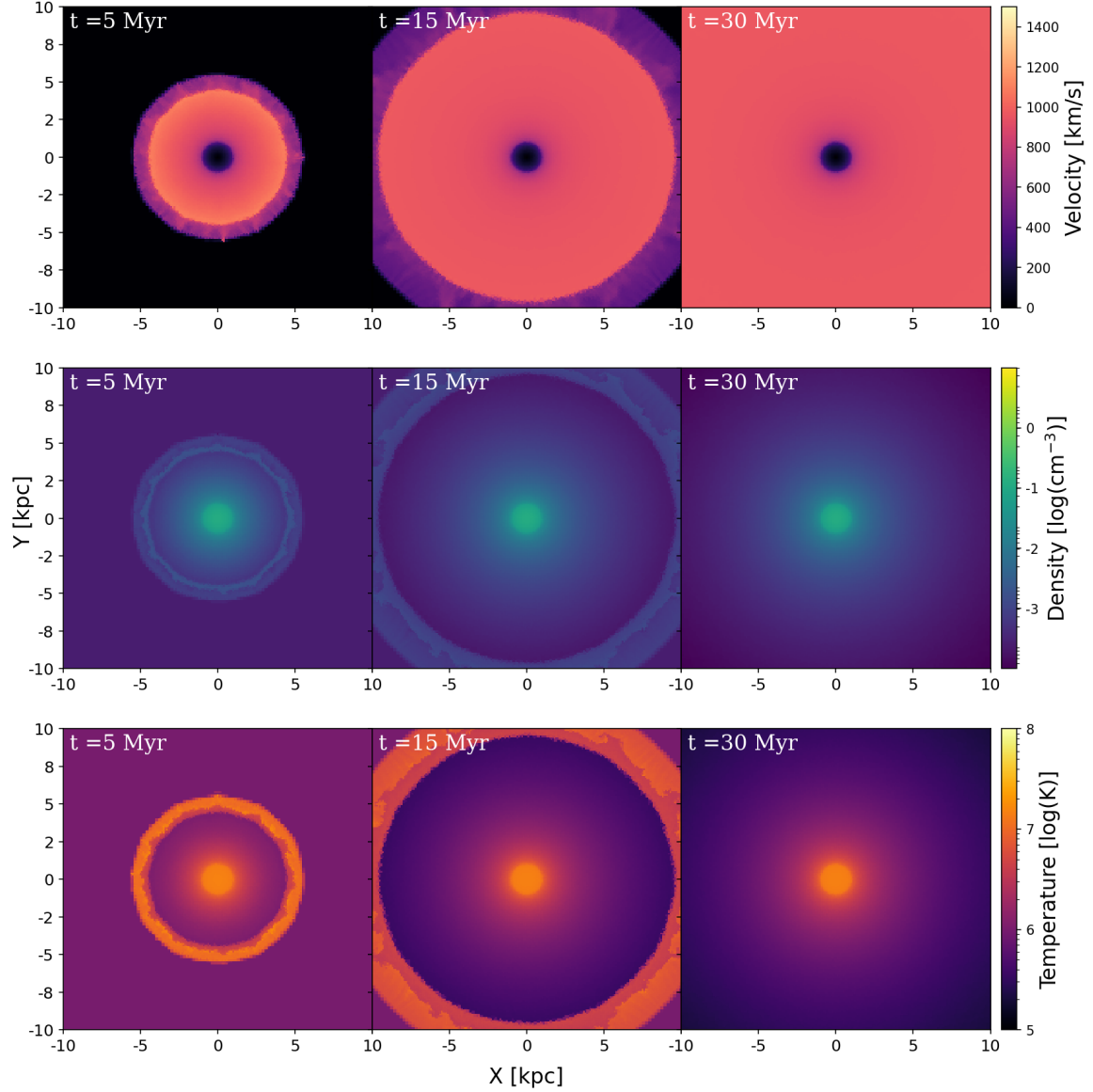


Figure 4.2. Temporal evolution of velocity (**top**), density (**middle**), and temperature (**bottom**) for the case of a spherically symmetric fiducial wind. Energy injection into the starburst creates a wind-blown bubble enveloped by a two-layer shock, consisting of an outer layer of shocked CGM gas and an inner layer of wind that is shocked upon contact with the CGM. The accelerating wind forces the shock outward, causing the bubble to expand and sweep up the ambient CGM gas. By $t = 30$ Myr, the shock blast has expanded beyond the bounds of our plots, leaving behind a spherically symmetric outflow at steady state.

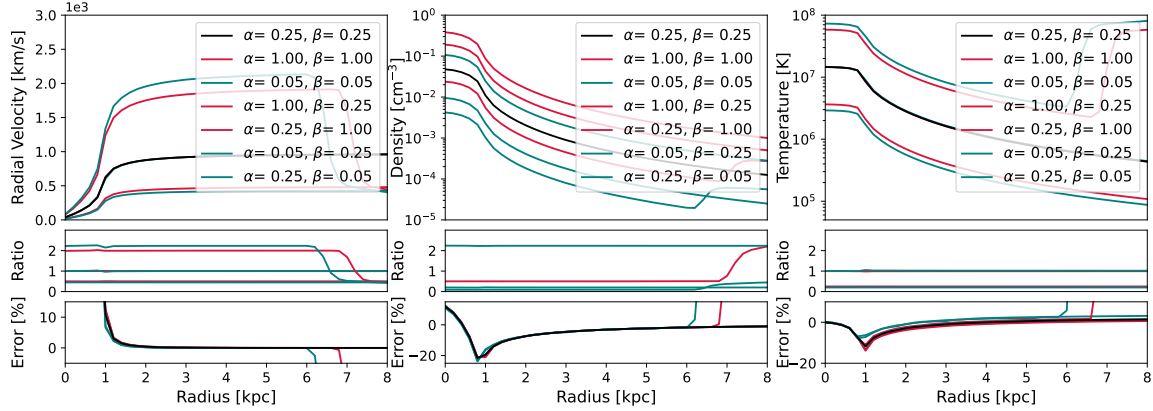


Figure 4.3. Time averaged radial profiles of the radial velocity (**left**) number density (**center**), and temperature (**right**) across 2 Myr for the case of varying load parameters. Inset plots consist of the ratio of each simulation’s radial profile to the fiducial (**middle**) and their % error from CC85 predictions (**bottom**). Line styles are used to represent the parameter varied for each run: dotted lines for mass load β , dashed lines for energy load α , and dash-dot lines for both. Colors are used to represent variations in each quantity: red lines for increases (4x) and teal lines for decreases (/5). Solid black lines are used to represent fiducial profiles. Each quantity has scaling relations that can be used to estimate their values using the fiducial result, with $v \propto (\alpha/\beta)^{0.5}$, $T \propto \alpha/\beta$, $n \propto \beta^{3/2}\alpha^{-1/2}$. We verify that the CC85 model is a good fit to our results in the region outside $r > R_{\text{inject}}$, with % errors $\gtrsim 10\%$ for $r < R_{\text{inject}}$ due to poor resolution within the starburst.

precise refinement criterion could lead to a poorly resolved starburst for $r < R_{\text{inject}}$, resulting in inconsistencies with the analytic solution. This artifact is not present in Sections 4.2 and 4.3, where we refine the starburst using a volume refinement scheme.

In Fig. 4.2, we examine the temporal evolution of a spherically symmetric wind. We establish that the injection of mass and energy creates a wind-blown superbubble. This bubble consists of the wind, which pushes the bubble outward, and an outer shock layer, called the forward shock or shock front. This shock front is formed by the shock heating of the background CGM by the initial mass and energy injection at $t = 0$ Myr, causing the shocked CGM to expand outward as a blast wave. At $t = 5$ Myr, the blast wave comprises dense, outward propagating gas with characteristic temperature $T \gtrsim 10^7$ K at a speed of ~ 800 km/s. As the wind flows away from the central starburst, the shock front expands and sweeps up ambient CGM gas. Aside from the shock front, we also note the presence of a "reverse" wind shock, where the colder, faster wind is decelerated and heated upon reaching the forward shock. The now shocked wind creates an interior layer of shocked gas with temperatures on the scale of $T \gtrsim 10^6$ K, and densities that are roughly 1 order of magnitude higher than the forward shock. At $t = 15$ Myr, we find that the inner wind has reached a steady state, while the shock bubble has nearly doubled in thickness from taking up ambient gas. Particularly, the shock velocities have decreased to ~ 500 km/s. We argue that this is due to the conservation of momentum, where the increased mass creates a "snowplow" effect that slows the shock down as it expands and takes up ambient gas (Veilleux et al. 2020). By $t = 30$ Myr, the outer bubble has expanded beyond the boundaries of our plots, leaving behind only the steady state wind.

To compare the variability between different configurations of mass load β and energy load α , we run a series of simulations where we increase either one or both parameters by a factor of 4, or decrease them by a factor of 5. For this, we maintain a constant injection radius of $R_{\text{inject}} = 1$ kpc. The

respective velocity, density, and temperature profiles of each test are plotted in Fig. 4.3. To compare how each simulation compares to our fiducial profile as well as to the CC85 predictions, we include insets where we plot the ratio of each profile to the fiducial and % error ($x_{\text{sim}} - x_{\text{CC85}}/x_{\text{CC85}}$ for quantity x). When we look at the profiles of each load configuration and their ratios to the fiducial wind profiles, it becomes apparent that each quantity has scaling relations that allow us to estimate the profiles of in terms of a base value with a reasonable degree of accuracy:

$$v_{\text{sim}} \simeq v_{\alpha=\beta} \left(\frac{\alpha}{\beta} \right)^{1/2} \quad (4.1)$$

$$n_{\text{sim}} \simeq n_{\alpha=\beta} \frac{\beta^{3/2}}{a^{1/2}} \quad (4.2)$$

$$T_{\text{sim}} \simeq T_{\alpha=\beta} \left(\frac{\alpha}{\beta} \right) \quad (4.3)$$

with $v_{\alpha=\beta}$, $n_{\alpha=\beta}$, $T_{\alpha=\beta}$ being the values for each quantity at $\alpha = \beta$. The wind velocities and temperatures are dependent on the energy to mass load fraction α/β , where a high energy to mass load results in a hotter, faster outflow, while a low energy to mass load ratio results in a slower, cooler outflow. Unlike the temperature and velocity, the density is more dependent on the mass load β than energy load α , with a large β being indicative of a high mass, and therefore high density wind. Significantly, the scaling relations are the same as the scaled CC85 equations 2.15, 2.16, and 2.17. At steady state, the terminal velocity for the CC85 wind is given at large distances is given as (Thompson & Heckman 2024):

$$v_{\infty} \simeq 1000 \frac{\text{km}}{\text{s}} \left(\frac{\alpha}{\beta} \right)^{1/2} \quad (4.4)$$

For $\alpha = \beta$ configurations, we find that $v_{\infty, \text{sim}} \simeq 1000 \text{ km/s}$, which is the expected value for a CC85 wind for equivalent loading factors. Thus, we verify that the CC85 model is a good predictor for the suite's spherically symmetric winds. Looking at the % error, we can see that this is indeed the case for $r > R_{\text{inject}}$. However, we find that the % error is $\gtrsim 10\%$ for $r < R_{\text{inject}}$. As before, we attribute this to be a numerical artifact due to a low number of cells within the starburst.

In Fig. 4.4, we examine how doubling and halving the injection radius R_{inject} can affect the wind evolution. Examining their profile lines and ratios to the fiducial, we find that the starburst temperature remains quasi-isothermal irrespective of R_{inject} . The density profile becomes more uniform with a mean density that is ~ 4 times less than the fiducial density. The more uniform density profile indicates a weaker pressure gradient. Consequently, the acceleration of the gas in the extended starburst is half that of the fiducial. By contrast, halving R_{inject} from 1 kpc to 0.5 kpc has the exact opposite effect on velocity and density. Note that for a CC85 type wind, the density of the central starburst scales with $\rho \propto v^{-1} R_{\text{inject}}^{-3}$ (see equation 2.8). As the acceleration and therefore the velocity are halved for $r = 0 - 1$ kpc, the gas density only decreases by a factor of 4 rather than 8. For $r \geq R_{\text{inject}}$, we find that the velocities for all three simulations converge to $v_{\infty} \simeq 1000 \text{ km/s}$ by $r = 7$ kpc, with the lower injection radii corresponding to faster accelerations. The densities converge with the fiducial profile for $r > R_{\text{inject}}$. A larger injection radius results in a hotter outflow, while a smaller one results in a cooler one. As we've established that the CC85 model is a good fit for our wind, we can use the pressure scaling $P \propto r^{-10/3}$ (Veilleux et al. 2020) and $\rho \propto r^{-2}$ to derive the temperature scaling, arriving at $T \propto P/\rho \propto r^{4/3}$. Analytically, $T_{R=2}/T_{R=1} \sim 2.52$ and $T_{R=0.5}/T_{R=1} \sim 0.4$. These values align with our corresponding simulation temperature ratios for $r > R_{\text{inject}}$. Compared with the CC85 model, it is shown that a larger R_{inject} reduces the % error within the starburst. We

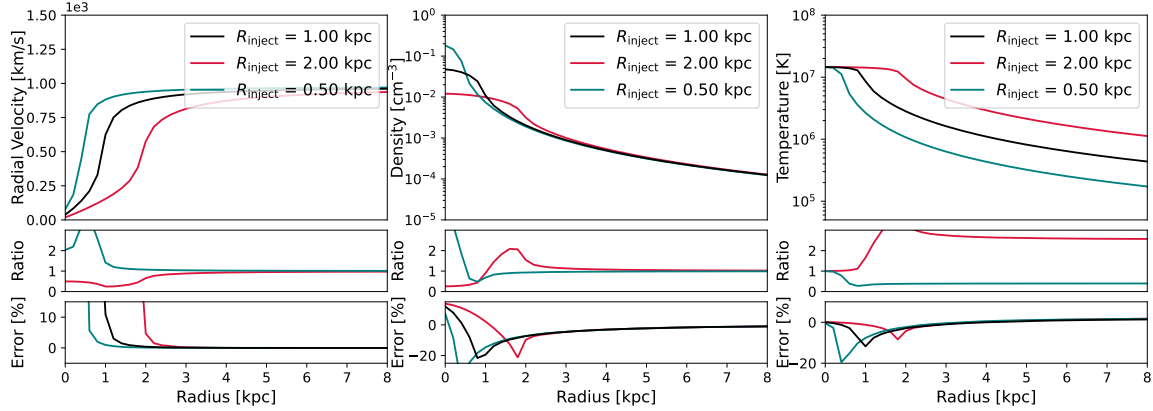


Figure 4.4. Time averaged radial profiles of the radial velocity (**left**) number density (**center**), and temperature (**right**) across 2 Myr for the case of varying R_{inject} . Inset plots consist of the ratio of simulation to the fiducial (**middle**) and their % error from CC85 predictions (**bottom**). Increasing R_{inject} results in a starburst that has a smoother velocity gradient, lower density, and an extended nearly isothermal region. Decreasing R_{inject} has the opposite effect. Outside R_{inject} , the radial velocity and density converge onto their fiducial result. Larger starbursts lead to hotter winds, while smaller starbursts lead to cooler ones. Gas inside $r < R_{\text{inject}}$ is better resolved with CC85 for larger radii.

argue that this is because the reduced acceleration leads to more cells remaining inside the starburst, allowing for better resolution with the CC85 predictions.

4.1.2 Energy Injection Beyond CC85

In this subsection, we look at extensions to the spherically symmetric wind by examining a gravity appended CC85 wind, along with an intermittent 15 Myr starburst.

Gravity on a Spherically Symmetric Wind

To study how gravity affects a CC85 wind, we add a static NFW potential which represents a background dark matter (DM) halo (see equation 3.4). The strength of the gravitational field is modulated by a halo concentration c which controls the halo density $\delta_c = 200c^3/[3\ln(1+c)-c/(1+c)]$, with a halo mass of $M_{200} = 1.5 \cdot 10^{12} M_\odot$. We compare three simulations: the fiducial with no halo, a Milky Way-like halo potential with concentration $c = 7.5$, and a dense, overly concentrated halo with $c = 15$. Their respective velocity profiles are shown in Fig. 4.5, where we measure the velocity slope from $r = 4 - 10$ kpc. Note that we do not show density and temperature as we do not see notable differences at steady state. We find that gravity initially doesn't affect the outflow as it leaves R_{inject} due to the initial wind acceleration being much higher than the deceleration due to gravity. However, as the wind plateaus towards an asymptotic velocity, gravity has a reductive effect on the velocity. Beyond $r \geq 4$ kpc, the slope of the velocity profile is flattened for the case of the Milky Way potential and negative for a highly concentrated halo. Therefore, we conclude that inclusion of a gravitational potential provides a higher order correction to the CC85 model, which neglects the impact of gravitational forces. This correction leads to a slight deceleration in wind velocity instead of plateauing towards an asymptotic velocity.

We comment that we also ran simulations where we turned on self-gravity, allowing the outflow and starburst to exert a gravitational pull onto themselves. However, we did not notice significant

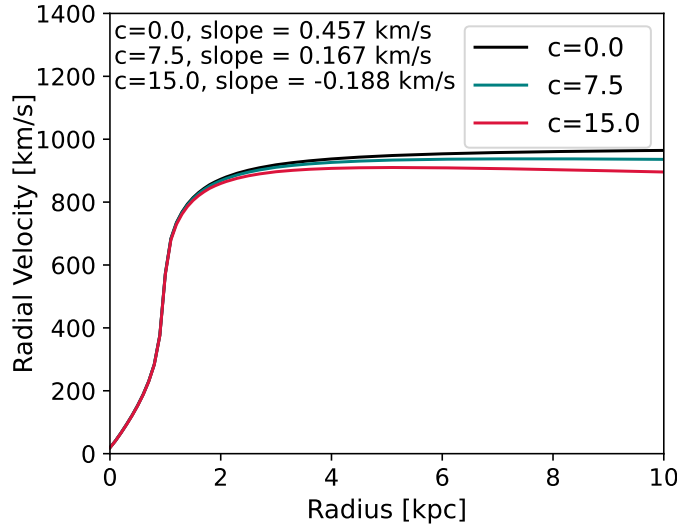


Figure 4.5. Radial profiles of the radial velocity, comparing the impact of gravity from a background NFW potential in steady state outflows, comparing: no gravity ($c = 0$), a Milky Way-like halo potential ($c = 7.5$), and an overly concentrated halo ($c = 15$). The halo potential has a reductive effect on the velocity as the wind propagates outward, with the strength of reduction increasing with halo concentration. For $r > 4$ kpc, the velocity profile is flattened for the case of a Milky Way-like potential, and negative for a highly concentrated halo.

differences in the wind profiles, and the case where we include both self-gravitation and an NFW potential reverts back to the spherically symmetric case. This is likely due to our periodic boundary conditions, where the mean density is subtracted from the density field in order to obtain a finite solution for the Poisson equation for self-gravity $\nabla^2\Phi = 4\pi G(\rho - \langle\rho\rangle)$ (Springel 2010; Mandal et al. 2023). For a spherically symmetric wind and potential, the system density is equal to the mean density for a given radius r . Ergo, the gravitational effects are canceled out and the wind properties are similar to the non-self gravity case. However, we note that density and velocity perturbations develop as the wind flows outward. This could be due to the outflow not having a perfect sphericity, or alternatively due to bounce-back effects at the boundaries rendering the wind non-spherical.

The Case of an Intermittent Starburst

In Fig. 4.6 we plot the velocity, and temperature profiles for an intermittent starburst that lasts for 15 Myr, followed by a 30 Myr rest state. During the starburst duration, the evolution of the starburst is the same as the fiducial simulation. After turning off the injection routine, gas densities, and temperatures fall to a uniform floor value that is at rest. As this process starts from R_{inject} and then moves outward, wind far away from the starburst will still flow outward at high velocities. Once they hit the edges of the box, they cause a bounce-back due to periodic boundary conditions. As there is no outflow to counteract the inflow, the bounce-back becomes the dominant feature at $t \geq 35$ Myr. We note that this feature is transient, and over time the gas will settle into a new uniform steady state across the entire simulation domain.

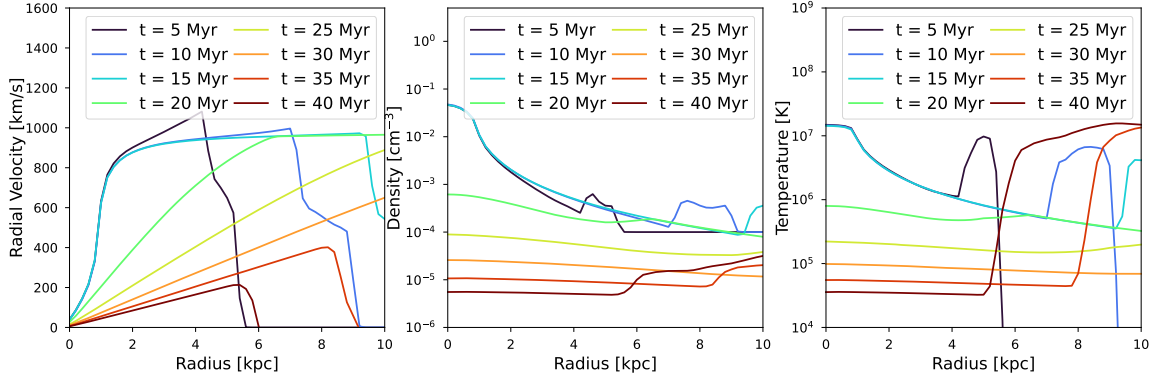


Figure 4.6. Time evolution of the radial profiles of velocity (**left**), density (**middle**), and temperature (**right**) for a single intermittent starburst that lasts for 15 Myr. During the starburst duration, the evolution of the outflow is equivalent to the fiducial. Post-starburst, the wind densities and temperature fall and settle into a uniform steady state with zero velocity. At times $t \geq 35$ Myr, a transient bounce-back effect forms due to wind interactions with the periodic boundaries.

4.2 Winds on a Galactic Disk

In this section, we examine the evolution of winds that emanate from a starburst embedded within a galactic disk. We first start by discussing the radial evolution of the wind at steady state. This is followed by a closer examination of the biconal structure of the wind, and how we choose to constrain our region of analysis going forward. We then study the temporal evolution of the wind, looking at how different disk models can affect the structure and evolution of the flow. Lastly, we compare and contrast our moving mesh results with those of a static mesh simulation. For this section, we set the fiducial mass and energy load to $\alpha = \beta = 0.25$, starburst radius $R_{\text{inject}} = 1.0$ kpc, $\dot{M}_{\text{SFR}} = 10 M_{\odot} \text{ yr}^{-1}$. For our fiducial initial condition, we adopt the disk parameters based on the M82 disk (see Table 3.1), as it is the most extensively studied starburst galaxy in the literature.

In Fig. 4.7, we show the steady state outflow at $t = 100$ Myr, with the panels consisting of central edge-on slices of number density, radial velocity, and temperature in the top row, and their respective radial profiles on the bottom row. We find that at steady state, the wind develops a bicone-like morphology that is centered around the Z-axis. For the fiducial parameters, the bicone has an opening angle of $\sim 120^\circ$, and consists of two layers. The inner layer, referred to as a "free wind" layer by Schneider & Robertson (2018), has lower density and temperature, as well as a higher velocity. This free wind layer is surrounded by an outer layer of which contains hotter, higher density gas that is somewhat slower than the inner bicone. This is referred to as a turbulent interface that forms due to shearing instabilities between the radially moving wind and the rotating disk. Beyond the opening angle, we find that the outflow has begun to shred and ablate the disk, creating a slower, dense turbulent interface that contains a mixture of colder temperatures. The biconal morphology has been produced across a wide range of observations and simulations alike (Veilleux et al. 2020; Schneider & Robertson 2018). Per Nelson et al. (2019), the formation of the bicone is an emergent feature formed from hydrodynamical collimation, and is a 'path of least resistance' effect. Winds that are directed within the same plane as the disk experience the most resistance due to the high densities of the disk, forcing the wind to travel outward as a bicone. The free wind travels along the path of least resistance, and their wind flow, as indicated by the Z-axis,

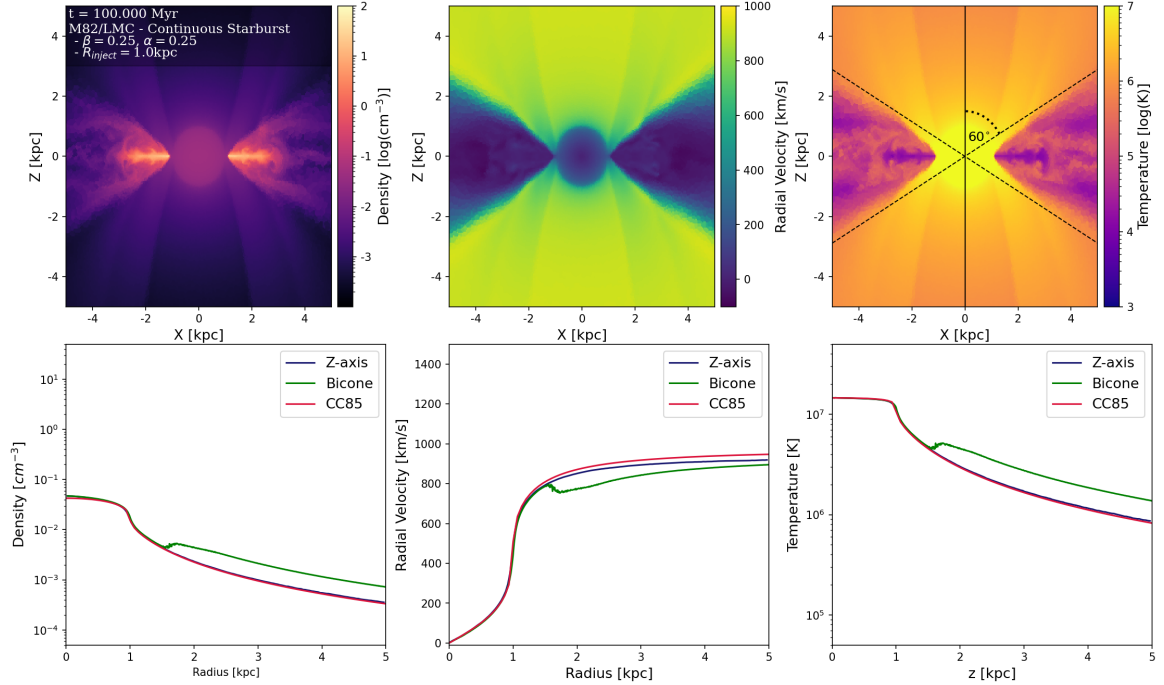


Figure 4.7. Edge-on slice and profiles of density (**left column**), radial velocity (**center column**), and temperature (**right column**) for the case of a wind being driven from a starburst embedded within an M82 disk at steady state. The profiles consist of the median radial profile of the vertical z-axis (**blue**), the corresponding CC85 solution (**red**), and the region bounded by a bicone of $\sim 120^\circ$ (**green**). Hydrodynamical collimation due to resistance between the disk and wind forces the wind into a bicone morphology. The inner bicone, or "free wind", follows the CC85 model, albeit with slightly lower velocities due to gravitational effects from the disk and halo. The outer bicone deviates from the CC85 model and forms an intermediate layer of hot, denser with slightly lower velocities. Interactions between the winds in the flowing in the disk plane shreds the disk and creates a dense turbulent shear layer of mixed temperatures.

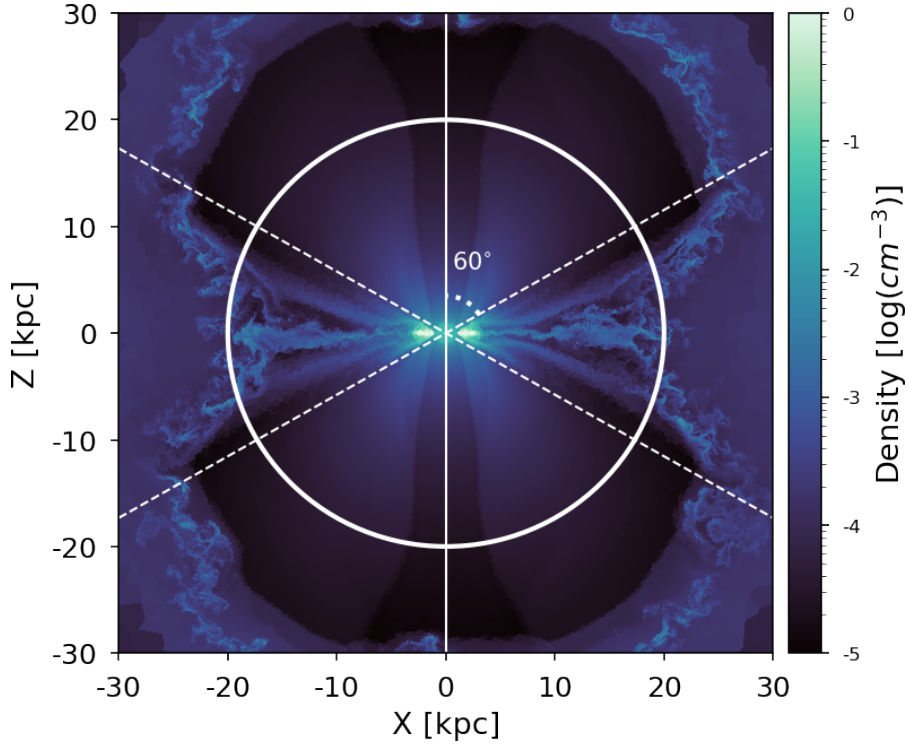


Figure 4.8. Edge-on density slice of the fiducial simulation at $t = 100$ Myr from $Z, X = -30$ to 30 kpc. At large distances, the biconical structure is somewhat curved, forming an hourglass-like shape. The resulting superbubble consists of a heavily mixed outer layer, a turbulent interface region that takes up most wind in the bicone, and collimated free wind. We overlay our standard region of analysis, which consists of a bicone with a 120° opening angle and extending outward to a radius of $r = 20$ kpc. We find that this region is sufficient to capture the overall structure of the wind in most cases.

largely follows that of CC85. However, due to gravitational effects from the disk and the halo, the radial velocities are slightly lower than their analytic predictions.

To study the wind densities in further detail as well as determine our region of analysis, we show a zoom-out of the density edge-on slice of the wind at $t = 100$ Myr spanning $Z, X = -30$ to 30 kpc at $t = 100$ Myr. Fig. 4.8. We find that this region captures most of the wind structure at this distance, which comprises a superbubble with an outer layer with extensive hydrodynamic instabilities, a turbulent interface region that comprises most of the wind contained within the bicone, and a highly collimated layer of free wind. Furthermore, we find that the biconical structure of the wind is somewhat curved at large distances, forming an hourglass-like structure as it propagates outward. To focus on the wind in future plots, we apply a filtering procedure where we filter out the disk by only considering cells within the $\sim 120^\circ$ bicone in Fig. 4.8. In most cases, we filter out gas at radii $r > 20$ kpc due to their low densities beyond this point. However, in some cases, we relax this filter in order to examine all wind cells contained within the $\sim 120^\circ$ bicone.

To compare how the wind evolution varies across different galactic disks, we show the temporal evolution of density for winds driven from starbursts embedded within the M82, Milky Way (MW), and Small Magellanic Cloud (SMC) disks in Fig. 4.9 (See Table 3.1 for the parameters used for each disk). Note that while all disks share the same loading parameters, we halve R_{inject} from 1 kpc to

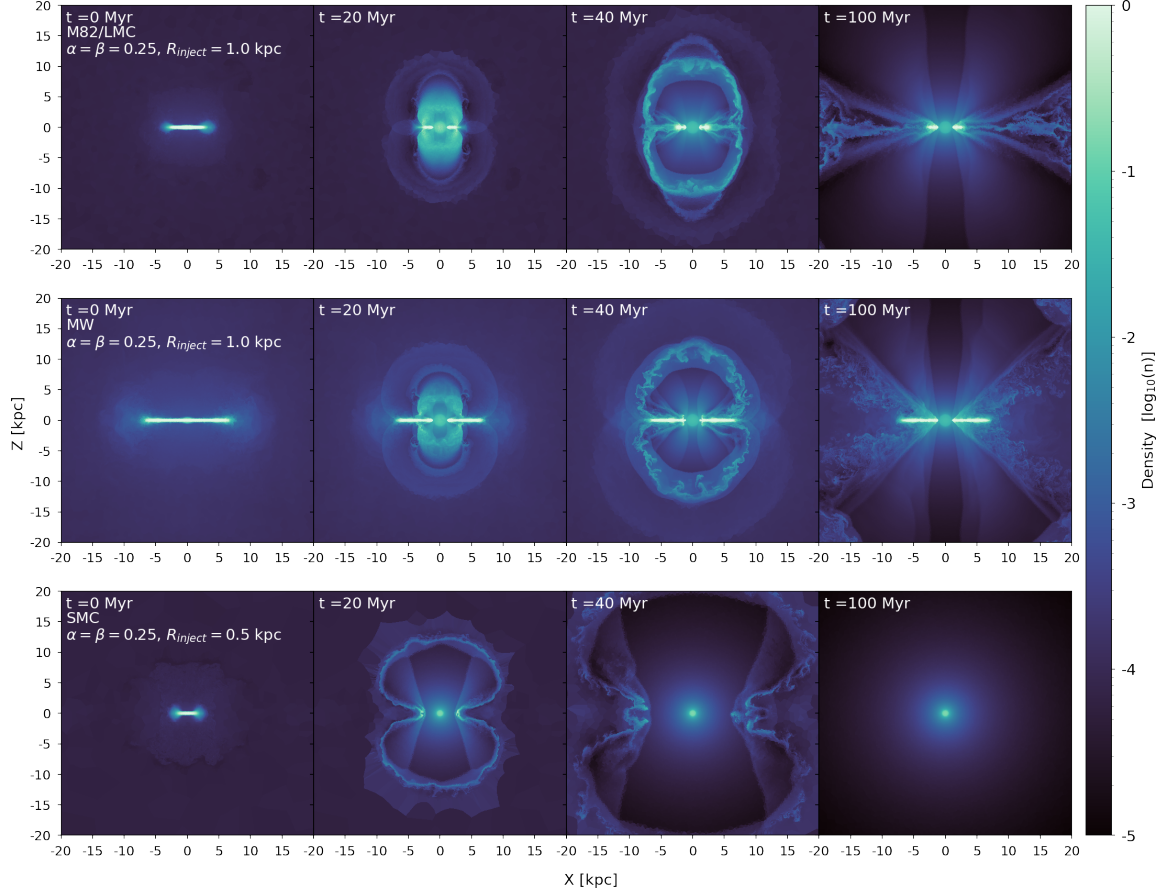


Figure 4.9. Time evolution of density with M82 (**top**), MW (**bottom**), and SMC (**right**) using the fiducial parameters. Note that $R_{\text{inject}} = 0.5 \text{ kpc}$ for the SMC due to the small size of the disk. For the M82 and MW disk, mass and energy injection drives a blast wave from the central starburst. Due to pre-existing disk gas, the starburst must maintain a continuous injection of mass and energy to accelerate the disk gas outward. This creates a multilayer superbubble which consist the forward CGM shock, a reverse shock from injected gas at $t = 0 \text{ Myr}$, outflowing disk gas, and wind. By $t = 40 \text{ Myr}$, a high density "disk" bubble forms and envelopes the wind. Stratification inside the disk bubble indicates possible Rayleigh-Taylor instabilities due to winds pushing against the bubble or Richtmyer-Meshkov instabilities resulting from the initial blast wave. Due to heavy resistance, acceleration is collimated in the Z-axis, with the larger, more massive disk forming a narrower bicone. The SMC disk is destroyed over time, and the system reverts to a CC85 wind solution. The likely reason is that the SMC's stellar and gas mass might be too low to sustain a long starburst.

0.5 kpc for the SMC due to its small size. We find that similarly to the spherically symmetric wind, the initial injection of mass and energy into the starburst drives a blast wave away from the central starburst. However, as the starburst is embedded within the center of a highly dense, cold disk, the initial acceleration of wind is delayed as the outflow must first inject enough mass and energy to drive a strong enough pressure gradient to push the disk gas within $r \leq R_{\text{inject}}$ outward. How long this takes depends on the disk. At $t = 20$ Myr, both the M82 and Milky Way starbursts are in the process of accelerating the gas from their respective disks outward. Due to the heavy resistance between the disk and the wind, their accelerations are collimated towards their respective Z-axis. Outflows from both disks form multilayer superbubbles, which consist of a low density forward shock, a reverse shock from injected gas at $t = 0$ Myr, the parts of the disk being pushed out, and the steady state wind. By $t = 40$ Myr, a disk "bubble" forms, sweeping up gas from the initial expansion. Due to the density contrast between the wind and the disk, it is unlikely that reverse wind shocks form between the two regions. However, the turbulent stratifications within the blown-out disk bubble demonstrates Rayleigh-Taylor instabilities, which might have formed from the wind constantly pushing against the bubble. Alternatively, the stratification could also partially originate from growing Richtmyer-Meshkov instabilities due to the blast wave from the early injections. At steady state, we find that the MW disk produces a narrower bicone than the M82. We attribute this to the MW disk being larger and more massive than that of M82, creating a more collimated bicone.

Unlike the M82 and MW, we find that the SMC disk is pushed out and destroyed by the wind at longer timescales, and reverting to a CC85-like wind. We believe that this could simply be due to the SMC disk mass being only $1.5 \cdot 10^8 M_{\odot}$, which is more than a factor of 10 smaller than the M82 disk. Thus, the SMC disk could potentially not have a sufficient mass to sustain a long starburst. Additionally, the low stellar mass of the SMC disk means that its stellar potential and rotation curve (see Fig. 3.5) is nearly 3 times smaller than M82's. Therefore, it is possible that a starburst-driven wind could disrupt the disk's rotation enough for it to become destabilized and shredded by the wind.

To examine the differences between the static and moving mesh, we prepared a static mesh initial condition of the M82 disk using an analogous approach to what was described in Subsection 3.1.3, where instead of turning on the moving mesh, we relax the disk in static mesh for 1.5 Gyr. We then use it to run a static wind simulation using the fiducial parameters, which is equivalent to a fixed Eulerian grid (Springel 2010). We compare the differences in mesh structure in Fig. 4.10. We find that allowing for cells to move with the flow creates a higher resolution disk and bicone, while cells outside the bicone, which have lower densities and weaker flows, have coarser resolutions and larger cell sizes. We note that the Eulerian fixed grid, by comparison, appears to have highly mixed disk-wind interactions and a more angular, narrow bicone rather than the hourglass shape of the moving mesh. From this, we conclude that the moving mesh approach allows for a more detailed visualization of the wind flow, as well as better representation of the disk-wind interactions compared to the static mesh.

4.3 Effects of Radiative Cooling on Galactic Winds

In this section, we introduce and discuss the effects of radiative cooling on winds. In Subsection 4.3.1, we discuss the general effects of radiative cooling, as well as the two origins from which the cold phases of multiphase gas can form. In Subsection 4.3.2, we study how varying the mass and energy loading parameters can affect the cooling efficiency and overall properties of radiatively

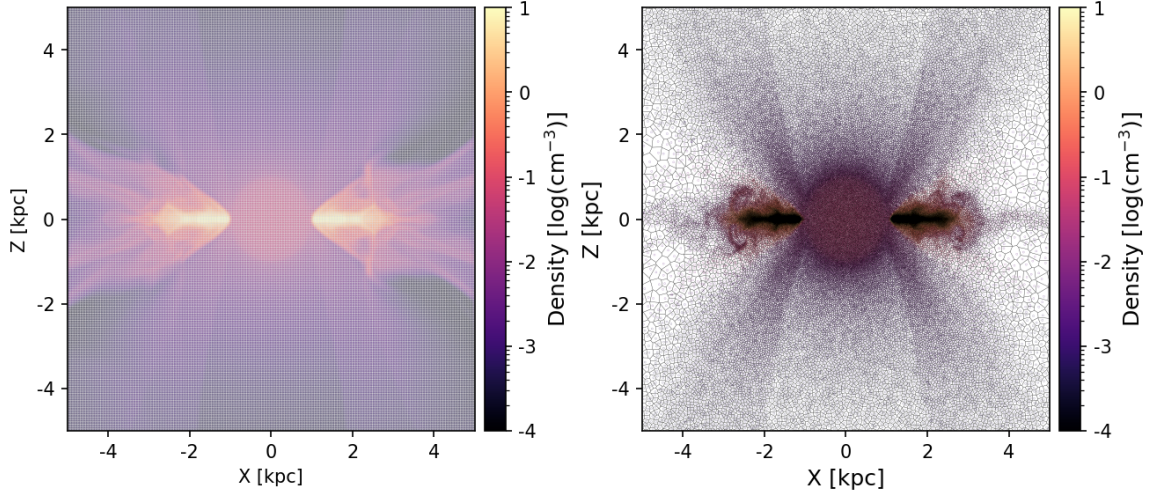


Figure 4.10. Voronoi diagram comparing the density and cell locations of a fiducial parameter simulation ran on a fixed Eulerian grid (**left**) vs one that uses a moving mesh approach and adaptive mesh refinement (**right**. Also see Fig. 4.7). Due to the density differences, the moving mesh creates a high-resolution disk and wind bicone, along with a lower fidelity background. The Eulerian fixed grid creates a highly mixed disk and a more angular, narrow bicone rather than the hourglass shape of the moving mesh. At the steady state, this leads to a loss in detail when compared to the moving mesh approach.

cooled winds. For Subsection 4.3.3, we conduct a case study on an entrained cold cloud, examining its morphology and key properties, as well as comparing it to the results of cloud crushing studies. In Subsection 4.3.4, we compare and contrast the differences between PIE and CIE cooling routines. Lastly, we study the structure and evolution of episodic starbursts in Subsection 4.3.5.

In order to study the effects of radiative cooling on the wind, we adopt the following fiducial parameters, taken from Schneider & Robertson (2018): $\beta = 0.6$, $\alpha = 0.9$, $M_{\text{SFR}} = 20 M_{\odot} \text{yr}^{-1}$, and disk/wind metallicity $Z = 4 Z_{\odot}$ for $Z_{\odot} = 0.02$. These values were computed from Strickland & Heckman (2009), who used Chandra X-ray observations to constrain the hot winds of M82 in terms of mass and energy loading parameters. The fiducial values correspond to a high mass, early stage starburst.

4.3.1 The Formation of Cold Gas

In this subsection, we discuss how cold gas can form in our simulation setup, as well as how it compares to the proposed origins that were discussed in Section 2.4. We start our discussion by comparing the temperature and density differences between a non-cooled wind versus a cooled wind in Fig. 4.11. As shown, the physical structure of the wind changes significantly when we include radiative effects. First, focusing our attention on the case of the non-radiatively cooled wind, we find that interactions between the wind and the disk create extensive turbulent instabilities. The wind is highly unstable, with both the free-wind and turbulent disk-wind shear layer experiencing intense fluctuations as they flow outward. These disk-wind interactions push the disk away from the starburst region and ablates and shreds it. By contrast, the inclusion of radiative cooling suppresses turbulent effects between the disk and the wind. The highly dense, metal-enriched disk cools strongly, such that most of the energy transferred from the wind to the disk is radiated away. This

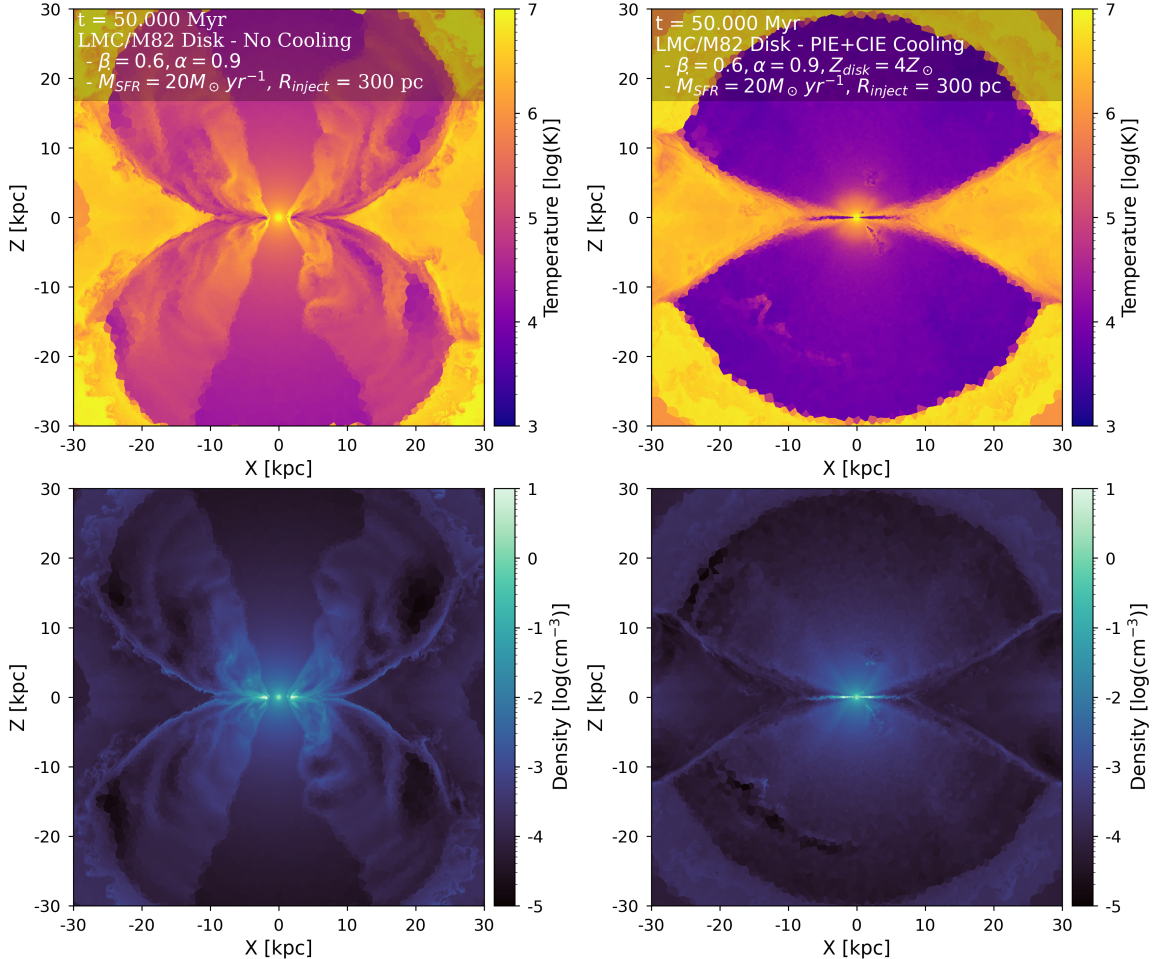


Figure 4.11. Temperature (**top row**) and number density (**bottom row**) edge-on slice plots at $t = 50$ Myr comparing the cases of a non-radiatively cooled wind (**left column**) and a PIE-cooled wind (**right column**). Under radiative cooling, both the disk and the outflow are stabilized, forming a narrow and consistent bicone structure. Efficient cooling creates dual origins of cold gas: the ejection of cold clouds and the formation of a cooling beyond a cooling radius R_{cool} .

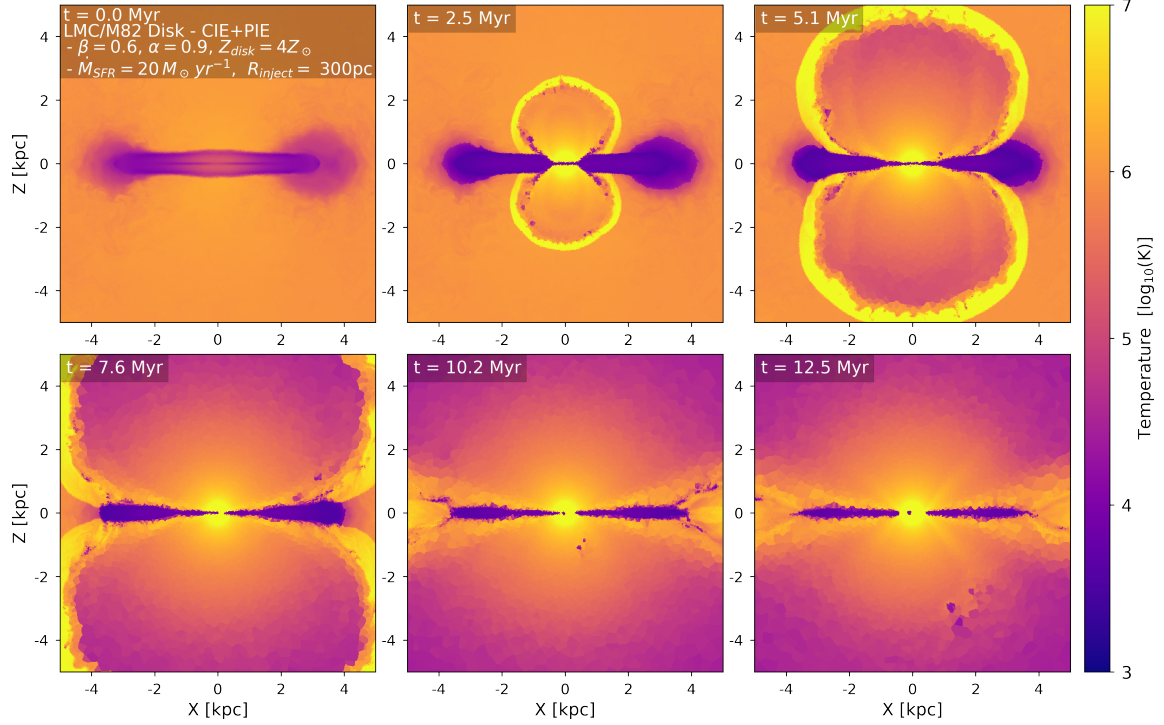


Figure 4.12. Temperature edge-on slices of the fiducial cooled wind. At the onset of the starburst, cold gas from the disk is stripped away and taken up by the hot wind. These clouds are shredded by the forward shock. By $t \sim 5$ Myr, the cooling radius R_{cool} begins to form and most of the cold gas clouds from the initial disk injection has been absorbed by the outflowing shock. By $t \sim 10$ Myr onward, much of the disk contained within R_{inject} has been destroyed by the hot gas being injected into the starburst region. Additionally, both cold gas origins become apparent.

leads to the bicone forming a narrow, consistent inner layer of free wind, surrounded by a slightly turbulent layer of somewhat denser gas. Cooling, therefore, has a stabilizing effect on the wind.

Crucial to our discussion, when radiative cooling is sufficient, two origins of cold gas emerge. The first is that of our disk, from which cold gas clouds are ejected and carried outward by the outflowing wind. The vast majority of this cold gas is ejected from the high density disk remnant that is enveloped by the starburst. The right two panels of Fig. 4.11 highlight the presence of several clouds at various radii, providing a glimpse into how they evolve at a steady state type flow. The ejected cold clouds starts out as tiny, highly dense grains of cold gas. As it flows outward, the gas expands and forms cold gas streams.

The second origin is that of the wind itself, through which cold gas can form in-situ from an initially hot phase. This is marked by a cooling radius at $R_{\text{cool}} \approx 2.7$ kpc, which stratifies the temperature into two layers:

- (i) An inner layer where $r_{\text{gas}} < R_{\text{cool}}$. In this layer, the wind consists of a hot phase which cools adiabatically until it reaches R_{cool} .
- (ii) An outer layer with $r_{\text{gas}} \gtrsim R_{\text{cool}}$ that comprises a cold phase. Here, the cooling becomes strongly radiative, leading to the gas losing significantly more heat than what would be expected under adiabatic expansion. This loss of heat results in the in-situ formation of cold gas.

The development of both the hot and cold phases, as well as the ejection of gas clouds, begins early into the starburst. As shown in the top three panels of Fig. 4.12, the initial injection of mass and energy into a relaxed disk strips away pieces of the disk in the form of cold gas clouds. By $t = 5$ Myr, the initial gas clouds have been absorbed by the much hotter shock bubble, and the cooling radius R_{cool} begins to form. The continual injection of mass and energy, as shown in the bottom three panels of Fig. 4.12, leads to a compression of the galactic disk, creating the flat disk shape seen in Fig. 4.11. Furthermore, the disk gas contained within the starburst region is enveloped and eventually shredded by the outflowing hot gas, leaving behind a dense disk remnant from which most of the cold clouds are launched. At $t = 12.5$ Myr, the cooling radius at R_{cool} becomes apparent, and we see dual origins of cold gas: ejection of clouds by the disk, and a cooling flow formed from a radiatively cooled wind at distance $r \sim R_{\text{cool}}$. Note that because of the reduced interactions between the wind and disk, winds do not form multi-layer superbubbles like in the adiabatic disk simulations. Instead, shock bubbles in radiative cooled winds consist of a forward shock of swept up CGM gas and a reverse wind shock due to cooled winds hitting the shock front.

Fig. 4.13 compares the time-averaged median radial profiles of the fiducial wind which is cooled at metallicity $Z = 4Z_{\odot}$, and non-cooled winds with the analytic results of the CC85 model. For this, we include all values that are contained within the 120° bicone described in Fig. 4.8. Time averages are taken in order to smooth out potential fluctuations in the wind profiles that might have formed due to cooling e.g. large cold cloud streams. The shaded regions represent the values between the 16th and 84th percentiles, or $\pm\sigma$. Comparing the fiducial cooled wind to the non-cooled wind profiles, we further verify the stability of the cooled wind. The damping of turbulence results in decreased variation within the wind properties, such that the median radial profile is an accurate indicator of the outflow behavior across the 120° bicone. The density and radial velocity profiles of the cooled wind both follow a similar evolution to those of a gravity corrected CC85-like wind. The temperature profile of the fiducial wind can be separated into three phases:

- (i) An adiabatic hot phase that roughly spans $0 - 1.5$ kpc that approximately follows the CC85 solution.
- (ii) An intermediate "warm" phase between $\sim 1.5 - 3$ kpc, where the temperature starts to deviate from CC85.
- (iii) A cold phase beyond $r \gtrsim 3$ kpc, which is dominated by radiative cooling. During the cold phase, the gas drops significantly, eventually plateauing at a temperature of $T \approx 10^4$ K.

The intermediate phase indicates an "interface" region in which both adiabatic expansion and radiative cooling play significant roles in controlling the thermal structure of the wind. As expected from a function of both temperature and density, the pressure also experiences a sharper drop than the expected profile of CC85. However, as reduction in instabilities creates a highly stable density profile that corresponds closely to CC85 predictions, the pressure difference only becomes significant during the cold phase, where its radial profile becomes roughly 1 order of magnitude less than the hot gas of the CC85 model.

We also included radial profiles where we decreased the metallicity to $Z = Z_{\odot}$ and $Z = 0.25Z_{\odot}$. Generally, while the suppression of turbulence and the formation of the central disk fragment occur even in low metallicity winds, the presence of a clear cooling flow and the ejection of clouds is only seen at super-solar metallicities. Setting the metallicity to $Z = Z_{\odot}$ only produces a small and gradual decrease in the wind temperature, indicating that radiative cooling only occurs at large distances for

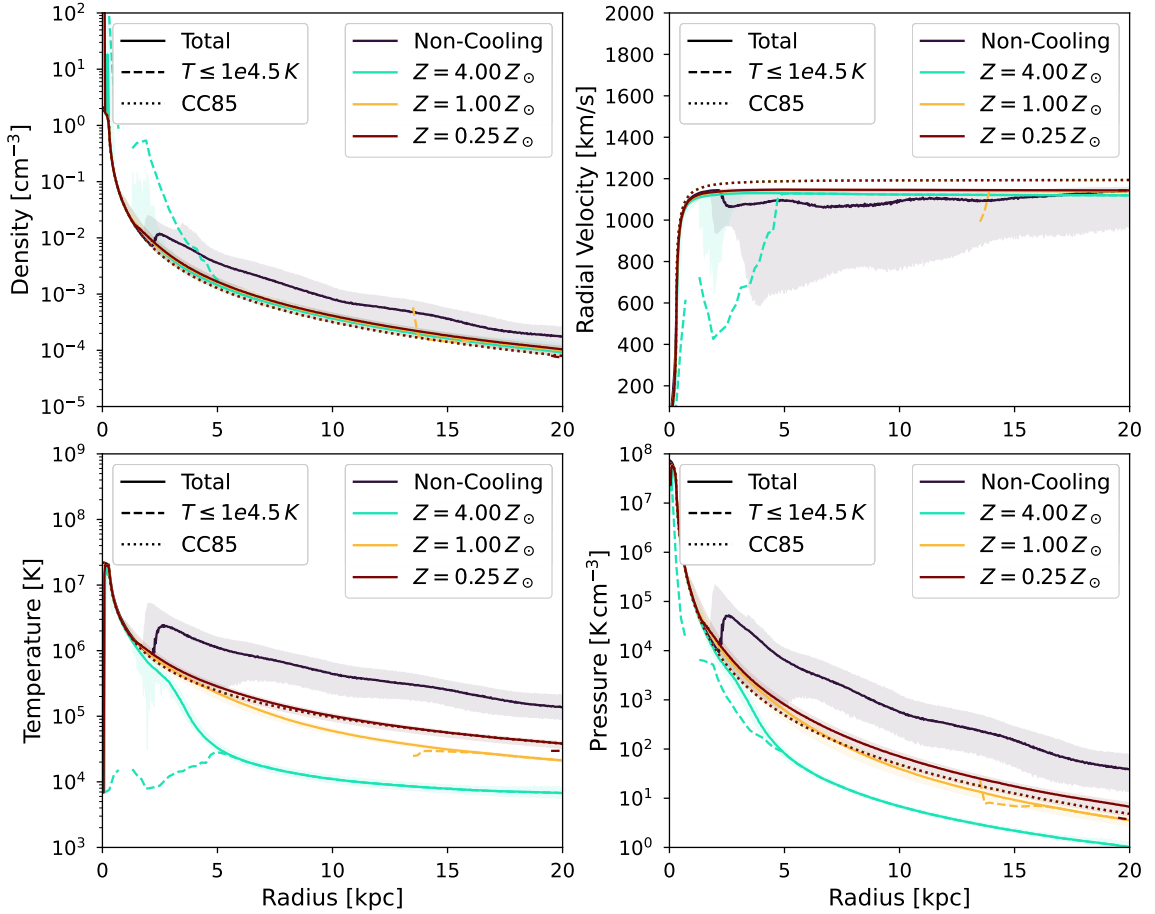


Figure 4.13. Time-averaged (over 2 Myr) median radial profiles of density (**upper left**), radial velocity (**upper right**), and temperature (**lower left**), and pressure (**lower right**) where metallicities are varied under fiducial loading parameters. Dashed lines represent the profile of cold gas below $T \lesssim 10^{4.5} \text{ K}$, while dotted black lines represent the CC85 predictions. Shaded regions represent the variance in each quantity. As cooling stabilizes the outflow, the variation in wind properties is reduced, such that the median density and velocity profiles correspond to a gravity-corrected CC85 wind. The temperature profile initial follows the CC85 result, but starts to deviate as radiative cooling becomes significant. The pressure, as a function of both density and temperature, only starts to undergo significant deviations as radiative cooling starts to dominate over adiabatic expansion. The production of cold gas only becomes noticeable under a high metallicity, when a strong cooling flow forms beyond R_{cool} .

solar metallicities. A possible reason for this could be due to the implementation of metallicity as a passive scalar field, despite it having an obvious effect on the cooling. It is possible that the effects of gas metallicity were not fully represented in our suite, leading to a super-solar metallicity being required for efficient cooling.

Comparing the formation of multiphase gas in our simulation to their predicted origins in Section 2.4, we find that the entrainment origin for cold clouds corresponds strongly with our results. Clouds are clearly ejected outward by the starburst. Moreover, their evolution from small grains to streams as they flow outward is indicative of entrainment, where clouds are elongated, sheared, and mixed by the wind as they flow outward. However, our results compare less favorably with the two-stage stage transmigration model for in-situ structure formation by [Thompson et al. \(2016\)](#). Broadly speaking, the results do corroborate much of the physical picture, demonstrating a two stage production of cold gas where gas clouds are ejected from the disk by the outflowing wind, followed by the formation of a cooling flow beyond the cooling radius R_{cool} . However, our results also demonstrate key behavioral differences. Most notably, as Fig. 4.12 demonstrates, cold gas clouds are only shredded within the first 5 Myr when they merge with the significantly hotter and more massive forward shock. It is unlikely that these shredded cold gas clouds play a role in seeding density perturbations inside the wind, as beyond the R_{cool} , the wind pattern predominantly consists of a coherent phase of cold gas instead of the cooling and condensation expected for a second transmigration. At later times, while the winds of the hot phase do have ablative effects on the cloud, these clouds manage to survive and propagate outward. Based on this, we argue that under idealized circumstances, cold clouds are more likely to originate from entrained cold clouds rather than in-situ cooling. We posit that cold structures can form from an initially hot phase if the wind contains additional material that can seed instabilities. Such material could come in the form of dust grains, which can catalyze cold phase formation ([Veilleux et al. 2020](#)). Alternatively, additional physics such as self-gravity could introduce density perturbations and drive in-situ formation of cold clouds.

Given the similar setup and the same controlling parameters, the results of our fiducial simulation strongly resemble the high mass-load state of the radiatively cooled central feedback simulation of the CGOLS suite, referred to as Model B by [Schneider et al. \(2018\)](#). Like us, cooling in Model B also results in the suppression of turbulence and shear instabilities, causing the wind to form a stable structure with a clearly defined cooling radius. However, unlike our fiducial cooling results, Model B does not result in the production and ejection of multiphase gas clouds. We compare our respective temperature profiles in Fig. 4.14. Notably, despite having a similar cooling radius of $R_{\text{cool,CGOLS}} \approx 2.77 \text{ kpc}$, the temperature gradient of Model B is much steeper than that of our fiducial simulation, with temperatures falling to a floor value of 10^4 K by $r \sim 3 \text{ kpc}$. One possible explanation for this is the difference in cooling models. Cooling physics, as described in [Schneider & Robertson \(2018\)](#), was implemented via an analytic function that has been parabolically fitted to a CIE cooling curve computed from Cloudy at solar metallicity. As such, the cooling routine of the CGOLs suite is purely a function of temperature. In contrast, our simulation uses a PIE-based routine, which is less effective at cooling low density gas. This results in a smoother temperature gradient compared to CGOLs.

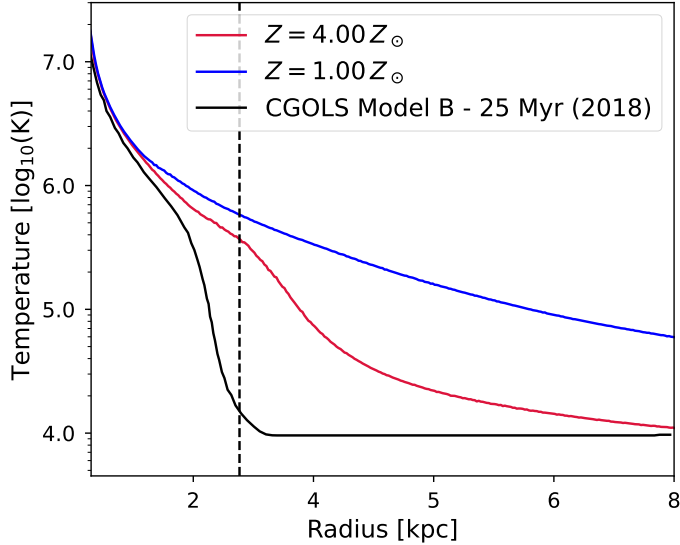


Figure 4.14. Temperature profiles for radiatively cooled winds at solar and solar metallicities compared to the digitized temperature profile of the high-mass load state of the solar metallicity, radiative central feedback simulation (CGOLS Model B) described in Schneider et al. (2018). The dashed line represents their cooling radius at solar metallicity. The temperature gradient of the Model B is significantly steeper than even our super-solar metallicity wind, reaching a temperature floor of 10^4 K by ~ 3 kpc. We argue that this discrepancy in results could be caused by differences in cooling models.

4.3.2 Effects of Energy and Mass Load on Radiatively Cooled Winds

As established in Section 2.4, the mass load β and the energy load α can have substantial impacts on the wind cooling by altering the cooling and advection times. In this subsection, we examine how these two parameters can affect cooling efficiencies, as well as how they can affect the flow of radiatively cooled winds. To do this, we compare four different energy-mass load configurations, which are listed in Table 4.3, along with their designation and abbreviated form in writing.

Name (abbreviation)	Configuration
Fid./Low Energy, Low Mass (LE-LM)	$\alpha = 0.9, \beta = 0.6$
High Energy, Low Mass (HE-LM)	$\alpha = 1.8, \beta = 0.6$
Low Energy, High Mass (LE-HM)	$\alpha = 0.9, \beta = 1.0$
High Energy, High Mass (HE-HM)	$\alpha = 1.8, \beta = 1.0$

Table 4.3. Table listing the energy-mass load configurations varied in Subsection 4.3.2. The left column lists the name of for each simulation, along with the abbreviation we use to refer to them. The right column lists the parameters used in each configuration.

We analyze the temperature, density, and velocity, focusing on a specific case study for each intensive property. We provide a discussion on how each property is affected by the change in loading parameters, as well as a deeper dive into possible insights that we can ascertain from each property. We then conclude by discussing the outflow rates.

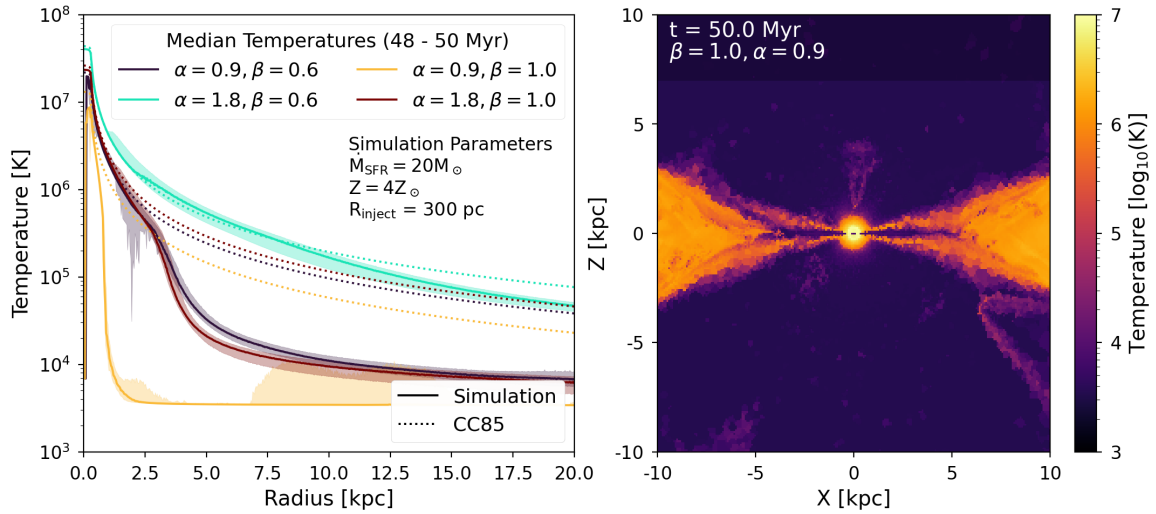


Figure 4.15. Time-averaged median temperature profiles of each load configuration (left) and edge-on temperature slice (right) of the LE-HM configuration. Shaded regions represent the temperature variation. A high mass load β increases the cooling efficiency and retracts R_{cool} , while a high energy load α decreases cooling efficiency and extends R_{cool} . Cooling is more dependent on β than α , as the HE-HM configuration cools more efficiently than the fiducial LE-LM case despite a smaller increase in β compared to α . However, only the LE configurations lead to cold cloud formation. Increased cooling efficiency reduces the mixing strength, with LE-HM clouds going through a more extended mixing process than those in LE-LM. The decreased mixing in LE-HM results in smaller, more shredded clouds seeding the wind with warmer gaseous debris.

Temperature

We begin by analyzing Fig. 4.15, which consists of the radial temperature profiles on the left panel, and the edge-on slice of the LE-HM case ($\alpha = 0.9, \beta = 1.0$). From the radial profiles, we can see that in all configurations, the gas will eventually cool faster than what would be expected from an adiabatic wind one it has reached a far enough distance from the starburst. The LE-HM case has the most intense cooling out of the four, having the smallest cooling radius, as well as the steepest temperature gradient, with median temperatures falling to the temperature floor of $T = 10^{3.5} \text{ K}$ past R_{cool} . Comparatively, the HE-LM case ($\alpha = 1.8, \beta = 0.6$) cools weakly, with radiative effects only becoming significant at distances $r \gtrsim 10 \text{ kpc}$. Notably, we find that cold clouds only form in the fiducial LE-LM case ($\alpha = 0.9, \beta = 0.6$) and the LE-HM case. The mixing processes of larger clouds can be approximated by the shaded regions of their respective temperature profiles. Clouds traveling through the LE-HM wind experience a prolonged mixing process, which can stretch across kiloparsecs as they flow away from the starburst. Comparatively, the LE-LM winds have a relatively short mixing process that is only significant at 2-3 kpc, with the temperature contrast between wind and cloud disappearing past the cooling radius. From this, we infer that more efficient cooling weakens the mixing processes, allowing clouds to remain coherent at larger distances. When we examine the LE-HM slice, we find that larger clouds form "envelopes" of hotter gas as they are mixed with the wind. Additionally, we find because of the reduced mixing, smaller and more shredded clouds seed the wind with warmer gaseous debris with temperatures $T \sim 10^4 \text{ K}$.

Using the temperature profiles to examine how the loading parameters affect the cooling efficiency, we find that the mass load factor β increases the cooling efficiency and heavily retracts the

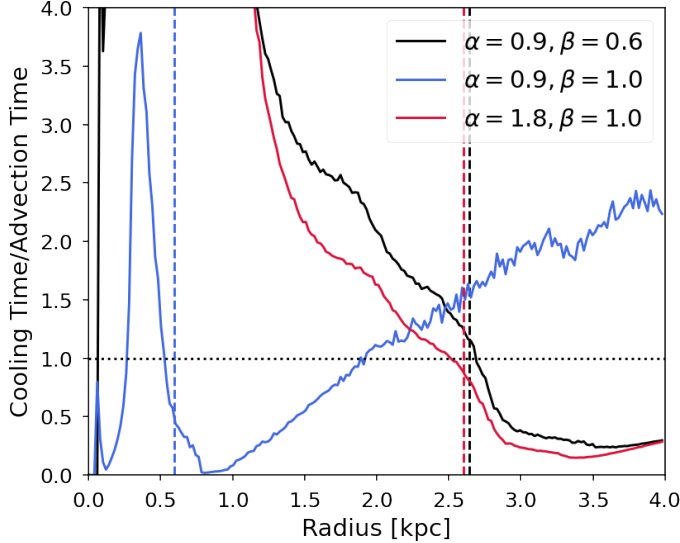


Figure 4.16. Ratio of cooling time to advection time $t_{\text{cool}}/t_{\text{advec}}$, with the distance at $t_{\text{cool}}/t_{\text{advec}} = 1$ being the cooling radius R_{cool} . Dashed vertical lines represent the predicted cooling radii from Equation 2.24. The cooling radii of each configuration roughly corresponds with their predicted cooling radii. The decline in both temperature and densities decreases the cooling efficiency, leading to $t_{\text{cool}}/t_{\text{advec}} > 1$.

cooling radius, with HM-LE and HM-HE having the smallest cooling radii and steepest temperature gradients. By contrast, increasing the energy load α extends the cooling radius and decreases the cooling efficiency. Notably, we find that HM-HE wind, which has its mass loading factor from 0.6 to 1.0 or $\Delta\beta = 0.4$, has a slightly shorter cooling radius and steeper temperature gradient than the fiducial wind, despite a higher increase in the energy load from 0.9 to 1.8 or $\Delta\alpha = 0.9$. In other words, β has a stronger impact on the cooling efficiency than α . Nevertheless, though cooling is less dependent on the energy load factor α , it still plays a fundamental role in driving the formation of cold clouds. This is seen when examining the temperature profiles of the HE-LM ($\alpha = 1.8, \beta = 0.6$) and HE-HM ($\alpha = 1.8, \beta = 1.0$) simulations. In both cases, we find that over a sustained starburst, cold cloud formation and ejection from the disk does not occur on noticeable scales. Additionally, when examining their temperature evolution (see [link](#)), we find that the disk gas contained within their starburst regions are completely shredded over time, with the HE-HM wind having a shorter destruction timescale between the two configurations. It is likely that any cold clouds that might have formed before the disk is destroyed are similarly shredded and mixed with the hot injected gas.

The stronger dependencies of cooling on mass load β than energy load α correspond well with the predicted results of the [Thompson et al. \(2016\)](#) model for in-situ formation of cold gas, where the cooling radius' dependencies on the loading factors are $R_{\text{cool}} \propto \alpha^{2.13}\beta^{-2.92}$ (see Equation 2.24). To make further verifications, we plot the ratio between the cooling time to advection time $t_{\text{cool}}/t_{\text{advec}}$ as a function of radii in Fig. 4.16, with $t_{\text{cool}}/t_{\text{advec}} = 1$ being the cooling radius where the cooling physics becomes radiative. Note that we exclude the HE-LM wind, as the weak cooling of that configuration means that we don't expect to see a cooling radius at small distances. We find that for all cases, the cooling time falls below the advection time at distances roughly corresponding to the predicted cooling radii of Equation 2.24. At larger distances, we find that as gas gets colder and

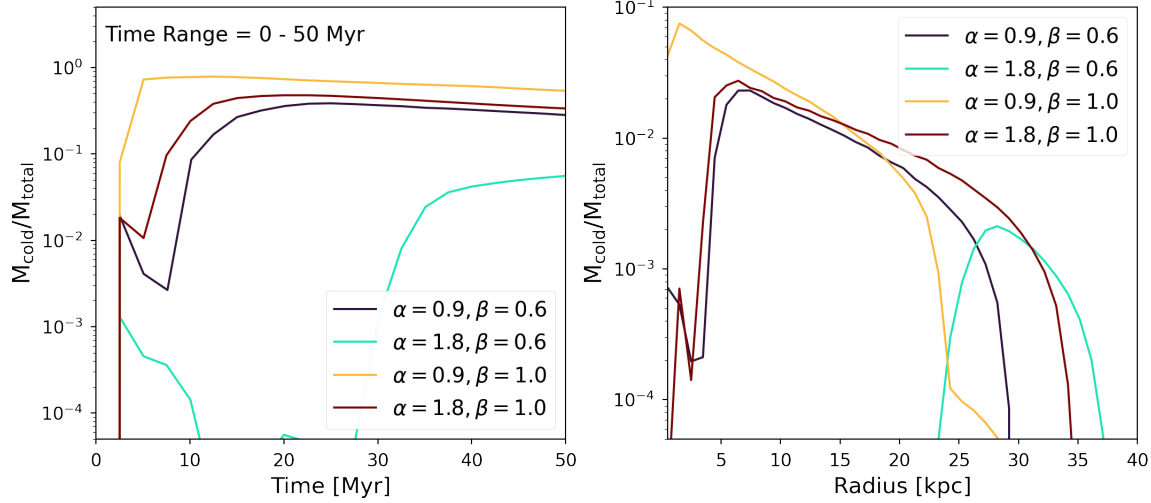


Figure 4.17. Cold gas mass fraction over time (**left**) and radius (**right**) for varying load configurations. The total fraction of cold gas mass initially declines due to the shredding of cold clouds by the shock front. This is followed by a peak, followed by a marginal decline over time due to the growing shock bubble. Higher β leads to a higher fraction of cold gas, while higher α leads to a lower fraction, consistent with their expected effects on the cooling efficiency. For mass fraction over radii, we find cold gas fractions are highest near their configuration’s R_{cool} and decreases over distance. HE winds ($\alpha = 1.8$) are faster and can transport cold gas to larger distances. LE winds ($\alpha = 0.9$) are slower and transport gas to shorter distances. Clouds comprise a small percentage of the total cold gas mass compared to the cold phase, and are not noticeable across large time averages.

less dense, the cooling rates decline, and cooling becomes less efficient. As a result, t_{cool} once again becomes larger than advection time t_{advec} .

In Fig. 4.17, we investigate the total fraction of cold gas with $T \leq 10^{4.5}$ K contained within the wind, examining all cells within the 120° wind bicone. The left panel shows the total fraction over time. The right panel shows the median fraction over radius, time-averaged over 50 Myr. First, focusing on the temporal profiles, we find that the cold gas mass fraction experiences an initial decline, which we attribute to the shredding of cold clouds as they impact the shock front. Over time, the fraction of cold gas rises again as the cooling phase develops, with all but the HE-LM wind reaching a cold mass fraction of $M_{\text{cold}}/M_{\text{total}} > 0.1$. The cold gas fraction increases with higher β and decreases with higher α , which is consistent with their respective effects on cooling efficiency. The cold gas fractions peak, and then marginally decline over time. We argue that this is due to the forward and reverse shocks, which grows more massive over time. Analyzing the radial profile, we can see that most of the cold gas is close to their respective R_{cool} , and decreases over distance. As the cold gas takes longer to reach these longer distances, we consequentially don’t see much cold gas at large distances until later times. Faster, i.e. HE, winds have larger bicones and thus transport cold gas to larger distances, while LE winds are slower, and thus the range over which they transport cold gas is smaller. As clouds form a small percentage of the total cold gas mass compared to the cold phase, we do not expect them to make significant contributions to the cold gas fraction across long periods.

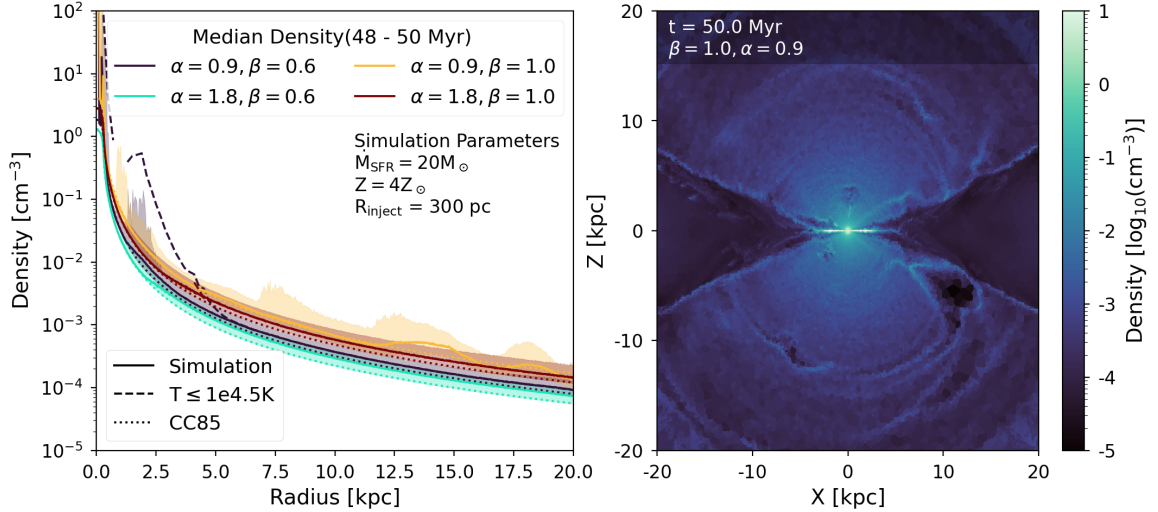


Figure 4.18. Time-averaged median density profiles (**left**) of each load configuration and edge-on density slice (**right**) of the LE-HM configuration. Dashed lines represent the cold gas temperatures and shaded regions represent the density variation. The HE-LM wind has a minor deviation from CC85 predictions, indicating slightly stronger disk-wind interactions. For LE winds, the cloud densities are initially $\sim 10^3$ times higher than the wind. Clouds expand as they propagate outward, eventually converging onto the background densities. Low density regions in front of the cold clouds imply a transfer of mass from the wind to the cloud, allowing the cloud to survive at large distances. For LE-HM winds, clouds expand enough to form large arcs that comprise the ripples seen in their variation.

Density

In Fig. 4.18, we show the median number density profiles of each load configuration, along with the density slice of the LE-HM wind. We find that of the four cases, the HE-LM wind deviates the most from the analytic predictions of CC85. We attribute this to its relatively weak cooling efficiency, which results in a more pronounced turbulent interface. However, we note that the differences are minor, as in all cases the high densities of the disk cause a reduction in disk-wind interactions.

For winds that form cold clouds i.e. LE-LM and LE-HM winds, we find that cloud densities are initially a factor of $\sim 10^3$ greater than the wind densities. As clouds propagate outward, they expand, and their densities start to converge onto the background wind densities. However, as seen in the density slice of the LE-HM wind, the highly efficient cooling allows for clouds to continue to expand even after crossing R_{cool} . At large distances, these clouds expand enough to form arcs that take up much of the wind flow, which are represented as ripple patterns in the shaded regions of their density profile. Comparatively, the density evolution of the LE-LM wind is subdued. Although LE-LM clouds continue to survive and expand at large distances, they do not form the same large-scale ripple patterns seen in the profiles, and they mostly fade into the wind flow.

We plot phase diagrams to examine the relationship between temperature and density, showing the case of the LE-LM wind in Fig. 4.19. Here, we examine all wind cells contained within a bicone of 120° , weighing the temperature and density bins by the total mass.

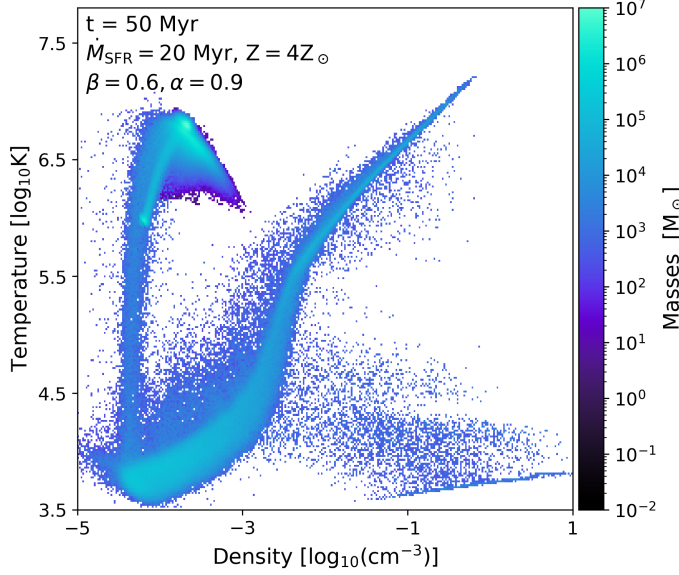


Figure 4.19. Phase diagram of temperature as a function of density, weighted by the mass. The wind can be separated into three phases: (i) the forward shock bubble phase at $T \sim 10^{6.5}$ K (ii) the wind phase, which starts out as a hot adiabatic wind at 10^7 K, expands, and becomes radiative at $n \sim 10^{-2} \text{ cm}^{-3}$, and (iii) the high density, low temperature phase of the cold clouds. Two transitions are noted: (i) the convergence of the cold clouds into the wind, and (ii) the reverse wind shock at the edge of the bicone.

We find that the overall distribution can be separated into three phases:

- (i) The forward shock bubble phase, which consists of CGM gas that is swept up by the wind, defined by $\Delta T \approx 10^6 - 10^7$ K and $\Delta n \approx 10^{-5} - 10^{-3} \text{ cm}^{-3}$.
- (ii) The wind phase, which consists of an initially hot adiabatic gas at 10^7 K which expands as it cools. The curved decline at $n = 10^{-2} \text{ cm}^{-2}$ corresponds to the shift to radiative cooling.
- (iii) The high density, low temperature phase characterizing the cold gas clouds.

We note that phase (iii) is only apparent for LE winds, and for the LE-HM wind, it is heavily mixed with the wind phase due to the strong cooling of LE-HM. We identify two major phase transitions. The first is the previously discussed convergence of cloud densities with those of the wind. The second phase transition is the formation of the reverse wind shock upon interacting with the forward shock. Due to shock heating, the cold wind compress and become denser.

Velocity

The median velocity profiles for the LE configurations, along with the velocity edge-on slice of the LE-LM wind, are shown in Fig. 4.20. For this plot, we neglect the profiles of the HE winds, as they do not produce cold clouds. Moreover, their velocity profiles are dynamically similar to the LE-LM configuration. Examining the LE-LM velocity slice, we see that the cooling-driven reduction of hydrodynamic instabilities and turbulence from disk-wind interactions results in a highly stable and consistent velocity profile across the entire bicone. The velocities of the LE-LM winds are fast enough that it is less affected by gravity, and the lack of expansive cold clouds allows it to maintain a stable velocity profile that corresponds well with the CC85 predictions. By contrast, the velocity

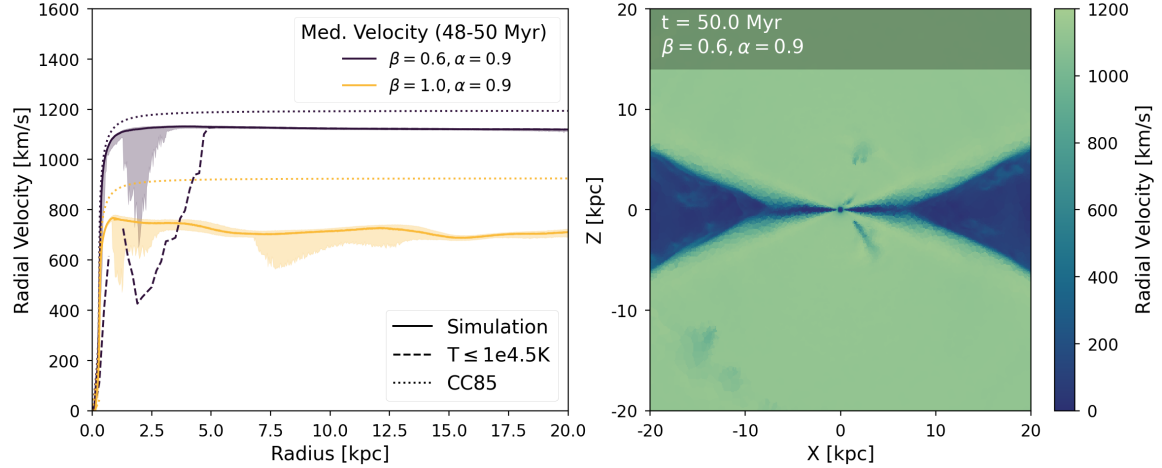


Figure 4.20. Velocity profiles (left) of the LE configurations, along with the edge-on velocity slice (right) of the LE-LM case. Dashed lines represent the cold gas velocities, and shaded regions represent the velocity variance. The LM velocity profile is highly stable due to reductions in hydrodynamic instabilities. The HM velocity profile is 200 km/s lower than the CC85 prediction due to its lower steady state velocity. Additionally, the more wave-like velocity profile is caused by the expanded cold clouds, which have reductive effects on the profile. We find that as clouds flow outward, they become entrained, accelerating to speeds comparable to the background wind.

profile of the LE-HM wind is unstable, and plateaus at a velocity that is ~ 200 km/s lower than the analytic prediction. We attribute the deviation from CC85 to the LE-HM wind having a slower steady state velocity, which causes it to be more affected by gravitational corrections. Additionally, we argue that the unstable profile is due to the highly expanded clouds, which are slower and can cause the velocity profile to fluctuate.

Looking at the velocities of the cold clouds in Fig. 4.20, it is clear from the profiles and slice plots that cold clouds at small distances have low initial velocities relative to the wind. However, as they flow out of the starburst region, the clouds accelerate, eventually becoming co-moving with the wind and surviving at distances several kpc from the starburst. That is to say, we verify that we see an entrainment of cold gas clouds by the hot phase, where rather than being fully shredded by the wind's hydrodynamic instabilities, clouds are instead accelerated by the wind. The cloud entrainment appears to take the form of a head to tail pattern, where the region of the cloud closest to the starburst region appears to have lower velocities than the region facing the wind. Notably, at large distances, we find that the clouds have not fully faded, suggesting a survival mechanism that allows the cloud to be sustained at large distances.

Outflow Rate

To compute the outflow rates, we use the approach described in Nelson et al. (2019) and consider the outflow rates to be instantaneous fluxes of all gas cells in a thin shell. The mass outflow rate \dot{M} is given as:

$$\dot{M} = \frac{\partial M}{\partial t} = \frac{1}{\Delta r} \sum_{i=0}^N \left(\frac{\mathbf{v}_i \cdot \mathbf{r}_i}{|\mathbf{r}_i|} m_i \right) \quad (4.5)$$

for a given cell i with velocity \mathbf{v}_i , position relative to the central starburst center \mathbf{r}_i , and mass $m = m_i$. The cell is contained within a bicone shell binned by $\Delta r = 100$ pc.

A similar process is used to calculate the energy and momentum outflow rates. The energy outflow rate \dot{E} is given as:

$$\dot{E} = \frac{1}{\Delta r} \sum_{i=0}^N \left(\frac{\mathbf{v}_i \cdot \mathbf{r}_i}{|\mathbf{r}_i|} E_i \right) \quad (4.6)$$

where the cell energy E_i consists of the internal (thermal) and kinetic energy, such that $E_i = m_i \cdot (\frac{1}{2}v_i^2 + e_{th})$. The momentum outflow rate \dot{P} is:

$$\dot{P} = \frac{1}{\Delta r} \sum_{i=0}^N \left(\frac{\mathbf{v}_i \cdot \mathbf{r}_i}{|\mathbf{r}_i|} p_i \right) \quad (4.7)$$

for a cell momentum of $p_i = m_i v_i$.

We show the median outflow rates for each parameter configuration, time-averaged over 48-50 Myr, in Fig. 4.21. As seen from the mass and momentum outflow rates (left column) of Fig. 4.21, the overall pattern between the \dot{M} and \dot{P} profiles is that gas contained in the starburst region is initially accelerated outward as hot gas, reaching an approximately asymptotic outflow rate at steady state. After the gas reaches the cooling radius, the entire outflow undergoes rapid cooling, forming a cold gas phase that comprises nearly all the wind, similar to what is shown in Fig. 4.15. We find that the HM winds ($\beta = 1.0$) have a higher mass outflow rate than LM winds ($\beta = 0.6$). However, a conspicuous complication to this finding is that much of the LE-HM wind is encompassed by the clouds. Collectively, they leave behind spikes of higher mass outflow rate \dot{M} , followed by a drop in \dot{M} which are lower than that of the background wind. From the LE-HM density profile of Fig. 4.18, we can infer that the spike-drop shape in \dot{M} characterizes the head-tail pattern of the cloud. Furthermore, the mass outflow rate of the head increases as the cloud travels outward. Combined with the lower mass outflow rates of the tail, this raises the possibility of a local inflow effect that imparts mass from the tail to the rest of the head. Given the small cooling radius of the LE-HM wind, the increased outflow rates could be the result of a cooling flow that imparts mass into the cloud (Dutta et al. 2022). This suggests the possibility that the cooling flow provides a mechanism for long-term cold cloud survival, allowing multiphase gas to survive and be detected at large distances (Schneider et al. 2018).

Looking at the momentum outflow rates \dot{P} , we note that the HE winds have significantly higher \dot{P} than their LE counterparts, with the HE-HM wind rate being nearly double that of the fiducial LE-LM wind. Returning to the topic of the lack of the production of cold clouds in HE outflows, we theorize that the increase in momentum also significantly increases the imparting of shear instabilities. The increased shearing shreds any clouds that might form before they can be accelerated out of the disk, before also destroying the parts of the disk contained in R_{inj} , explaining why we don't see any clouds from these simulations. The momentum outflow rate of the HE-HM wind being higher than the HE-LM wind could also explain why it is faster at shredding away the disk.

A key question to consider is whether a radiatively cooled wind remains energy-driven, or if it becomes momentum-driven. Intuitively, for an energy-driven wind, we would expect to see a drop in the energy outflow rate as the gas cools. However, when looking at the energy outflow rate \dot{E} (upper right), we note that outside R_{inject} , the wind contained in the bicone region instead maintains a stable energy outflow rate as it propagates away from the disk. Furthermore, while the initial acceleration of wind from R_{inject} is clearly thermally (i.e. internal energy) driven, the contributions from the internal energy decline significantly beyond R_{inject} , such that past the cooling radii, the kinetic contribution becomes the dominant factor. This suggests that the cold gas might be momentum-driven rather than energy-driven.

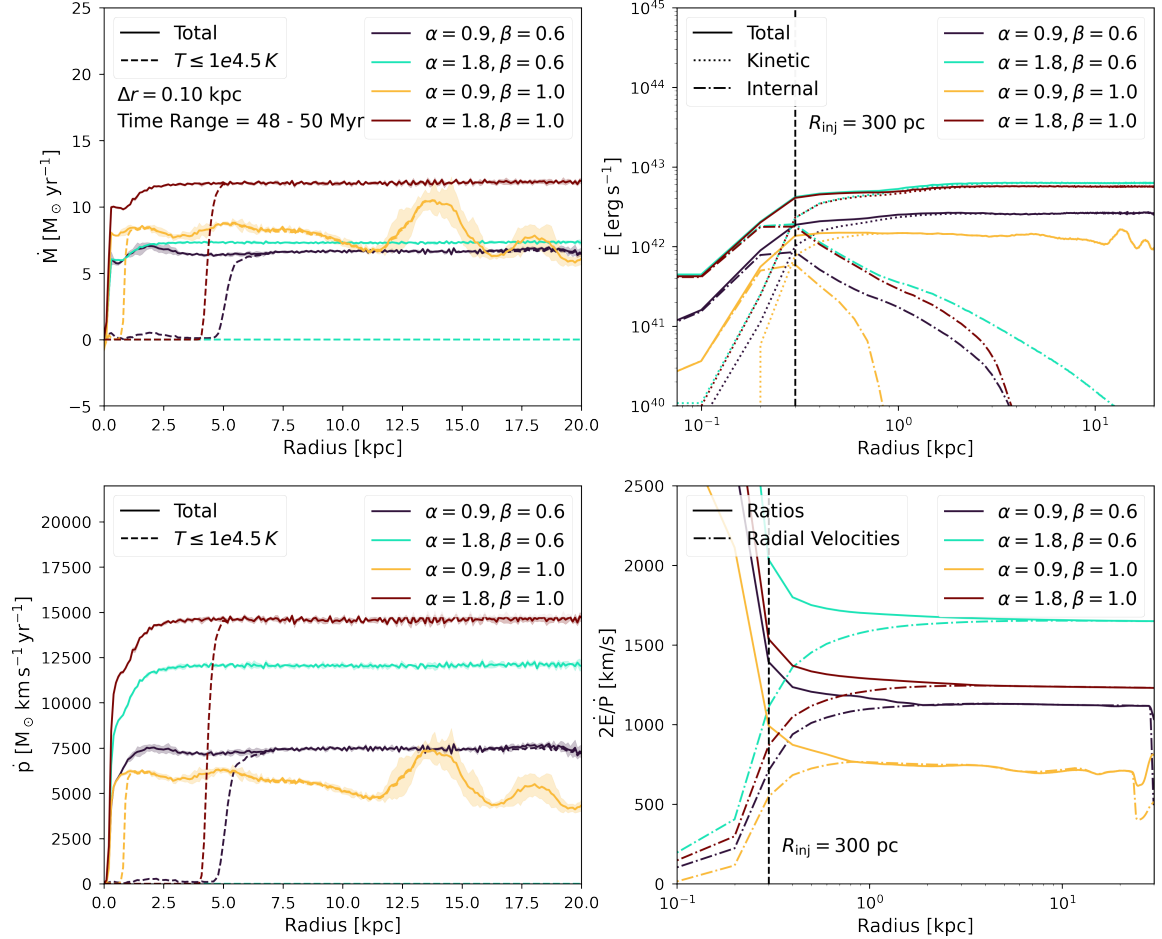


Figure 4.21. The mass (**top left**), energy (**top right**), momentum outflow (**bottom left**), and the energy to momentum outflow rate ratio (**bottom right**) for varying load configurations. For each configuration, the mass outflow rate \dot{M} and momentum outflow rate \dot{P} initially comprises an entirely hot phase, before transition to an entirely cold phase past their respective cooling radius R_{cool} . HM winds have higher \dot{M} than LM winds. Due to the presence of clouds, the LE-HM contains spikes in \dot{M} followed by a drop to a value below the wind values, suggesting a local inflow effect that imparts mass to the cloud. HE winds have higher momentum outflow rates than LE winds. The higher momentum outflow rates could increase shearing, shredding any cold clouds that before it can leave the disk. Winds accelerated from the starburst are initially energy driven, but transitions being momentum-driven past R_{cool} . This indicates that momentum is the primary driver of the cold phases.

To test this, we make an estimation that the total wind energy is purely kinetic, neglecting the thermal energy component:

$$E_{\text{tot}} \approx 1/2mv^2 \rightarrow mv^2 \approx 2E_{\text{tot}} \quad (4.8)$$

Under this assumption, the energy outflow rate \dot{E} becomes proportional to:

$$\dot{E} = \frac{1}{\Delta r} \sum_{i=0}^N v_{r,i} E_i \propto 1/2mv^3 \rightarrow 2\dot{E} \propto mv^3 \quad (4.9)$$

We plot the ratio of $2\dot{E}$ to \dot{P} (bottom right panel). Additionally, we include the radial velocities for each configuration, arguing that for an energy-driven wind, $2\dot{E}/\dot{P}$ should be significantly higher than that of the radial velocities, while for momentum-driven wind, this ratio should converge with the radial velocities. We find this approximation fails for $r \lesssim R_{\text{cool}}$, as expected for energy-driven winds. However, for $r > R_{\text{cool}}$, the extensive cooling of the gas leads to this that this ratio converges onto the radial velocities, demonstrating that the momentum becomes the driver of the cold phase in wind flows. As such, we arrive at a two-stage picture, where winds are first thermally driven out of the injection radius. Radiative cooling reduces the thermal contribution, causing the cold phase of the wind to transition to becoming momentum driven after they cross R_{cool} .

4.3.3 Survival and Entrainment of Cold Clouds

In Subsection 4.3.2, we've established that under efficient radiative cooling, cold clouds within the suite are entrained and can survive up to distances that are several kpc away from the central starburst. In this subsection, we build up on this and investigate the properties of entrained clouds in greater detail. For this purpose, we conduct a case study on a cloud that is taken from our fiducial wind simulation and has a center of mass at (in kpc): $r_x = 1.22, r_y = 1.42, r_z = 1.68$. We examine the column densities of the cloud, focusing on the overall cloud structure and how it evolves from head to tail. Afterwards, we look at the temperature, velocity, and pressures of the cloud, comparing its properties to the proposed results in Sections 2.2 and 2.4.

The projection and radial profiles of the cloud's column densities along the y-axis are presented in Fig. 4.22. From the projection, we see that this cloud has developed a stream-like morphology, consisting of a highly concentrated "head" that faces the central starburst. The cloud is densest in the central region, which is denser than the outer edge by a factor of 10. Shearing effects between the cold, slow cloud and the much hotter, faster wind background creates a wind-facing cometary tail. Notably, the cloud undergoes a broadened, differential expansion, being highly compressed and narrow at the head and widening as the cometary tail flows outward. The column densities of the tail decline as it gets further away from the head, eventually merging with the column densities of the wind background.

We show the center edge-on temperature slice of the cloud in the right panel of Fig. 4.23. We find that the cloud is surrounded by a layer of hot wind with temperatures at around $T \sim 10^6 - 10^7$ K, with the hottest temperatures being located near the cloud head. This is indicative of a wind-driven shock that sweeps through and crushes the cold cloud. We see that at the cometary tail, shearing from the wind results in warm mixed gas that act as the boundary layer between the cloud and the wind. In the left panel of Fig. 4.23, we show the median temperature profiles of both the cloud and the mixed gas. In order to isolate the cloud and the boundary layer from the rest of the wind, we narrow our region of focus to an angular range of $40 - 60^\circ$ from the z-axis. To identify cloud cells, we set a threshold filter where we assume all cloud cells have a temperature of $T_{\text{cell}} \leq 10^{4.5}$ K

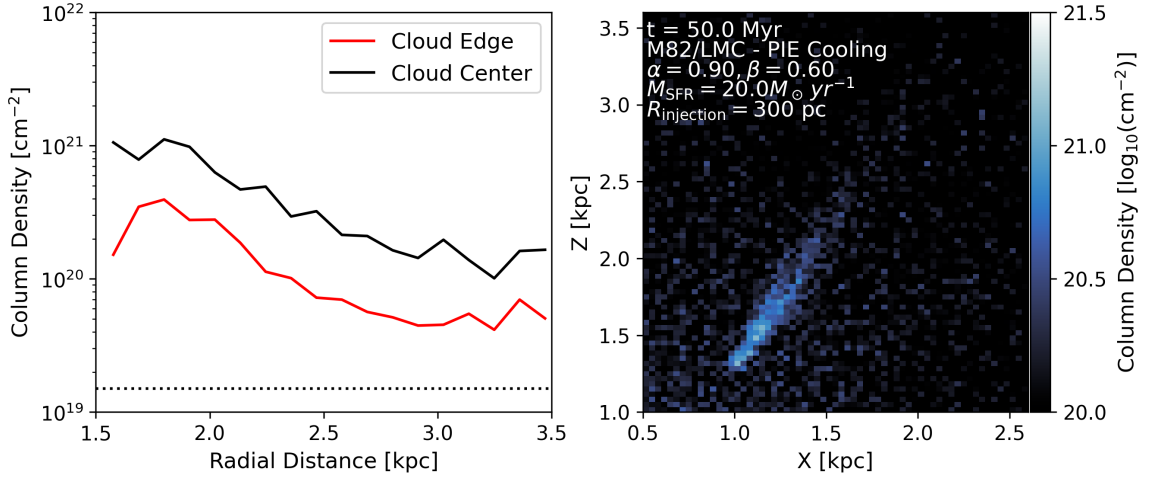


Figure 4.22. Column density profiles (**left**) and projections (**right**) of a cold gas cloud. For the profiles, we approximate the cloud center (black) to be the maximum value across each bin, and the median to be the outer edges of the cloud (red). The cloud develops a cometary flow, with the highest column densities at the head and decreasing at the tail to the extent where it fades into the background wind. The central densities are higher than the edge by roughly a factor of 10. Both center and edge temperatures are above $N_{\text{cl,grow}} \approx 1.5 \cdot 10^{-19} \text{ cm}^2$ (dotted line) for the given parameters. However, the column densities fade, deviating from cloud crushing studies.

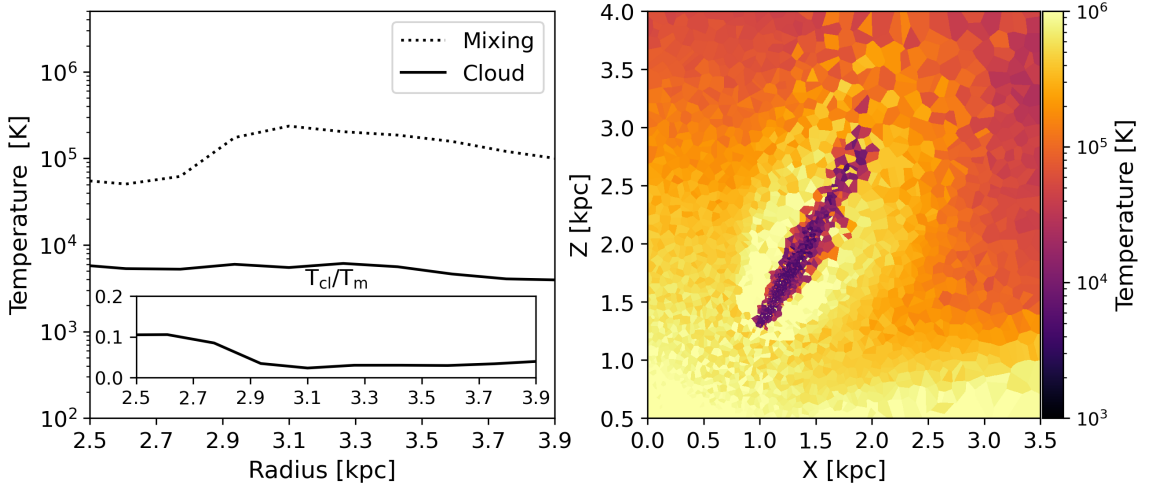


Figure 4.23. Temperature slice of the entrained cloud (**right**), along with the radial temperature profiles (**left**) of the cloud (solid) and the mixed intermediate boundary (dotted). The inset plot is the ratio of the cloud temperature to mixing temperature across radii. The cloud becomes enveloped by a layer of hot gas with $T \gtrsim 10^6$ K that is strongest at the head, indicative of crushing by the wind. The cloud itself maintains a nearly isothermal temperature profile from head to tail. The intermediate temperatures are initially an order of magnitude higher than the cloud, but heats up as the cloud propagates outward before cooling at the ends of the cloud tail. We attribute the initial increase in temperatures at the boundary to be due to heating from the wind-shock. The boundary prevents the shock from destroying the cloud.

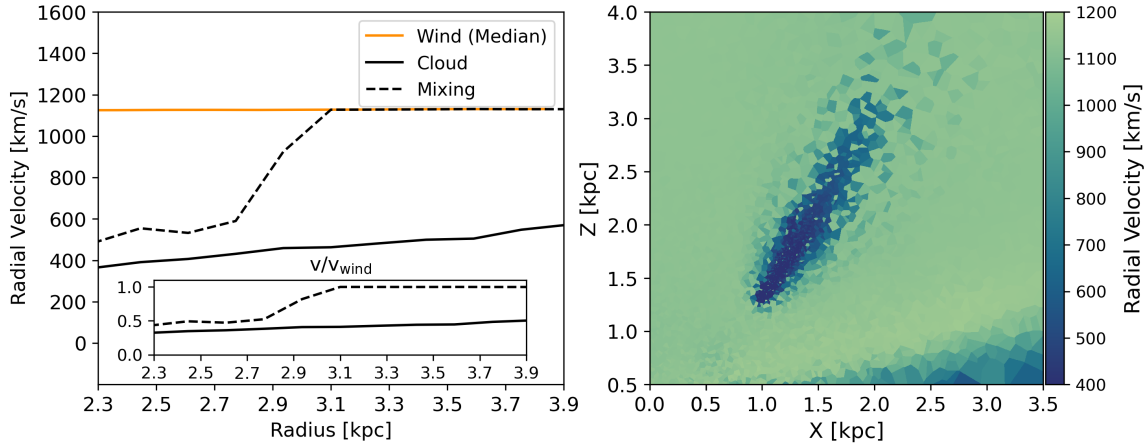


Figure 4.24. Velocity slice of the entrained cloud (**right**), along with the radial velocity profiles (**left**) of the cloud (solid black) and mixing layer (dashed). The wind velocity (solid orange) is included for comparison. The inset plot is the ratios of both the cloud and mixing velocities with that of the wind velocity across radii. The higher velocities of the tail indicate that the cloud starts to become co-moving at the tail first, and then the head. The mixed layer is only ~ 100 km/s higher than the cloud at the head, but increases and becomes completely co-moving with the wind at $r \geq 3.1$ kpc. This suggests an initial deceleration, where momentum is transferred from the wind to the cloud via the boundary layer. This transfer of momentum accumulates at the tail, causing the intermediate velocities to converge with the wind. Past $r = 3.1$ kpc, the wind mixes and transfers mass to the cloud.

and minimum overdensity $\delta = (n_{\text{cell}} - \langle n_{\text{wind}} \rangle) / \langle n_{\text{wind}} \rangle$ of 5. Mixed cells are considered by setting a threshold temperature range where $10^{4.5} \text{ K} < T_{\text{cell}} \leq 10^{5.5} \text{ K}$. Note that because the dense cloud has a much higher resolution than the significantly less dense mixing layer, it is unfortunately somewhat difficult to fully resolve the structural properties of the intermediate mixed gas. We find that the cloud temperature profile is nearly isothermal, starting with a cloud head of temperature $T < 10^4 \text{ K}$, which heats up slightly as the tail starts to expand, before cooling down to near the temperature floor $T_{\text{floor}} = 10^{3.5} \text{ K}$ as the tail gas mixes with the wind. The temperature of the mixed gas undergoes more noticeable changes, being roughly 1 order of magnitude higher than the cloud temperature at the head. However, as cloud gas is sheared outward by the wind, the boundary layer heats up, reaching temperatures that exceed 10^5 K . Once the cloud starts to fade and mix into the background wind, the mixing temperatures cool down to $T \sim 10^5 \text{ K}$. We attribute the initial increase in the boundary temperatures to the influence of the wind-driven shock, which heats up the mixing layer. The boundary prevents the shock from destroying the cloud, which experiences a very minor increase in temperature. As the shock subsides, the mixed layer cools again.

In Fig. 4.24, we show the central edge-on slice of the cloud velocities, along with the median velocity profile of both the cloud and the mixing layer. For reference, we also include the background wind profile. Noticeably, the cloud becomes more entrained with distance, with head velocities that are roughly ~ 350 km/s, corresponding to $\sim 30\%$ of the wind velocity. At the tail, the cloud is about ~ 550 km/s, corresponding to $\sim 50 - 60\%$ of the wind velocities. This indicates that the cloud is accelerated to co-moving velocities at tail first, and then the head. For the mixing layer, we see that at the cloud head, it is only ~ 100 km/s higher than the cloud velocities, and becomes significantly faster to the extent that it co-moving with the rest of the wind at $r = 3.1$ kpc. The velocities of the

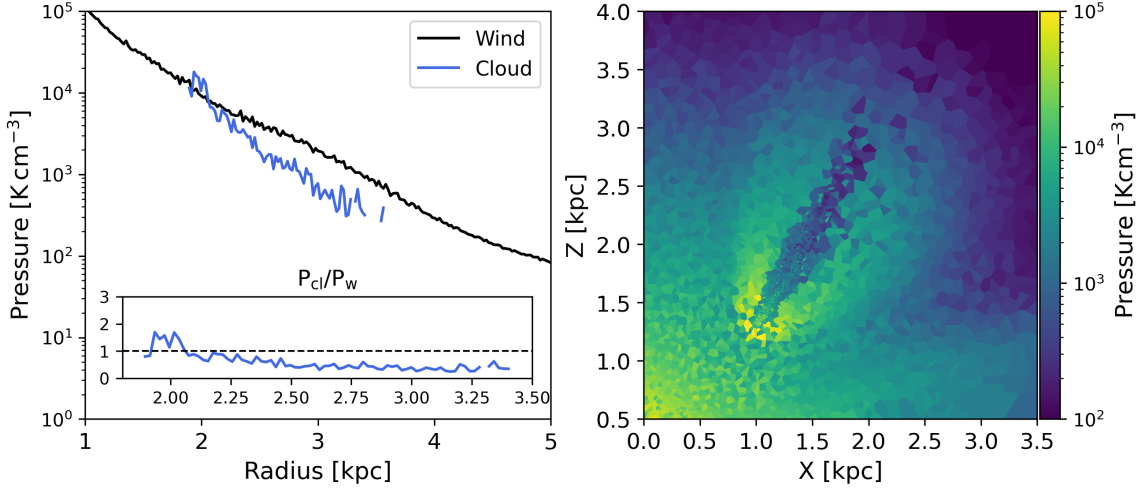


Figure 4.25. Pressure slice of the cold cloud (**right**), along with the median profiles (**left**) overlaid on top of those of the wind. The pressures of the cloud are in rough equilibrium with the wind, indicating that the cloud expands differentially with distance, which reduces the density contrast between the cloud and the wind and causes it to fade into the wind at large distances. The tail is under-pressurized, which is likely caused by the tail crossing cooling radius R_{cool} , where the cooling flow can siphon cold gas into the cloud and allowing it to survive at large distances.

mixing layer suggests an initial deceleration effect by the wind, where momentum is transferred from the hot wind to the momentum-driven cold cloud via the mixing layer, which entrains and accelerates the cloud (Schneider et al. 2020; Thompson & Heckman 2024). This momentum transfer process starts at the head and accumulates at the tail, causing the tail to become more entrained than the head. After the wind becomes co-moving, we see that the cloud becomes diffusive, indicating mixing and transfer of mass with the wind (Dutta et al. 2025; Veilleux et al. 2020).

Comparing the results of our case study to those of cloud crushing simulations e.g. Gronke & Oh (2018); Fielding et al. (2020), it is clear that the cloud corroborates the established head-tail morphology and isothermal cloud profile. We use Equation 2.21 to estimate the critical column density, assuming a $T_{\text{mix}} = 10^{5.5}$ K and an interpolated median cooling function of $1.03 \cdot 10^{-21}$ erg cm 3 s $^{-1}$ at T_{mix} , and acquire a value of $N_{\text{crit,cl}} = 1.5 \cdot 10^{19}$ cm $^{-2}$. This value is significantly lower than even the least dense parts of the cold cloud, indicating we should expect to see cold mass growth in the cloud at large distances. However, as seen in Fig. 4.22, the cloud column density declines and fades as it is entrained, rather than act as a "condensation seed" that accretes mass (Veilleux et al. 2020). Furthermore, while efficient cooling does suggest a local inflow that allows clouds to take up surrounding wind gas (best shown in the mass outflow rates of the $\alpha = 0.9, \beta = 1.0$ wind in Fig. 4.21), the cloud instead expands as it is entrained by the wind (see Fig. 4.18). Schneider et al. (2020) posit that this discrepancy in cloud behavior could potentially be due to differences in wind physics. In cloud crushing simulations, it is typical to use laminar plane-parallel winds, which allows for unimpeded cloud mass growth. CC85 winds, by contrast, are radially expanding, and include transverse velocity components that could disrupt and prevent the growth of cold clouds. Recent work by Dutta et al. (2025) have argued that clouds entrained by CC85 winds undergo a differential expansion orthogonal to the wind direction, becoming isobaric relative to the wind. The wind and cloud maintain a local pressure equilibrium, causing the cloud to lose its density contrast and fade into the background wind.

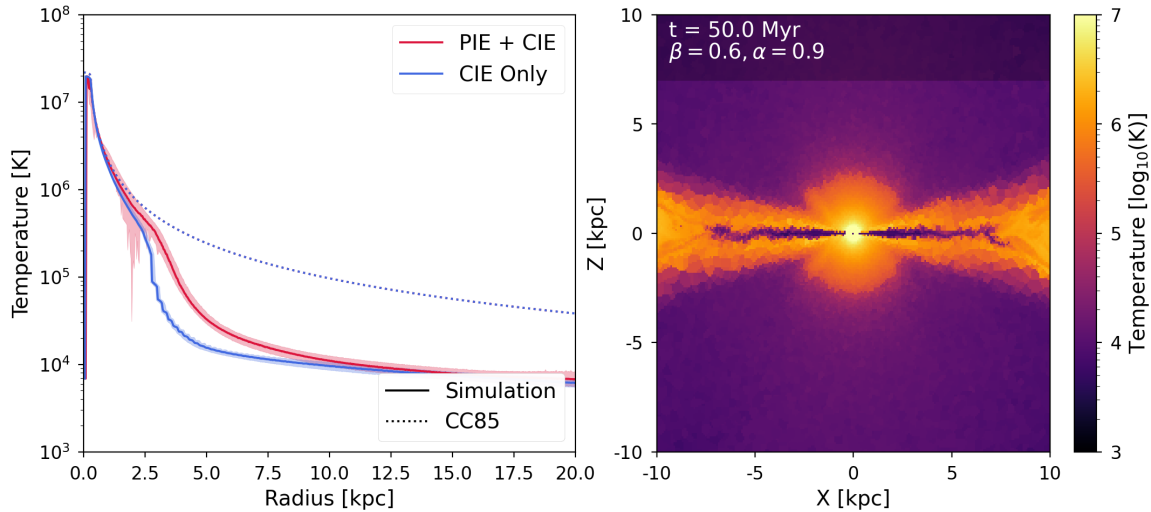


Figure 4.26. Temperature slice (right) of the CIE-cooled wind and median temperature profiles (left) comparing the CIE and PIE routines. The CIE cooling routine produces a steep drop in temperature compare to the PIE routine. This creates a sharply defined cooling flow. However, clouds are not ejected from the disk.

To verify this, we show the edge-on pressure slice of the cloud, along with the median pressure profile overlaid on top of the median wind profile in Fig. 4.25. We find that aside from initial high pressure due to wind crushing, the pressures of the high density cloud head maintain a rough equilibrium with the background wind. At the less dense tail, we instead find that the gas is noticeably under-pressurized compared to the wind, which is likely caused by the tail crossing the cooling radius R_{cool} and being enveloped by the cooling flow. At this distance, it is possible that the a negative pressure gradient can siphon gas into the cloud (Dutta et al. 2022; Gronke & Oh 2020), allowing for the cloud to sustain itself at large distances and explaining why we see cold gas clouds even further away from the starburst. Under very efficient cooling, the siphoning of cold gas into the cloud could allow it to expand enough to create the cloud arcs seen in Fig. 4.18.

4.3.4 Cooling Models

Thus far in Section 4.3, we've applied a cooling routine based on the assumption that gasses are in photoionization equilibrium (PIE) with an extragalactic UV background. However, as previously established in Section 2.3, PIE cooling can suppress the cooling rates of low density gas, and even heat gas at low enough temperatures (Wiersma et al. 2009). In this subsection, we investigate how different cooling routines can affect the structure and evolution of a radiatively cooled wind by comparing our fiducial wind, which uses a PIE cooling routine, versus a cooled wind that uses a collisional equilibrium (CIE) cooling model that neglects the UV background altogether.

We start by comparing their temperature profiles, Fig. 4.26, along with examining the edge-on central slice of the temperature of the CIE simulation. Whereas the fiducial wind simulation has a smooth temperature profile that gradually falls to 10^4 K by $r = 10$ kpc, we find that the increased cooling causes the CIE-controlled wind to develop a smaller, well-defined cooling radius that is marked by a sharp decline in temperature, leading to in-situ formation of a cooling flow at shorter distances. However, unlike the PIE wind, we do not find evidence that CIE wind successfully entrains cold clouds from the disk.

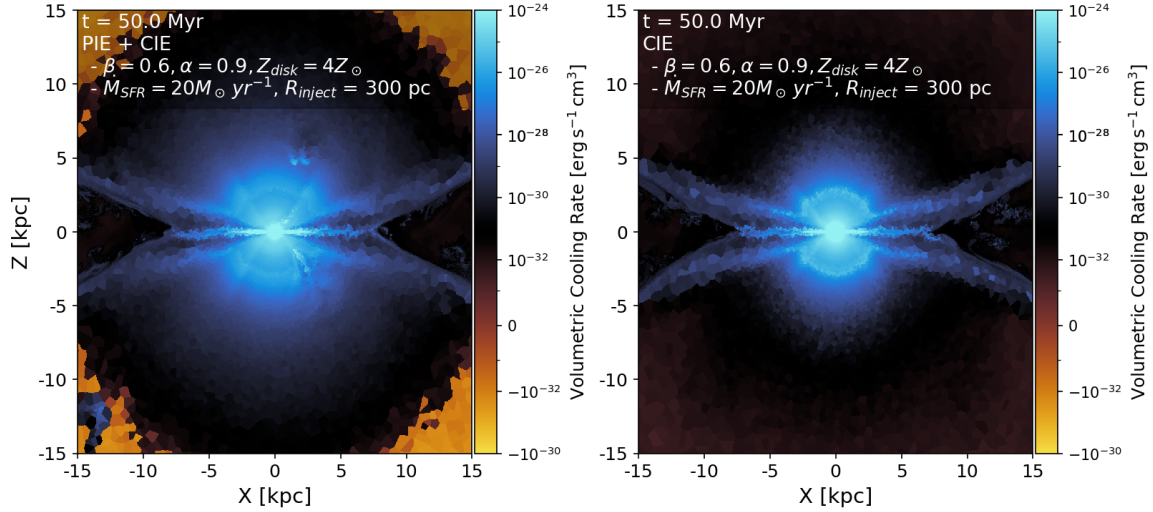


Figure 4.27. Edge-on slice comparing the volumetric cooling rates for wind simulations running a PIE (left) and CIE (right) cooling routines. The PIE model is based on both temperature and density, creating a region of high density pre-cooling radius, followed by a gradual decline in cooling, and heating at large distances. Highly dense clouds heads have high cooling radius, while tails converge with the wind medium. The CIE model is solely based on temperature, creating a region of high cooling pre-cooling radius and no cooling or heating after that point.

To get a better sense as to why this is the case, we plot the volumetric cooling rates of both simulations in Fig. 4.27. Both the CIE and PIE controlled outflows can be separated by ring-like phases. At the center of the outflow inside R_{cool} , we see that the cooling rates are high, corresponding to a high temperature, relatively dense region. The two routines differ significantly past R_{cool} . In both cases, we find that at $r \sim R_{\text{cool}}$, a boundary ring with high cooling rates envelops the spherical zone. This ring corresponds to regions where the temperature undergoes a rapid decline in Fig. 4.26. For the case of CIE, this boundary ring is thin and is characterized by a sharp spike in cooling rate at $r \sim R_{\text{cool}}$, while for $r > R_{\text{cool}}$, the radiative cooling rate quickly falls to nearly 0. The decline in cooling rate past R_{cool} is corroborated by the results of Thompson et al. (2016), who note that gas in CIE becomes adiabatic post-cooling. For PIE, the boundary ring is wider, and the cooling rates in $r > R_{\text{cool}}$ experience a slower and more gradual decline. At large distances, we see that the low densities and temperatures has caused the wind to be radiative heated instead of cooled. The clouds in the PIE-controlled wind have particularly high cooling rates at the dense head, while the cooling in the tail region appears to converge with those of the wind medium.

Given what is shown in Fig. 4.27, we can infer that for the CIE controlled winds, the lack of density dependence means that any potentially entrained cold clouds are cooled at the same rate as cold less dense gas, that is to say, very little. As such, these clouds will likely be sheared and mixed into the hot flow on cloud-crushing timescale t_{cc} before they can be entrained enough to be noticeable.

4.3.5 The Evolution of Shocks and Episodic Bursts

Up until this point, this thesis predominantly focused on the study of continuous starbursts. However, though they are more commonly associated with AGN-driven winds (Veilleux et al. 2020), observational studies of galactic winds e.g. Strickland & Heckman (2009); McQuinn et al. (2009)

Name (abbreviation)	Duty Cycle	Configuration
Fid./Continuous	1	$t_{\text{burst}} = 50 \text{ Myr}$, $t_{\text{rest}} = 0 \text{ Myr}$
Long Bursts (LB)	1/3	$t_{\text{burst}} = 5 \text{ Myr}$, $t_{\text{rest}} = 10 \text{ Myr}$
Short Bursts (SB)	1/6	$t_{\text{burst}} = 1 \text{ Myr}$, $t_{\text{rest}} = 5 \text{ Myr}$
Short Fast Bursts (SFB)	1/2	$t_{\text{burst}} = 1 \text{ Myr}$, $t_{\text{rest}} = 1 \text{ Myr}$

Table 4.4. Table listing the time variability configurations that are compared in Subsection 4.3.5. The left column lists the name of for each simulation, along with the abbreviation we use to refer to them. The middle column is the calculated duty cycle for each configuration. The right column lists the burst and rest periods comprising each configuration.

indicate that nuclear starbursts are not well represented as a single starburst event, but rather as episodic bursts contained within a longer starburst. Thus, in this section, we shift our focus to exploring how the time variability might affect the evolution of galactic winds. For this purpose, we compare wind simulations where rest periods t_{rest} are interspaced between burst periods t_{burst} . These values can be used to calculate the duty cycle $D = t_{\text{burst}}/(t_{\text{burst}} + t_{\text{rest}})$. We first look at the wind's temperature evolution over time, focusing on how the wind evolves over the course of repeated bursts as well as the development of the forward shock. We then follow up by looking at their radial evolution of the periodic winds. Finally, we study how cold gas distributions are affected by periodic bursts. The configurations used for this comparison, along with abbreviated names and duty cycles, can be found in Table 4.4.

We show the temporal evolution of the temperature for all four configurations in Fig. 4.28 (see [link](#)). We find that for all cases, the injected mass and energy drives a biconical, wind-blown "superbubble" which is enveloped by an outer forward shock of CGM gas of temperature $T \sim 10^6\text{--}10^7 \text{ K}$, and a reverse wind shock formed through interactions between the wind and the forward shock. After the initial starburst, the wind cools, decreasing temperatures to $T \lesssim 10^4 \text{ K}$. Subsequent burst episodes repeat the shock heating process, wherein the injection of mass and injection at the start of t_{burst} creates a new wind-blown bubble with its own blast wave. The new blast wave sweeps up the pre-existing wind as it flows outward. It also conductively heats the surrounding wind gas, raising the wind temperatures to $T \sim 10^4\text{--}10^5 \text{ K}$. Upon reaching the shock front at the edges of the bicone, the blast wave coalesces into the shock front. Over the course of several bursts, the shock front of the superbubble forms two biphasic structures. The outer biphasic consists of the shocked CGM and wind from the initial starburst, while the inner biphasic consists of the forward shock of compressed wind from previous starbursts as well as a reverse wind shock from the current starburst.

We find that the duty cycle D plays a modulating role in controlling the evolution of the superbubble's shock front. Starbursts with smaller duty cycles develop thickened, more well-defined shock bubbles, with the SB wind ($t_{\text{burst}} = 1 \text{ Myr}$, $t_{\text{rest}} = 5 \text{ Myr}$, $D = 1/6$) taking up nearly half of the bicone by $t = 50 \text{ Myr}$. As duty cycles become larger, we find that the blast waves start to decrease in size, with the SFB wind ($t_{\text{burst}} = 1 \text{ Myr}$, $t_{\text{rest}} = 1 \text{ Myr}$, $D = 1/2$) forming thin blast waves that create a ripple like pattern within the wind as they propagate outward. As they hit the bicone edge, the blast waves form biphases that are less well-defined in comparison to those with smaller duty cycles, with the shock front of the SFB wind being nearly identical to the continuous case. We argue that the more intense shock patterns are related to the amount of gas injected into the starburst region, and to the wind-blown nature of the superbubble. Because the superbubble is sustained by the injection of energy and momentum by the wind, starbursts with smaller duty cycles creates

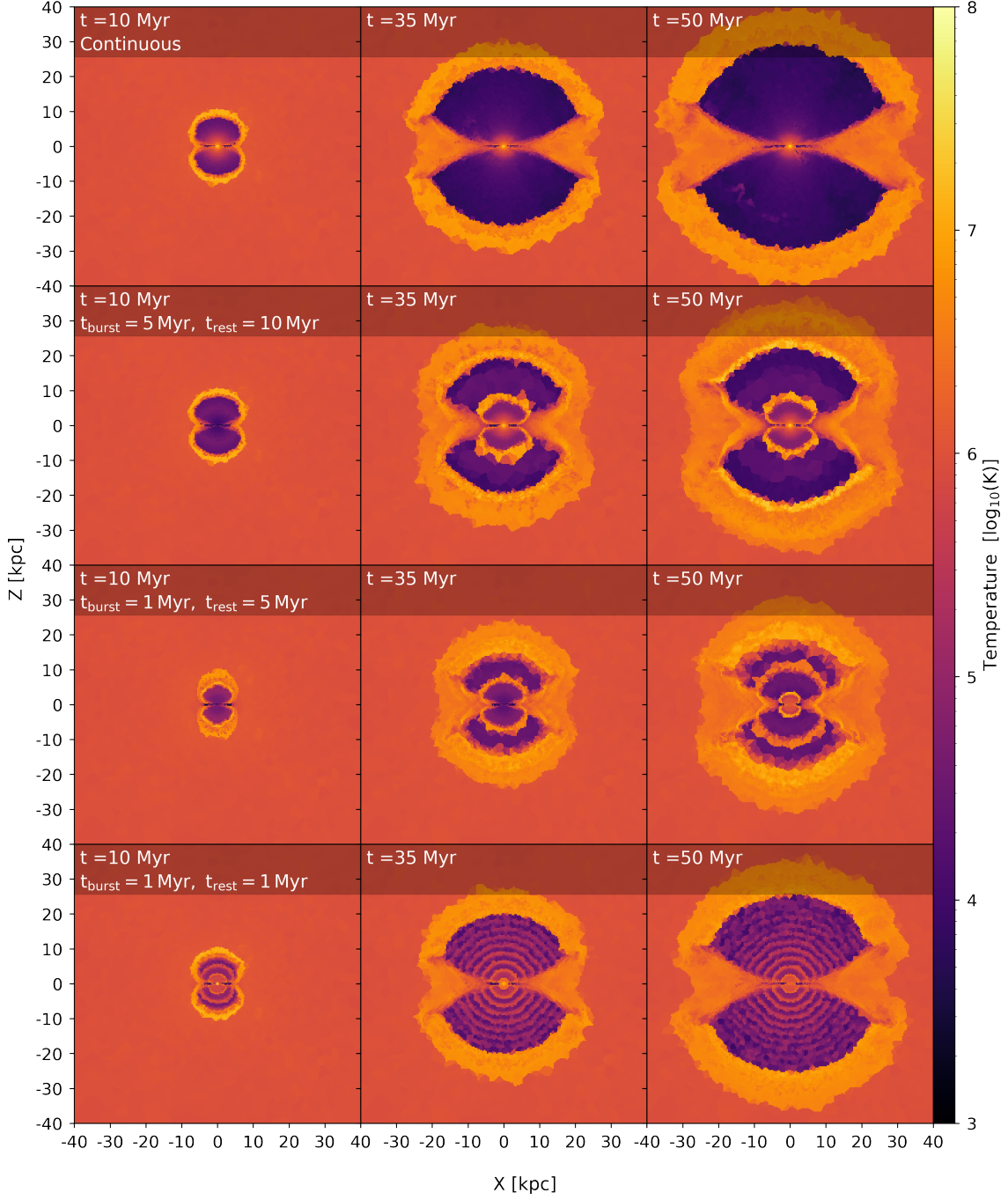


Figure 4.28. Temporal evolution of temperature for continuous (top), LB (upper middle), SB (lower middle), and SFB (bottom) burst configurations. Subsequent bursts repeat the shock process of the initial bursts, forming blast waves which sweep up ambient wind and eventually merging with the existing superbubble shock front. Successive starbursts form bi-phasic shock patterns of shocked CGM and wind from the initial burst and shocked winds from subsequent bursts. Due to less injecting momentum and energy, winds with smaller duty cycles have slower shock fronts and smaller bicones. Because they also inject less mass, subsequent bursts from these winds experience less resistance, leading to larger, hotter wind shocks. Conversely, starbursts with larger duty cycles will have more energy, momentum, and mass injected, leading to larger bicones and less intense shocks.

superbubbles that have smaller bicones and slower shock fronts due to injecting less energy and momentum. Simultaneously, these same starbursts also inject less mass into the wind. Thus, the shocks of subsequent bursts experience less mass resistance as they propagate outwards. Once these shocks hit the current shock front, they form sharper discontinuities and more intense reverse shocks. Conversely, larger duty cycles injection more energy, momentum, and mass, which results in less intense shocks.

In Fig. 4.29, we show the median radial profiles of velocity, density, and temperature for each episodic starburst configuration, averaged over a period of $t = 30\text{--}50$ Myr. Each starburst accelerates the wind to velocities that converge onto the steady state velocities of the fiducial wind, so long as mass and energy injection is maintained. During rest periods, the velocities drop to zero starting from $r = R_{\text{inject}}$ outward. Notably, the SB wind has higher median velocities than the LB wind ($t_{\text{burst}} = 5$ Myr, $t_{\text{rest}} = 10$ Myr, $D = 1/3$) despite having a smaller duty cycle and bicone bubble, while the SFB wind converges with the wind velocities at large distances. Thus, we infer that over longer periods of time, wind with shorter rest periods are faster than winds with longer ones.

However, we find comparatively little differences between density profiles outside of starbursts with larger duty cycles injecting more mass and thus creating higher density winds. Of particular note is that the shocks do not appear to be significantly denser than the wind. We attribute this to be because of previous starbursts sweeping up pre-existing gas, leaving behind a low density background after the injection ceases. Subsequent wind shocks will only sweep up this low density background, and as such will not be much denser than the wind.

When looking at the temperature profiles, we find that a longer burst period corresponds to hotter and more extended individual blast waves. As they propagate outward, these blast waves expand and cool. To compare the shock temperatures to analytic results, we additionally include the CC85 temperature as a dashed blue line in the temperature panel. We note that the SFB wind, which predominantly consists of blast waves, is quasi-adiabatic and corresponds closely to the analytic result, suggesting that radiative cooling is inefficient for blast waves compared to adiabatic expansion. We posit that due to their low densities, the cooling of gas during the rest periods is also predominantly driven by adiabatic expansion. Based on the temporal evolution of the LB wind in Fig. 4.28, along with the temperature evolution in Fig. 4.12 (see subsection 4.3.1), we argue that for a wind to cool radiatively under these parameters, bursts need to be sustained for $t_{\text{burst}} \gtrsim 5$ Myr.

In Fig. 4.30, we examine the fraction of cold gas with $T < 10^{4.5}$ K in the 120° wind bicone over time as well as the median cold gas fraction over radius, time-averaged over 50 Myr. We find that the initial peaks and subsequent decline in cold gas mass fractions over time are due to the acceleration and shredding of cold gas clouds from the first starburst. Following this initial starburst, the cold gas fraction over time depends primarily on their respective t_{rest} and on t_{burst} . In particular, we find that the cold gas mass fraction for the LB wind fluctuates over time, rising to fractions $\gtrsim 0.1$ during the rest periods and declining during the burst periods. We find that this fluctuation is reduced with each subsequent burst, eventually converging onto a fraction that is slightly less than 0.1. We believe that this is due to the wind gas being able to cool for increasingly long periods as the bicone superbubble moves further away from the central starburst, with the slight decline being largely driven by the outer shock layer taking up mass as it flows outward. For the case of the quasi-adiabatic SFB wind, we find that it follows the continuous case, with the cold gas mass fraction increasing over time. However, because cooling is largely adiabatic, we find considerably less cold gas over time compared to the continuous case. The cold gas fraction of the SB remains stable over time, which we attribute to be due to the short t_{burst} . When we examine the cold gas mass fractions across radius,

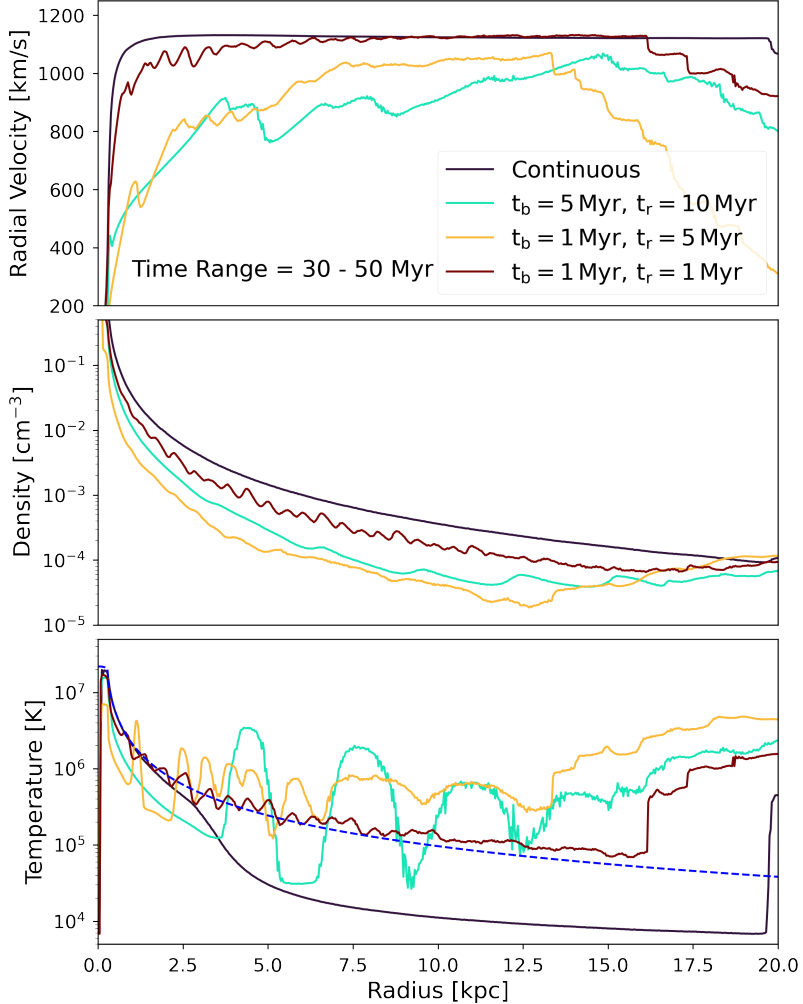


Figure 4.29. Radial profiles of velocity (**left**), density (**middle**), temperature (**right**) of each episodic starburst configuration, averaged across a time period of $t = 30 - 50 \text{ Myr}$. For the temperature, we include the CC85 solution for temperature as a dotted blue line. Velocities go to zero when injection routines cease, causing winds with longer rest times t_{rest} to have correspondingly lower median velocities. Shock densities are not meaningfully distinct from the wind densities due to sweeping up low density background gas. Shock expand and cool as they propagate outwards, with the SFB ($t_{\text{burst}} = 1 \text{ Myr}, t_{\text{rest}} = 1 \text{ Myr}$) wind corresponding closely with the CC85 solution, suggesting that blast waves cool via adiabatic expansion rather than radiative cooling.

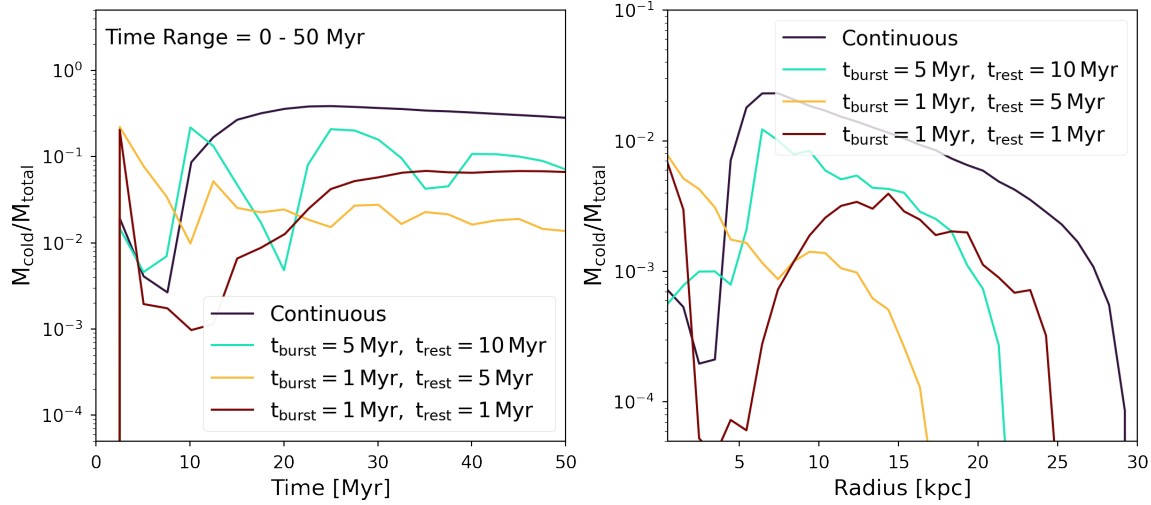


Figure 4.30. Mass fraction of cold gas with $T \leq 10^{4.5}$ K in wind bicone over time (**left**) and median cold gas fraction profile averaged over 50 Myr (**right**). The initial peaks in cold gas fraction over time are due to acceleration and shredding of clouds. Temporal evolution after that is dependent on their respective t_{burst} and t_{rest} , with increasing cold gas fraction during t_{rest} and declining during t_{burst} . The cold gas fraction stabilizes over time as gas flows outward, allowing gas to cool over longer periods. Cold gas fractions peak and subsequently decline over large radii due to gas taking longer to reach those points. How far gas is distributed is largely based on their duty cycles, with larger duty cycles corresponding to faster velocities and an extended cold gas distribution. Initial peaks in $t_{\text{burst}} = 1 \text{ Myr}$ winds are due to their relatively short burst times, which is followed by rapid cooling during the rest period.

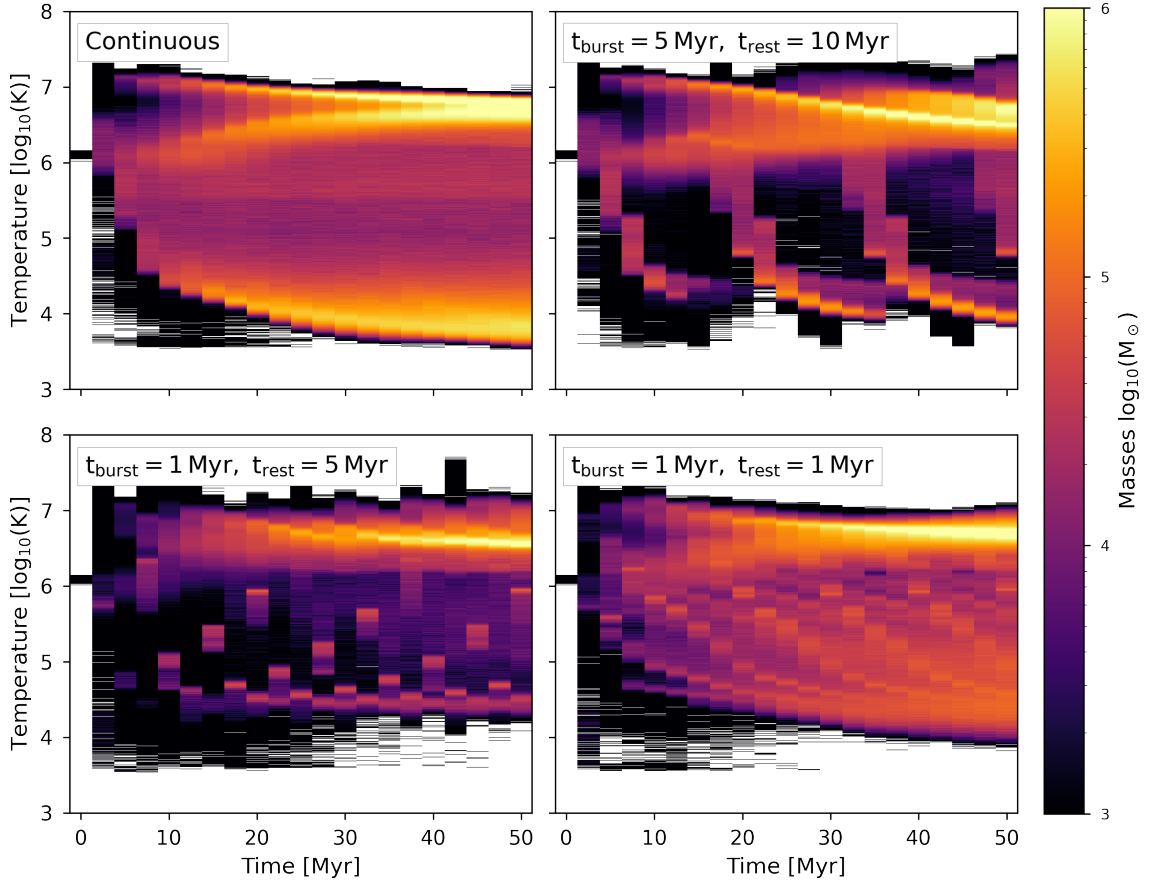


Figure 4.31. Temperature of cold wind within the wind bicone across 50 Myr for varying burst models. For all cases, the wind develops a hot high mass phase that corresponds to the forward shock. Winds with sufficient mass and energy injection form a secondary fork-like phase that corresponds to the wind shocks. Over time, the forward and wind shocks merge together to form a single phase, indicating that discontinuities between the two shocks disappear across large distances. The cold gas comprise a single high mass phase for the continuous starburst and several strand-like phases for the episodic bursts. We find that these phases get longer as time goes on, indicating that cool gas survives for longer periods of time as the bicone flows outward.

we find that they are largely dependent on their duty cycles, with larger duty cycles corresponding to larger velocities and therefore a more extended distribution of cold gas, with declining fractions across distances being the result of gas taking longer to reach those points. Furthermore, due to their short burst times, which are immediately followed by rapid cooling during their rest period, we find that starbursts with $t_{\text{burst}} = 1 \text{ Myr}$ have higher mass fractions at $r \lesssim 2.5 \text{ kpc}$.

In Fig. 4.31, we show the phase diagram of temperature over time, weighted by the mass, for each burst configuration. We find that for all cases, the wind develops a well-defined phase of shocked gas, which over time accumulates mass and forms the most massive phase within the bicone superbubble. We find that the shocks of the continuous, LB, and SFB cases develop a secondary fork-like phase, which corresponds to the reverse wind shocks. Notably, we find that winds with longer t_{burst} have more well-defined wind forks. We attribute this to be due to winds with longer burst times contributing more mass to the shocked layer, thus causing a stronger discontinuity. Over time, the two prongs merge together to form a single phase of hot gas, indicating that discontinuities

between the forward and reverse shocks disappear across large distances. This could either indicate mixing via hydrodynamic instabilities, or gradual cooling of the forward shock due to expansion. We note that for the continuous starburst, a second high mass phase consisting of cool gas develops at $t \approx 7$ Myr, with an intermediate phase consisting of the hot wind for $r \leq R_{\text{cool}}$. For phases with episodic bursts, we find that the formation of cool gas is represented with strand-like structures that correspond to rest periods between bursts. Notably, these strands become longer with time, indicating that as the bicone expands, cool gas can remain for significantly longer periods before they are replaced by wind from later starbursts.

5 Conclusions and Outlook

In this thesis, we set out to build a suite of idealized hydrodynamic simulations of galactic winds using a moving mesh approach, with the goal of understanding the physical structure and evolutionary processes behind galactic winds as well as ascertaining the effects of radiative cooling on wind flow. We start by giving a summary of key results in Section 5.1. Afterwards, we transition to discussing the limitations of the suite and proposing opportunities for follow-up work in Section 5.2.

5.1 Summary of Key Results

We summarize our key results as follows:

The injection of mass and energy into a central starburst drives a galactic wind whose properties can be described using the CC85 model. When a galactic disk is included, the wind forms a wind-blown superbubble with a curved biconical morphology that forms along the z-axis due to resistance with the disk. The wind comprises a collimated layer of free wind, which is surrounded by a turbulent shear layer that forms due to disk-wind interactions.

Radiative cooling suppresses disk-wind interactions, creating a less turbulent bicone. Under efficient cooling, cool gas can originate either as entrained cool clouds or cold gas that formed in-situ beyond R_{cool} . As we see a single coherent phase of cool gas, rather than the predicted transmigration under in-situ cooling, we infer that entrained cold clouds is more likely the primary origin of cooler phases under ideal circumstances. However, we posit that it is possible for cold structures to form in-situ if the wind contained addition material such as dust or if gravitational interactions can sufficiently perturb the wind. We find that winds start out as being energy-driven before becoming momentum-driven once the wind enters the cooling flow. From this, we concluded that cool phases in multiphase gas are momentum-driven.

Wind shearing causes entrained cold clouds to ablate and elongate, creating a head-to-tail morphology, as well as a warm mixed layer. The mixing layer protects the cloud from being shredded by the wind and entrains the cloud via momentum transfer. The transfer of momentum starts at the head and accumulates at the cloud, causing the tail to become entrained first. While the cloud properties corroborates much of the established literature, we found that our results differed in that the cloud expanded differentially and faded as it became entrained instead of increasing in size. We argue this is because our galactic wind is radially expanding, whereas cloud crushing studies often assume a plane-parallel wind. For a radially expanding wind, the cloud instead remains roughly isobaric with the wind, causing it to expand and fade as it is entrained. The cooling flow beyond R_{cool} can siphon gas into the cloud, extending its lifetime and allowing it to survive substantial distances into the CGM. Under extremely efficient cooling, the differential expansion leads to the clouds forming arcs that take over much of the wind flow.

5.2 Outlook

Overall, we found that the moving Voronoi mesh approach of AREPO was highly effective, allowing us to study the evolution of cold clouds far into the CGM while remaining at high fidelity. This feat would not be possible with Eulerian grid codes except at very high resolutions. Thus, we believe that our results provide a strong framework for building a theoretical picture for stellar feedback-driven multiphase galactic winds.

Nevertheless, we note that this suite has clear limitations. We found that the wind became increasingly low resolution as they decreased in density and flowed away from the starburst. While this is expected to a degree, the coarse resolutions made it difficult to resolve the warm intermediate regions of cool clouds due to the density contrast between the cold and hot phases. Improving the resolution can be easily achieved by lowering the volume criterion for refinement, which increases the number of cells being ejected outward. However, doing so significantly increased the computing cost, often exceeding our available computational constraints.

A more prominent limitation is our relatively simple model for metallic cooling, particularly our treatment of the metallicity. For this suite, we implemented the metallicity as a passive scalar quantity. However, the metallicity is obviously a key parameter in determining the cooling efficiency. We posit that our implementation of metallicity as a passive scalar was a major reason as to why it took super-solar metallicities to get sustained cool cloud formation. Additionally, we found that there was little mixing of metals inside the wind, but rather the entire bicone develops a singular phase of near uniform metallicity. Thus, we believe that the first step in terms of improving our radiative cooling model would be to implement the metallicity as an active scalar field. Such an adjustment could be combined with self-gravity, which could potentially drive in-situ formation of cold gases beyond the cooling radius. Such improvements, however, would require more extensive changes to AREPO’s implementation of hydrodynamics.

Aside from the above, we also propose the following avenues for future work. The first would be to change the central starburst model to a clustered feedback model of individual clusters from which winds can be driven outwards. Our central starburst model is a clear oversimplification that may not accurately produce the wind structures seen in observations, as it is well-established that stars form in dense star cluster environments (Veilleux et al. 2020). A clustered feedback model introduces inherent perturbations within the wind, which could lead to more complex and varied cold structures than the ones produced by our suite. Notably, Schneider et al. (2018) found that a clustered feedback model was able to produce multiphase gas even at lower mass-loading. The second, more long-term avenue would be to consider stellar-feedback mechanisms beyond supernovae. While much of our current understanding implicates thermal heating via supernovae explosions as the key driver of winds, cosmic rays and radiation pressure are expected to be major drivers in their own right. Radiation pressure feedback may be essential to understanding the nature of winds found in extremely dense, dusty galaxies such as ULIRGs. Cosmic rays, while possessing only a small fraction of the SN energy budget, also possess long lifetimes which allows them to launch weak but sustained outflows to considerable distances (Thomas et al. 2025; Kjellgren et al. 2025). Thus, we argue that both radiation pressure and cosmic rays need to be explored alongside supernovae-driven feedback to acquire a complete picture of galactic winds.

Bibliography

- Begelman, M. C. & Fabian, A. C. 1990, "Turbulent mixing layers in the interstellar and intracluster medium.", *MNRAS*, 244, 26P
- Bekki, K. & Stanimirović, S. 2009, "The total mass and dark halo properties of the Small Magellanic Cloud", *MNRAS*, 395, 342
- Chevalier, R. A. & Clegg, A. W. 1985, "Wind from a starburst galaxy nucleus", *Nature*, 317, 44
- Dutta, A., Sharma, P., & Gronke, M. 2025, "Fading in the Flow: Suppression of cold gas growth in expanding galactic outflows", *MNRAS* [arXiv:2506.08545]
- Dutta, A., Sharma, P., & Nelson, D. 2022, "Cooling flows around cold clouds in the circumgalactic medium: steady-state models and comparison with TNG50", *MNRAS*, 510, 3561
- Fabbiano, G. & Trinchieri, G. 1984, "The complex X-emission of NGC 253.", *ApJ*, 286, 491
- Fielding, D., Quataert, E., McCourt, M., & Thompson, T. A. 2017, "The impact of star formation feedback on the circumgalactic medium", *MNRAS*, 466, 3810
- Fielding, D. B., Ostriker, E. C., Bryan, G. L., & Jermyn, A. S. 2020, "Multiphase Gas and the Fractal Nature of Radiative Turbulent Mixing Layers", *ApJ*, 894, L24
- Fisher, D. B., Bolatto, A. D., Chisholm, J., et al. 2025, "JWST observations of starbursts: cold clouds and plumes launching in the M 82 outflow", *MNRAS*, 538, 3068
- Fluetsch, A., Maiolino, R., Carniani, S., et al. 2019, "Cold molecular outflows in the local Universe and their feedback effect on galaxies", *MNRAS*, 483, 4586
- Gronke, M. & Oh, S. P. 2018, "The growth and entrainment of cold gas in a hot wind", *MNRAS*, 480, L111
- Gronke, M. & Oh, S. P. 2020, "How cold gas continuously entrains mass and momentum from a hot wind", *MNRAS*, 492, 1970
- Hopkins, P. F., Kereš, D., Oñorbe, J., et al. 2014, "Galaxies on FIRE (Feedback In Realistic Environments): stellar feedback explains cosmologically inefficient star formation", *MNRAS*, 445, 581
- Hopkins, P. F., Quataert, E., & Murray, N. 2012, "Stellar feedback in galaxies and the origin of galaxy-scale winds", *MNRAS*, 421, 3522
- Hopkins, P. F., Wetzel, A., Kereš, D., et al. 2018, "FIRE-2 simulations: physics versus numerics in galaxy formation", *MNRAS*, 480, 800

- Katz, N., Weinberg, D. H., & Hernquist, L. 1996, "Cosmological Simulations with TreeSPH", *ApJS*, 105, 19
- Kjellgren, K., Girichidis, P., Gölle, J., et al. 2025, "The dynamical impact of cosmic rays in the Rhea magnetohydrodynamic simulations", *A&A*, 700, A124
- Licquia, T. C. & Newman, J. A. 2015, "Improved Estimates of the Milky Way's Stellar Mass and Star Formation Rate from Hierarchical Bayesian Meta-Analysis", *ApJ*, 806, 96
- Mandal, A., Mukherjee, D., & Mignone, A. 2023, "A Self-gravity Module for the PLUTO Code", *ApJS*, 268, 40
- Martini, P., Leroy, A. K., Mangum, J. G., et al. 2018, "H I Kinematics along the Minor Axis of M82", *ApJ*, 856, 61
- McQuinn, K. B. W., Skillman, E. D., Cannon, J. M., et al. 2009, "The True Durations of Starbursts: Hubble Space Telescope Observations of Three Nearby Dwarf Starburst Galaxies", *ApJ*, 695, 561
- Miyamoto, M. & Nagai, R. 1975, "Three-Dimensional Models for the Distribution of Mass in Galaxies", *PASJ*, 27, 533
- Mo, H., van den Bosch, F. C., & White, S. 2010, Galaxy Formation and Evolution (Cambridge University Press)
- Navarro, J. F., Frenk, C. S., & White, S. D. M. 1997, "A Universal Density Profile from Hierarchical Clustering", *ApJ*, 490, 493
- Nelson, D., Pillepich, A., Springel, V., et al. 2019, "First results from the TNG50 simulation: galactic outflows driven by supernovae and black hole feedback", *MNRAS*, 490, 3234
- Nguyen, D. D., Thompson, T. A., Schneider, E. E., Lopez, S., & Lopez, L. A. 2023, "Dynamics of hot galactic winds launched from spherically-stratified starburst cores", *MNRAS*, 518, L87
- Pillepich, A., Nelson, D., Springel, V., et al. 2019, "First results from the TNG50 simulation: the evolution of stellar and gaseous discs across cosmic time", *MNRAS*, 490, 3196
- Rix, H.-W. & Bovy, J. 2013, "The Milky Way's stellar disk. Mapping and modeling the Galactic disk", *A&A Rev.*, 21, 61
- Rupke, D. S. N., Coil, A., Geach, J. E., et al. 2019, "A 100-kiloparsec wind feeding the circumgalactic medium of a massive compact galaxy", *Nature*, 574, 643
- Rupke, D. S. N., Coil, A. L., Perrotta, S., et al. 2023, "The Ionization and Dynamics of the Makani Galactic Wind", *ApJ*, 947, 33
- Scannapieco, E. & Brüggen, M. 2015, "The Launching of Cold Clouds by Galaxy Outflows. I. Hydrodynamic Interactions with Radiative Cooling", *ApJ*, 805, 158
- Schneider, E. E., Ostriker, E. C., Robertson, B. E., & Thompson, T. A. 2020, "The Physical Nature of Starburst-driven Galactic Outflows", *ApJ*, 895, 43
- Schneider, E. E. & Robertson, B. E. 2017, "Hydrodynamical Coupling of Mass and Momentum in Multiphase Galactic Winds", *ApJ*, 834, 144

- Schneider, E. E. & Robertson, B. E. 2018, "Introducing CGOLS: The Cholla Galactic Outflow Simulation Suite", *ApJ*, 860, 135
- Schneider, E. E., Robertson, B. E., & Thompson, T. A. 2018, "Production of Cool Gas in Thermally Driven Outflows", *ApJ*, 862, 56
- Schneider, P. 2015, Extragalactic Astronomy and Cosmology: An Introduction (Springer-Verlag)
- Springel, V. 2010, "E pur si muove: Galilean-invariant cosmological hydrodynamical simulations on a moving mesh", *MNRAS*, 401, 791
- Strickland, D. K. & Heckman, T. M. 2009, "Supernova Feedback Efficiency and Mass Loading in the Starburst and Galactic Superwind Exemplar M82", *ApJ*, 697, 2030
- Strickland, D. K., Heckman, T. M., Weaver, K. A., & Dahlem, M. 2000a, "Chandra Observations of NGC 253: New Insights into the Nature of Starburst-driven Superwinds", *AJ*, 120, 2965
- Strickland, D. K., Heckman, T. M., Weaver, K. A., & Dahlem, M. 2000b, "Chandra Observations of NGC 253: New Insights into the Nature of Starburst-driven Superwinds", *AJ*, 120, 2965
- Thomas, T., Pfrommer, C., & Pakmor, R. 2025, "Why are thermally and cosmic ray-driven galactic winds fundamentally different?", *A&A*, 698, A104
- Thompson, T. A. & Heckman, T. M. 2024, "Theory and Observation of Winds from Star-Forming Galaxies", *arXiv e-prints*, arXiv:2406.08561
- Thompson, T. A., Quataert, E., Zhang, D., & Weinberg, D. H. 2016, "An origin for multiphase gas in galactic winds and haloes", *MNRAS*, 455, 1830
- Veilleux, S., Cecil, G., & Bland-Hawthorn, J. 2005, "Galactic Winds", *ARA&A*, 43, 769
- Veilleux, S., Maiolino, R., Bolatto, A. D., & Aalto, S. 2020, "Cool outflows in galaxies and their implications", *A&A Rev.*, 28, 2
- Watson, M. G., Stanger, V., & Griffiths, R. E. 1984, "X-ray emission from M82.", *ApJ*, 286, 144
- Weinberger, R., Springel, V., & Pakmor, R. 2020, "The AREPO Public Code Release", *ApJS*, 248, 32
- Wiersma, R. P. C., Schaye, J., & Smith, B. D. 2009, "The effect of photoionization on the cooling rates of enriched, astrophysical plasmas", *MNRAS*, 393, 99
- Xu, X., Heckman, T., Yoshida, M., Henry, A., & Ohyama, Y. 2023, "What Are the Radial Distributions of Density, Outflow Rates, and Cloud Structures in the M82 Wind?", *ApJ*, 956, 142
- Zhang, D. 2018, "A Review of the Theory of Galactic Winds Driven by Stellar Feedback", *Galaxies*, 6, 114
- Zhang, D., Thompson, T. A., Quataert, E., & Murray, N. 2017, "Entrainment in trouble: cool cloud acceleration and destruction in hot supernova-driven galactic winds", *MNRAS*, 468, 4801